

Synthesis and Applications of Copper Nanowires and Nanoplates

by

Mutya Aguila Cruz

Department of Chemistry
Duke University

Date: _____

Approved:

Benjamin Wiley, Advisor

Jie Liu

Aaron Franklin

Kevin Welsher

Dissertation submitted in partial fulfillment of
the requirements for the degree of Doctor
of Philosophy in the Department of
Chemistry in the Graduate School
of Duke University

2019

ABSTRACT

Synthesis and Applications of Copper Nanowires and Nanoplates

by

Mutya Aguila Cruz

Department of Chemistry
Duke University

Date: _____

Approved:

Benjamin Wiley, Advisor

Jie Liu

Aaron Franklin

Kevin Welsher

An abstract of a dissertation submitted in partial
fulfillment of the requirements for the degree
of Doctor of Philosophy in the Department of
Chemistry in the Graduate School of
Duke University

2019

Copyright by
Mutya Aguila Cruz
2019

Abstract

Research on the unique properties of metal nanocrystals sparked the advent of powerful nanomaterial-based technologies that improve the performance of catalysts, electronics, and cancer therapies, to name a few. Due to their promise, extensive progress has been made in tailoring the properties of metal nanocrystals by controlling their size, shape, composition, and structure. However, these nanoscale materials remain largely within the confines of research laboratories. One of the biggest hindrances to the widespread use of metal nanocrystals is cost. Precious metals such as Ag and Au exhibit compelling properties in the nanoscale, yet the astronomical cost of bulk materials and low throughput of synthetic methods make them impractical for applications that require more than a few milligrams of nanocrystals. This work addresses this issue by furthering our knowledge of Cu nanocrystal synthesis and presenting synthetic methods that lower the cost of its production.

Cu is significantly cheaper and more abundant compared to other metals, and much like Au and Ag nanocrystals, Cu nanocrystals exhibit conductive and catalytic properties. In this work, we present efforts to increase the impact of Cu nanowires by first developing a multigram-scale synthesis of stable Ag-coated Cu nanowires (Cu-Ag nanowires). The two-step process starts with the production of 4.4 g of Cu nanowires in 1 h, followed by a Ag-coating procedure that yields 22 g of Ag-coated Cu nanowires (Cu-

Ag nanowires) in 1 h. Due to the large diameters of Cu nanowires produced by this synthesis (≈ 240 nm), a Ag:Cu mol ratio of 0.04 is sufficient to coat the nanowires with a protective, oxidation-resistant shell. This multigram synthesis of Cu and Cu-Ag nanowires enabled the development of the first nanowire-based conductive polymer composite for 3D printing with a resistivity of $0.002 \Omega \text{ cm}$, which is >100 times more conductive than commercially available graphene-based 3D printing filaments. Furthermore, a felt-like material consisting of Cu-Ag nanowires was also used to create a stretchable conductor that has a conductivity of 1000 S/cm and is stretchable up to 300%. Finally, Cu nanowires were annealed to create a porous flow-through electrode (FTE). Compared to other commercially available FTEs, Cu nanowires are significantly thinner, resulting in a 15x increase in surface area compared to carbon paper. This translates to a 4.2x increase in the productivity of an electroorganic intramolecular cyclization reaction.

We also developed a self-heating synthesis of Cu nanowires, which produced shorter, thinner nanowires than was previously possible. Self-heating is accomplished through NaOH dilution and glucose degradation, which allows us to tune the length of the Cu nanowires in the range of 1.0 to $5.5 \mu\text{m}$ by simply changing the concentration of glucose, and thereby the temperature of the reaction. The self-heating aspect of this synthesis decreases the energy cost associated with producing Cu nanowires, simplifies the reaction procedure, as well as increases its scalability.

Finally, we employed single-crystal electrochemistry to elucidate the growth mechanism of Cu nanoplates. Cu nanoplates have also been used in electronic and catalytic applications, yet their growth is not as well-understood as Cu nanowires. Thus, before they can be produced at quantities similar to that of Cu nanowires, we need to understand how they grow. Single-crystal electrochemistry allows us to replicate the crystal structure on the surfaces of Cu nanoplates using single crystal electrodes. The current density (j_{mp}) of Cu(111) and Cu(100) single crystal electrodes were measured in the nanoplate growth solution, which showed that Cu reduction is 2.6x higher on Cu(100) compared to Cu(111) in the presence of iodide ions (I^-) in a solution containing a $CuCl_2$ precursor and hexadecylamine (HDA). Increasing the concentration of I^- results in a higher ratio $j_{mp}^{(100)}/j_{mp}^{(111)}$, which alludes to the passivation of the {111} basal surfaces of Cu nanoplates, resulting in lateral growth. This work clarifies the role of halide ions on the growth of Cu nanoplates, giving us insight into how size-control can be achieved.

As a whole, this work aims to increase the impact of Cu nanocrystal-based innovations by increasing throughput, simplifying reaction procedures, and achieving control over the size and dimensions of the synthesized product.

Dedication

I would like to dedicate this work to my parents, who have made countless sacrifices to get me to where I am today. Thank you for always prioritizing my education and for showing me the value of hard work. I would also like to dedicate this work to my husband, who carried me through challenging moments and cheered for me in times of success.

Contents

Abstract	iv
List of Tables	xi
List of Figures	xii
Acknowledgements	xv
1. Introduction	1
1.1 Colloidal Growth of Anisotropic Metal Nanocrystals	2
1.2 Synthesis of Pentagonally-Twinned Cu Nanowires.....	6
1.3 Current Limitations to the Utilization of Cu Nanowires.....	9
1.4 Cu Nanoplate Growth and Applications	12
1.5 Using Single-Crystal Electrochemistry to Explain the Growth Mechanism of Cu Nanocrystals.....	14
2. Improvements in the Colloidal Synthesis of Cu Nanowires	21
2.1 Multigram-Scale Synthesis of High Aspect Ratio Cu-Ag Nanowires.....	22
2.1.1 Glucose-Based Cu Nanowire Synthesis and Electroless Deposition of Ag	22
2.1.2 Stability of Cu-Ag Nanowires	30
2.2 Tunable Synthesis of Low Aspect Ratio Cu Nanowires	32
2.2.1 Using Glucose Degradation and NaOH Dilution to Control Reaction Kinetics	33
3. Applications for Cu Nanowires	37
3.1 Highly Conductive Nanowire-Based 3D Printing Filament	37
3.1.1 Introduction to 3D Printed Electronics.....	37

3.1.2 Effect of Filler Morphology and Concentration on the Resistivity of the Filament	41
3.1.3 Production of 3D Printing Filament	45
3.1.4 Resistivity of Cu-Ag Nanowire Filament.....	48
3.1.5 3D-Printed Inductive Charging Coil as a Proof of Concept.....	48
3.1.6 Temperature Resistance and Current Capacity	50
3.1.7 Conclusion.....	55
3.2 Stretchable Conductor	55
3.3 Flow-Through Electrode.....	59
4. Single-Crystal Electrochemistry to Understand the Role of I ⁻ in Cu Nanoplate Growth	65
4.1 Synthetic Observations of Cu Nanoplate Growth.....	66
4.2 Electrochemical Measurements of Cu Reduction Rates on Cu Single-Crystal Electrodes.....	70
4.3 Conclusion.....	80
5. Conclusions.....	82
6. Experimental Procedures.....	84
6.1 Multigram-Scale Synthesis of Cu Nanowires.....	84
6.1.1 High Aspect Ratio Cu Nanowires.....	84
6.1.2 Synthesis of Ag and Cu-Ag Nanowires	85
6.1.3 Preparation of Samples Containing High Aspect Ratio Nanowires	87
6.1.4 Cu-Ag Nanowire Filament Production and 3D Printing.....	88
6.1.5 Low Aspect Ratio Nanowires.....	89

6.2 Synthesis and Analysis of Cu Nanocrystals	91
6.2.1 Synthesis of Cu nanocrystals	91
6.2.2 Seeded Growth of Cu Nanoplates	92
6.2.3 Electrochemical Methods	92
References	95
Biography	110

List of Tables

Table 1: Summary of One-Pot Syntheses for Cu Nanowires	7
Table 2: Labor and Materials Cost of Cu Nanowire Production at Low and High Volume	28
Table 3: Labor and Materials Cost of Ag Coating at Low and High Volume	29
Table 4: The Resistivity of Various Conductive 3D Printing Filaments and their Fillers.	39
Table 5: Dimensions of Ag and Cu Fillers.	42
Table 6: Physical Properties of Carbon Paper, Graphite Felt, Reticulated Vitreous Carbon, Ni Foam, and Cu Nanowire Felt.....	64
Table 7: The Crystal Structure of Metal Nanoplates Reported in Previous Research.....	68

List of Figures

Figure 1: Schematic of Cu nanocrystal growth stages in a colloidal synthesis.	3
Figure 2: Schematic of the two reduction pathways: (a) solution reduction and (b) surface reduction.	4
Figure 3: Schematic showing the role of capping agents in directing the growth of a single-crystal seed into either a cube or octahedra.	5
Figure 4: Distribution of nanowire-related publications by metal.	6
Figure 5: Growth mechanism of EDA-mediated pentagonally-twinned Cu nanowires. ...	9
Figure 6: Gram-scale synthesis of Cu nanowires using hydrazine as the reducing agent.	10
Figure 7: Schematic of the hydrothermal reaction and diagram of the formation of Cu nanowires and nanoplates.	13
Figure 8: Schematic showing the proposed mechanism for the bromide-mediated anisotropic growth of Cu particles in which Br ⁻ preferentially bind to the (111) surfaces.	13
Figure 9: SEM images of Cu nanocrystals synthesized with and without Cl ⁻	15
Figure 10: Proposed growth mechanism of Cu nanowires.	16
Figure 11: Graph demonstrating LSV at the mixed potential and the use of a Tafel plot to extract current density.	18
Figure 12: Tafel plots for Cu(111) and Cu(100) electrodes in solutions containing (a) CuCl ₂ and (b) Cu(NO ₃) ₂ with HDA and ascorbic acid.	19
Figure 13: Schematic showing the alternative growth mechanism of Cu nanowires obtained from single-crystal electrochemistry results and DFT calculations.	20
Figure 14: Multigram-scale synthesis of Cu nanowires.	23
Figure 15: Multigram-scale Ag coating procedure.	25
Figure 16: Characterization of the core-shell structure of Cu-Ag nanowires.	26

Figure 17: Stability tests (n = 3) of Cu-Ag nanowires with varying mol ratios of Ag to Cu.	31
Figure 18: Tunable, self-heated synthesis of short Cu nanowires.....	34
Figure 19: Temperature profile of NaOH with varying reactants.	35
Figure 20: SEM images of the Cu nanowires with average length (L , n = 200) and diameter (D , n = 100).	36
Figure 21: Resistivity of filament composites containing various Ag and Cu fillers at different volume percent (vol%).	42
Figure 22: Determination of composite quality and filler dispersion.....	43
Figure 23: Production of nanowire-based 3D printing filament.	46
Figure 24: DFOM images comparing the lengths of Cu-Ag nanowires in composite (a) before and (b) after extruding into filament.....	47
Figure 25: Proof of concept 3D printed inductive charging coil.	49
Figure 26: Resistivity of the conductive filament vs. temperature. The melting points of pure PCL and PCL with Cu-Ag nanowires are indicated by dashed lines.	51
Figure 27: Thermal limitations of nanowire-based filament.....	52
Figure 28: Production of a stretchable conductor using Cu-Ag nanowires.....	57
Figure 29: R/R_0 behavior over 50 cycles at 50% strain.....	58
Figure 30: Demonstration of conductor stretchability.....	59
Figure 31: Schematic illustration of this study's effort to explore how reducing the size of the fibers in a flow-through electrode to the nanoscale can improve productivity.	62
Figure 32: Performance of nanowire-based flow-through electrode.....	63
Figure 33: Cu nanostructures synthesized with HDA, AA, and different combinations of Cu precursors and halide ions	67

Figure 34: Two models demonstrating the atomic arrangement of Cu in hexagonal nanoplates using an FCC packing of spherical magnets.....	69
Figure 35: SEM images of Cu nanoplates after seeded growth in which Cu nanoplates from Figure 33c were added to a Cu nanowire growth solution (HDA-Cl).....	70
Figure 36: (a–c) Tafel plots for two Cu single-crystal electrodes obtained with the same reaction solutions as Figure 33a–c, respectively. (d–f) The corresponding LSVs.	72
Figure 37: The current densities at mixed potential (j_{mp}) measured from the Tafel plots shown in Figure 36a–c. The values in the graph correspond to average j_{mp}	73
Figure 38: Electrochemical and synthetic results demonstrating the passivation and activation effects of I ⁻ on {111} and {100} facets.....	75
Figure 39: The role of competitive adsorption of Cl ⁻ and I ⁻ in the growth of Cu nanoplates.	77
Figure 40: LSVs for the (100) electrode in an HDA-Cl solution, and the (111) electrode in an HDA-Cl-I solution.....	79

Acknowledgments

I would first like to thank Prof. Benjamin Wiley for his patient guidance, enthusiastic encouragement, and useful critiques during my time at Duke, and without whom this work would not have been possible. I would also like to thank my colleagues, especially Dr. Myung Jun Kim and Dr. Shengrong Ye, for their wonderful collaboration, advice, and friendship. Furthermore, I would like to acknowledge my undergraduate research advisor, Prof. Ellane Park, for her kindhearted mentorship and continued support, and Dr. Richard Gregor, for his boundless enthusiasm for all things chemistry and for inspiring me to pursue a career in the field. Finally, I would like to express my deepest gratitude to my family and friends, who have always believed in me and have never let me set limits on what I can accomplish.

1. Introduction

Metal nanocrystals are compelling materials that bridge the gap between bulk materials and atomic or molecular structures. They are characterized by having at least one dimension between 1–100 nm with single or polycrystalline atomic arrangement. Nanocrystals exhibit a wide range of unique properties based on their size, shape, composition, and structure, which can be individually manipulated to maximize their efficacy in fields including catalysis,¹⁻² electronics,³⁻⁵ sensing,⁶⁻⁷ and medicine.⁸⁻¹¹ For example, hollow, porous Au nanocages functionalized with thermally responsive polymers have been developed for potential use in controlled drug delivery.¹² Small molecules were loaded into the hollow core of the nanocages and released via laser excitation. The photothermal properties of the Au nanocages induced the collapse of the polymer coating that helped contain the loaded molecules. Furthermore, the nontoxic and noncorrosive property of Au makes the nanocages ideal for biomedical applications.

The overarching theme of metal nanocrystal research is that they exhibit exciting functionalities that can give rise to new and improved technologies. The potential impact of metal nanocrystals in industrial processes, biomedical applications, and consumer products is immense. However, in order to realize this potential, metal nanocrystals must be produced in large quantities using simple and cheap methods, while still maintaining excellent control over their morphology.

This work aims to address the practicality of utilizing Cu nanocrystal for electronic and catalytic applications by presenting a multigram-scale synthesis of oxidation-resistant Cu nanowires, demonstrating a tunable synthesis for low-aspect-ratio Cu nanowires, and using single-crystal electrochemistry to study the growth mechanism of Cu nanoplates.

1.1 Colloidal Growth of Anisotropic Metal Nanocrystals

One of the most effective ways to tailor the properties of metal nanocrystals is by changing their shape. The classic example used to demonstrate the importance of shape-control in colloidal nanocrystal synthesis is the role size plays in determining the localized surface plasmon (LSPR) properties of Au and Ag nanocrystals. Shape and size dictate the number, position, and intensity of LSPR peaks; thus, the ability to control those properties makes them valuable for a wide range of applications in sensing and imaging.¹³⁻¹⁵

In the colloidal synthesis of anisotropic metal nanocrystals, shape control begins with the nucleation of a metal precursor (Figure 1). The metal ions reduce and nucleate into particles, which form faceted seeds that help determine the final structure of the nanocrystals. Growth then occurs through two possible pathways: atomic addition or oriented attachment. In atomic addition, individual atoms adsorb onto the surface of the seeds, while in oriented attachment, several seeds coalesce to form the final structure. This work will focus on Cu nanocrystals that grow via atomic addition.

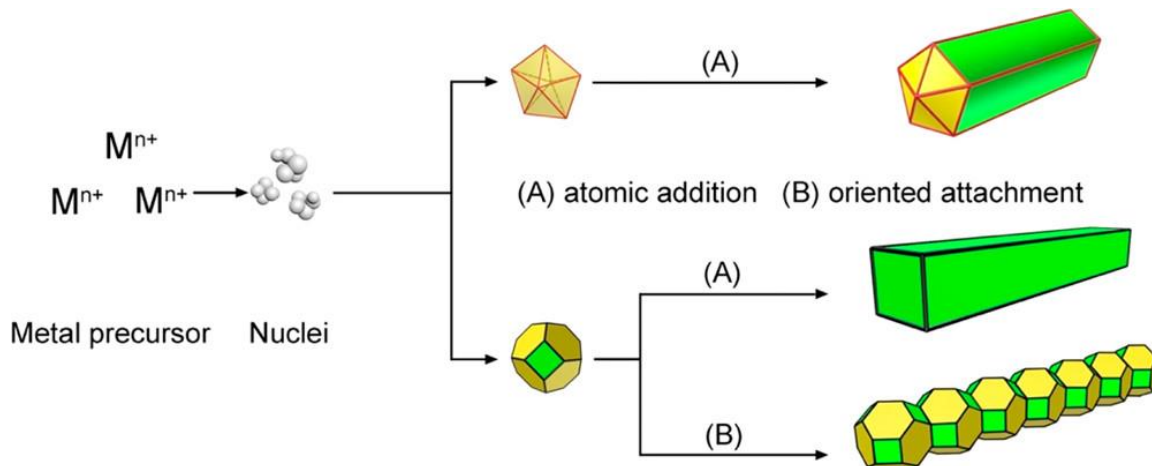


Figure 1: Schematic of Cu nanocrystal growth stages in a colloidal synthesis.

The reduction of the metal precursor and atomic addition can be described by a simple redox reaction in which the oxidation of the reducing agent provides sufficient electrons to reduce the metal.



Figure 2 shows that the reduction of the metal precursor can occur either through solution reduction (i.e., precursor is reduced in the solution before adsorbing onto a seed surface) or surface reduction (i.e., precursor adsorbs on the surface of a seed before undergoing reduction),¹⁶⁻¹⁸ with the latter being more likely to occur in the presence of seeds. The key to synthesizing metal nanocrystals of different shapes is to control the facets where atomic adsorption occurs.

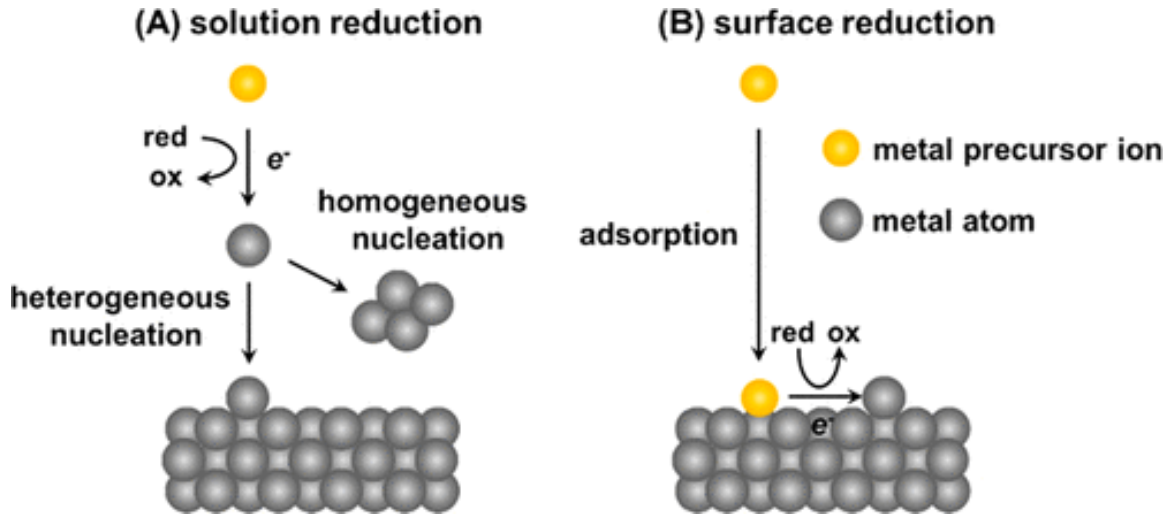


Figure 2: Schematic of the two reduction pathways: (a) solution reduction and (b) surface reduction.^{16, 19}

One way to dictate atomic adsorption is through the use of shape-directing agents, which include capping agents and facet-selective promoters.²⁰⁻²³ The guiding hypothesis is that these shape-directing agents preferentially adsorb on certain facets of the nanocrystal, altering their surface energies and in turn causing growth to deviate from thermodynamically favorable structures. For example, Wulff constructions of face-centered cubic (FCC) metals predict that the thermodynamically favored structure is a truncated octahedron composed of both {111} and {100} facets.²⁰ However, Figure 3 shows that the addition of certain capping agents results in either octahedrons covered exclusively by eight {111} facets or nanocubes enclosed by six {100} facets. The red capping agent preferentially adsorbs on the {100} surfaces, physically blocking atomic addition and lowering their surface free energy. Atomic addition is limited to {111} surfaces

containing higher free energies until the entire nanocrystal is enclosed by the lower energy {100} facets.²⁰

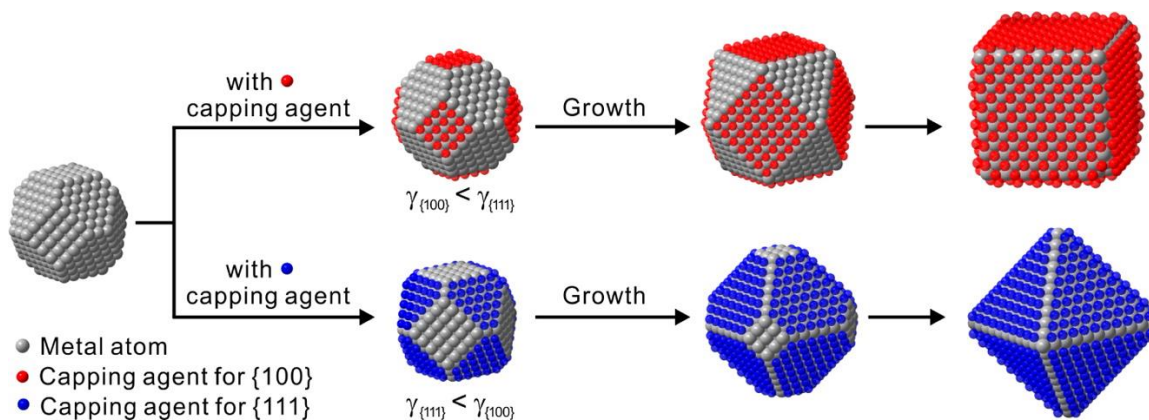


Figure 3: Schematic showing the role of capping agents in directing the growth of a single-crystal seed into either a cube or octahedra.²⁰

More dramatic deviations from thermodynamic predictions are exemplified by the anisotropic growth of nanowires and nanoplates, which have surface-to-volume ratios much greater than nanoparticles. Nanowires and nanoplates result from kinetically controlled growth, where preferential adsorption of shape-directing agents causes a growth rate differential between crystal facets.²¹ In light of this diverse collection of morphologies, obtaining a better understanding of the interactions between shape-directing agents and specific crystal facets is a crucial step to controlling and tailoring syntheses of nanocrystals for their wide range of applications.

1.2 Synthesis of Pentagonally-Twinned Cu Nanowires

Chapter 2 of this dissertation presents the synthesis of Cu nanowires, which have been used in the fields of optoelectronics, energy storage and conversion, catalysis, wearable electronics, and thermal management.²⁴ Among metal nanowires materials, Cu nanowires lag behind Ag and Au in terms of the number of 1D metal nanocrystal publications (Figure 4). Preference over Ag and Au is understandably high due to their excellent stability, conductivity, and unique LSPR properties that make them suitable for catalysis, plasmonics, and electronics.^{19, 25-32} However, bulk Cu is 45% more conductive than Au, only 6% less conductive than Ag, but is more abundant, less expensive, and has a lower carbon footprint.³³⁻³⁴ The economic viability of Cu nanowires, paired with the wide range of their demonstrated applications, makes them compelling materials.

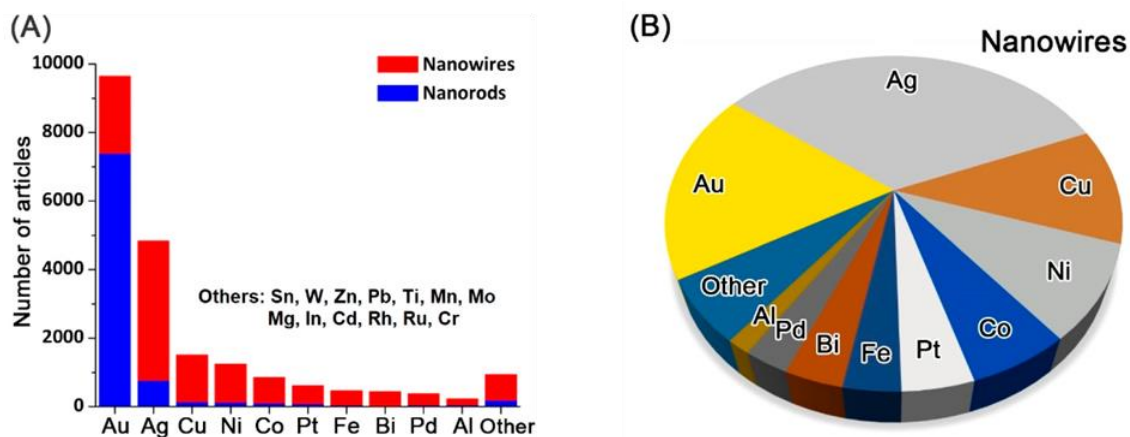


Figure 4: Distribution of nanowire-related publications by metal. (a) The number of articles about metal nanowires and nanorods sourced from the Web of Science database. (b) Relative distribution of articles discussing metal nanowires.¹⁹

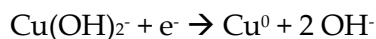
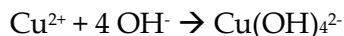
In addition to intrinsic conductive properties, the thin diameter of Cu nanowires enables them to be flexible and optically transparent, while their length facilitates the formation of percolative networks at low concentrations. Large aspect ratio Cu nanowires can also form networks that possess high porosity and high surface area-to-volume ratios. Taking advantage of these structure-property relationships to maximize the utility of Cu nanowires begins with understanding how they grow.

Cu nanowires have been synthesized using a variety of methods including chemical vapor deposition,³⁵ template-assisted growth,³⁶ and electrospinning,³⁷ but the most studied method are one-pot, solution-phase syntheses because they have high throughput and simplified reaction procedure where nucleation and growth occur in the same reaction solution.³⁸⁻⁴³ A typical one-pot synthesis contains a Cu precursor, a reducing agent, and a shape-directing agent, which are summarized in Table 1.

Table 1: Summary of One-Pot Syntheses for Cu Nanowires

Cu Precursor	Reducing Agent	Shape-Directing Agent	Citation
CuCl ₂	Glucose	Alkylamines: dodecylamine (DDA), tetradecylamine (TDA), hexadecylamine (HDA), octadecylamine (ODA), oleylamine (OLA)	44-46
	Ascorbic Acid	HDA	47
Cu(NO ₃) ₂	Hydrazine	Ethylenediamine	39-40
	Glucose		48 (this work)
CuSO ₄	Phosphite	Sodium dodecyl benzenesulfonate	38

This work presents two different syntheses that utilize $\text{Cu}(\text{NO}_3)_2$ as the Cu precursor, glucose and hydrazine as the reducing agents, and ethylenediamine (EDA) as the shape directing agent. Sodium hydroxide (NaOH) also acts as a complexing agent to assist in the reduction of Cu ions. The equations below show Cu ion reduction in a basic solution in which a Cu^{2+} ion complexes with OH^- molecules to form the more readily reduced $\text{Cu}(\text{OH})_4^{2-}$ complex. Finally, hydrazine or glucose provides two electrons to reduce Cu^{2+} to Cu^{1+} and Cu^{1+} to Cu^0 .



It was previously believed that EDA promotes anisotropic growth by acting as a capping agent restricting Cu atomic adsorption on the (100) side facets.⁴²⁻⁴³ However, the molecular length of EDA is much shorter compared to other alkylamines, making it unlikely that it forms a self-assembled monolayer than can sterically block Cu atomic addition.⁴⁹ An electrochemical study utilizing Cu(111) and Cu(100) electrodes to simulate the end and side facets of pentagonally-twinned Cu nanowires, respectively, clarified that EDA promotes anisotropic growth by selectively inhibiting oxidation on the (111) facets at the ends of growing Cu nanowires (Figure 5).⁵⁰

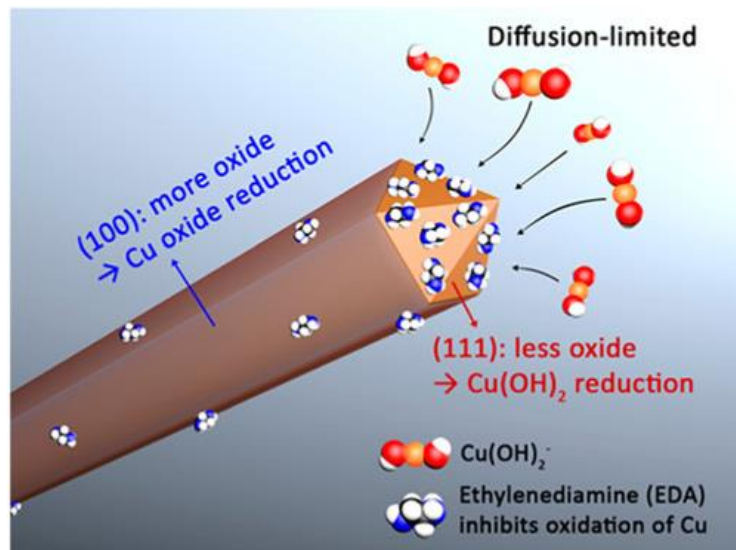


Figure 5: Growth mechanism of EDA-mediated pentagonally-twinned Cu nanowires.⁵⁰

1.3 Current Limitations to the Utilization of Cu Nanowires

Despite our knowledge of Cu nanowire synthesis, their industrial viability is still questionable due to the fact that the current synthetic methods produce nanowires at a small scale over several hours, which cannot feasibly meet any market demand. One of the more promising contributions to the large-scale production of Cu nanowires was reported by Rathmell et al., which produced 1.2 g of nanowires in 1 h (Figure 6).⁴⁰

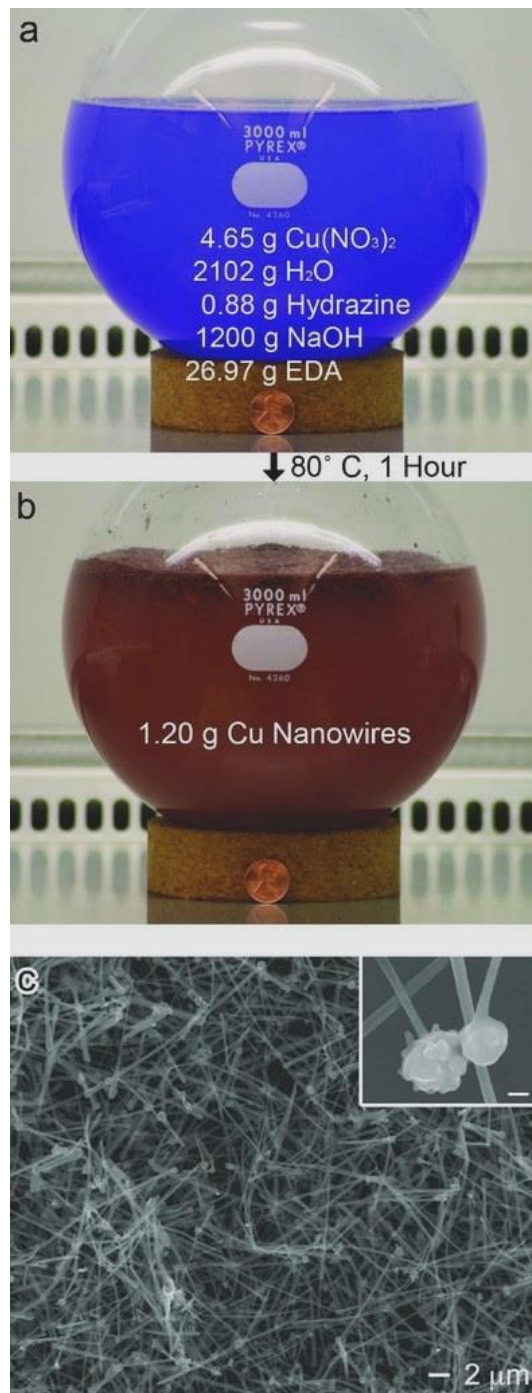


Figure 6: Gram-scale synthesis of Cu nanowires using hydrazine as the reducing agent. Pictures of the reaction (a) before and (b) after the growth of Cu nanowires at 80°C for 1 h. (c) SEM images of the Cu nanowire product with an average length of $10 \pm 3 \mu\text{m}$ and an average diameter of $90 \pm 10 \text{ nm}$.⁴⁰

However, the reaction utilized hydrazine as a reducing agent, which is highly flammable and a known carcinogen, making it undesirable for large-scale syntheses, especially at the industrial scale. Glucose is a safe and non-toxic alternative; however, it is a weaker reducing agent compared to hydrazine. Moreover, current reaction conditions for glucose-based syntheses involve long reaction times upwards of size hours,⁴¹ and high temperature and pressure.⁴⁶ There are also no current glucose-based syntheses that yield Cu nanowires in the gram scale.

Additionally, the utilization of Cu nanowires remains problematic because they easily oxidize. Methods for preventing or reducing the oxidation of Cu nanowires primarily include annealing under hydrogen gas,⁵¹ using acetic acid to dissolve Cu oxide,⁵² and encapsulating the wires in a protective shell of noble metals,⁵³ graphene,⁵⁴ or plastic.⁵⁵ While the quantity of nanowires that can be annealed is limited only by the size of the sample relative to the furnace, an alternative method for producing oxidation-resistant Cu nanowires in bulk is necessary for applications and samples that cannot be exposed to high temperatures required for annealing.

To help overcome these current limitations, Chapter 2 discusses a glucose-based multigram-scale synthesis of Cu nanowires that yielded 4.4 g of Cu nanowires in 1 h under mild reaction conditions. The Cu nanowires were then coated with an oxidation-resistant shell of Ag in a method that yielded 22 g in 1 h. Furthermore, the glucose-based synthesis was modified to yield short Cu nanowires with tunable aspect ratios. Finally, the Cu

nanowires were used in applications that benefited from their unique properties, as well as their availability in large quantities.

1.4 Cu Nanoplate Growth and Applications

Similar to Cu nanowires, 2D Cu nanocrystals such as nanoplates and nanosheets have also been of interest due to their catalytic and electrically conductive properties. Cu nanoplates have been successfully used as a filler for a semi-transparent conductive ink.⁵⁶ Cu and Cu-based nanoplates and sheets have also been used as electrocatalysts for the reduction of 4-nitrophenol,⁵⁷ carbon monoxide,⁵⁸ and carbon dioxide,⁵⁹ and oxidation of methanol.⁶⁰ Despite their promise, very little is known about the growth mechanism of 2D Cu nanocrystals.

As with the synthesis of metal nanocrystals, shape-directing agents play a pivotal role in the growth of Cu nanoplates. Lee and coworkers demonstrated a synthesis in which adding iodide ions (I⁻) to a Cu nanowire growth solution resulted in Cu nanoplates (Figure 7). Venkatasubramanian et al. also showed that the addition of bromide ions (Br⁻) caused a change in nanocrystal shape from a polyhedral Cu nanoparticle with a well-defined crystal structure to an anisotropic Cu nanoplate (Figure 8). These results clearly indicate that halide ions act as effective shape-directing agents in the growth of Cu nanoplates.

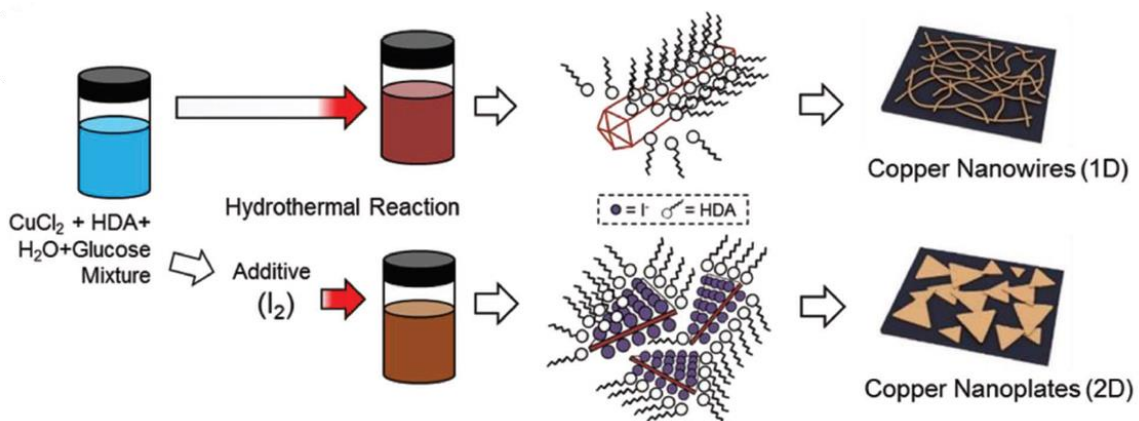


Figure 7: Schematic of the hydrothermal reaction and diagram of the formation of Cu nanowires and nanoplates. The addition of I_2 induces a shift in the growth mode of the Cu nanocrystal as it passivates the (111) basal surface of the Cu nanoplates, resulting in 2D lateral growth.⁵⁶

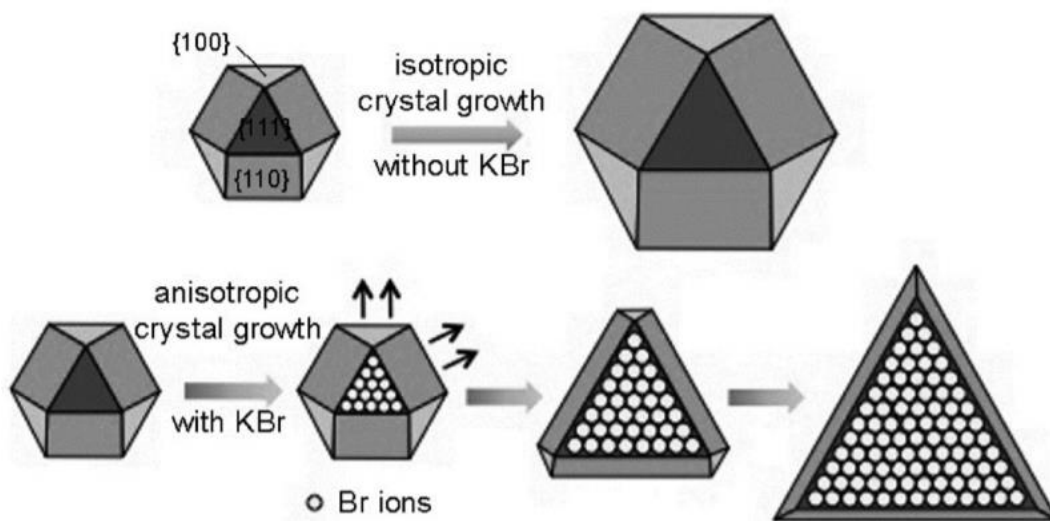


Figure 8: Schematic showing the proposed mechanism for the bromide-mediated anisotropic growth of Cu particles in which Br preferentially bind to the (111) surfaces.⁶⁰

Lee hypothesized that I⁻ preferentially adsorbed on the (111) basal facets of the nanoplates, limiting Cu reduction to the side facets. In this case, HDA acted as a stabilizer for the adsorbed I⁻, although it typically believed to be a facet-selective capping agent for (100) surfaces in Cu nanowire growth.⁶¹ The facet-selective capping behavior of I⁻ have also been reported for Au nanoplates.⁶² In a similar vein, Venkatasubramanian also attributed the anisotropic growth of Br-induced Cu nanoplates to the selective passivation of the (111) basal surfaces with Br⁻.

While these proposed growth mechanisms seem plausible, they were formed through observation of the synthesized products instead of experimental methods. It remains unclear why these halide ions preferentially adsorb on {111} crystal facets and not others. Moreover, in the case of the Lee study shown in Figure 7, the role of chloride ions (Cl⁻) on the growth of the nanoplates is also unclear. Thus, further research is necessary to clarify the specific role of halide ions on the growth mechanism of Cu nanoplates.

1.5 Using Single-Crystal Electrochemistry to Explain the Growth Mechanism of Cu Nanocrystals

Single-crystal electrochemistry has been used to study the role of Cl⁻ on the role of Cu nanowire growth.⁴⁷ As shown in Figure 9, Cl⁻ was necessary to produce nanowires in the presence of HDA and ascorbic acid, and that leaving out Cl⁻ resulted in isotropic Cu nanoparticles. However, the previously proposed mechanism for the growth of the nanowires only attributed their anisotropic growth to the selective passivation of {100}

side facets by HDA, making no mention of the role of Cl^- ,⁶¹ as shown by the schematic in Figure 10.

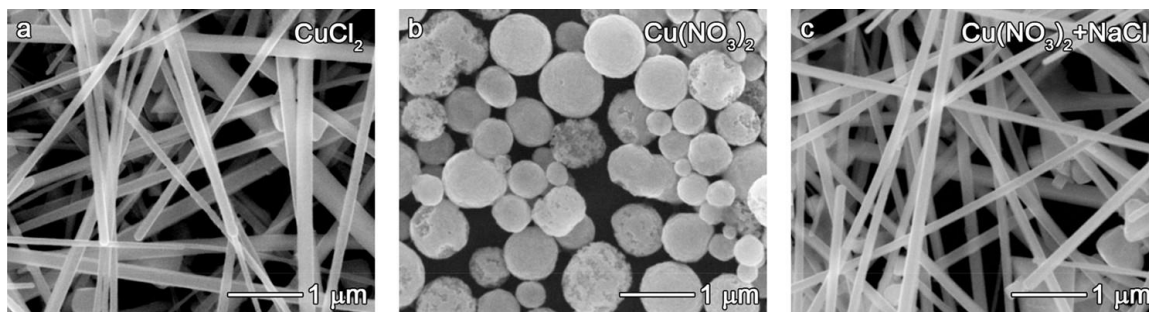


Figure 9: SEM images of Cu nanocrystals synthesized with and without Cl^- . (a) Cu nanowires synthesized using a CuCl_2 precursor, (b) Cu nanoparticles synthesized using a $\text{Cu}(\text{NO}_3)_2$ precursor, and (c) Cu nanowires synthesized with $\text{Cu}(\text{NO}_3)_2$ and NaCl additive. All three growth solutions also contained HDA and ascorbic acid.⁴⁷

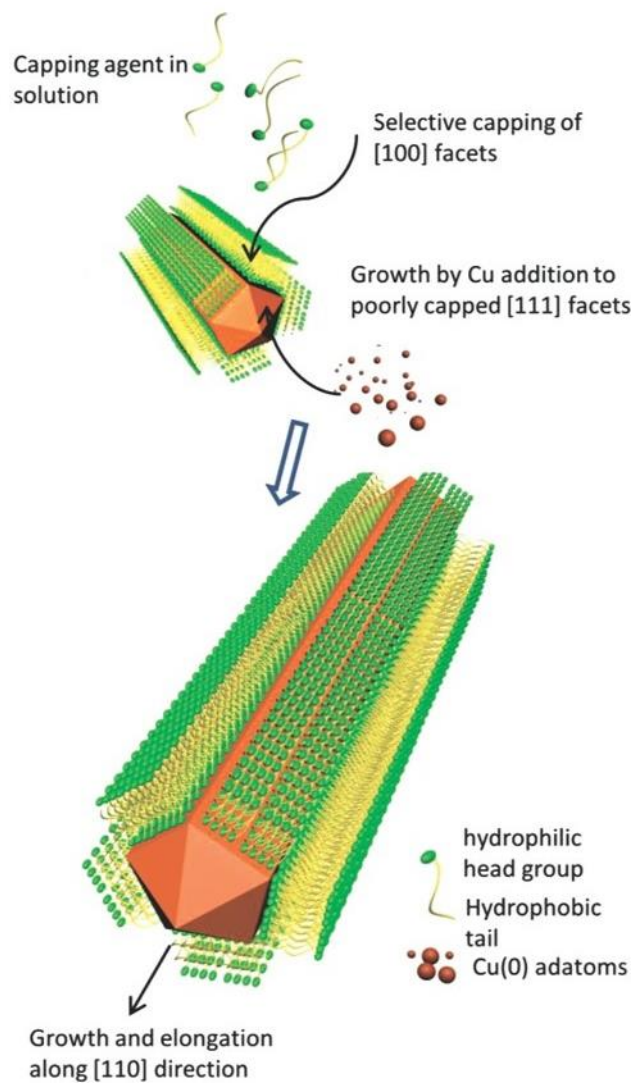


Figure 10: Proposed growth mechanism of Cu nanowires. HDA selectively passivated the {100} facets, limiting Cu atomic addition to the {111} end facets and resulting in the anisotropic growth of Cu nanowires.⁶¹

To elucidate the role of Cl⁻ in the growth of Cu nanowires, Kim et al. developed a method using Cu(111) and Cu(100) single-crystal electrodes to replicate the crystal facets of the nanowires and measure their electrochemical activity in the nanowire growth

solution. This method employed mixed potential theory, which has been used for describing the spontaneous and simultaneous electrochemical oxidation and reduction reactions including electroless deposition and galvanic displacement.⁶³⁻⁶⁵ It states that in a spontaneous redox reaction, the rates of oxidation and reduction should be equal because electrons cannot be accumulated or depleted in the system.

Within the context of nanocrystal growth, the mixed potential (E_{mp}) is where atomic adsorption occurs because all the electrons produced by the oxidation of the reducing agent goes towards the reduction of the metal precursor. If linear sweep voltammetry (LSV) is performed with a solution containing both the reducing agent and the metal precursor, the net current (j_{net}) at E_{mp} is 0, meaning that the two electrochemical reactions are balanced (or the rates of two electrochemical reactions are identical) as shown in Figure 11a. However, the zero current does not mean no electrochemical reactions are occurring at E_{mp} . The j_{net} is composed of both the partial current density of metal reduction (j_{red}) and reducing agent oxidation (j_{oxi}), such that $j_{net} = j_{oxi} - |j_{red}|$. Thus, at E_{mp} , $j_{oxi} = |j_{red}|$ and $j_{net} = 0$. Thus, E_{mp} represents the potential at which spontaneous atomic addition occurs, thereby Cu nanocrystal growth. Moreover, because the reduction and oxidation rates are equal and both are represented by j_{oxi} and j_{red} , either can be used to measure the rate of Cu deposition. However, a Tafel plot is necessary to extract these values.

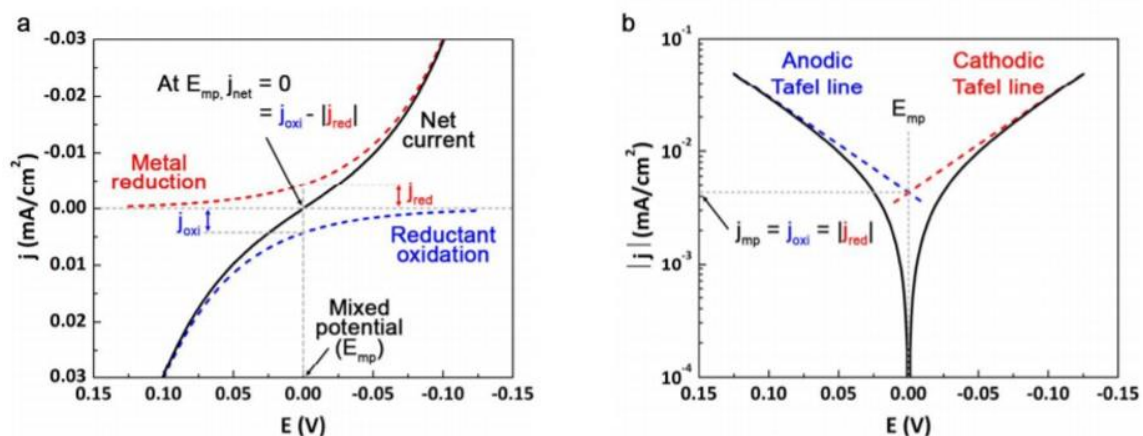


Figure 11: Graph demonstrating LSV at the mixed potential and the use of a Tafel plot to extract current density. (a) Example of current density and potential curves for metal ion reduction and reducing agent oxidation, and the corresponding net current. (B) Tafel plot obtained from (a).⁴⁷

The Tafel plot in Figure 11b shows the relationship of $\log |j|$ vs. potential (E), and a linear relationship (called a Tafel line) can be drawn between j and E under charge transfer-limited conditions.^{47, 66-67} Tafel lines can be extrapolated from either the anodic or cathodic half reactions to obtain the j_{mp} , which is the value at which it intersects with E_{mp} .

The Tafel plots of Cu(111) and Cu(100) single-crystal electrodes in Cu nanowire growth solution containing both Cl^- and HDA resulted in a 15x higher current for the Cu(111) electrode (Figure 12a), whereas in the nanoparticle growth solution only containing HDA (i.e., no Cl^-), both the Cu(111) and Cu(100) electrodes had equally low currents (Figure 12b), meaning that both surfaces were strongly passivated by an HDA self-assembled monolayer (SAM). These electrochemical results pointed to two important discrepancies from the previously accepted hypothesis: (1) Cl^- induces facet-selective

atomic adsorption on the (111) surface, and (2) HDA passivates both the (111) and (100) surfaces.

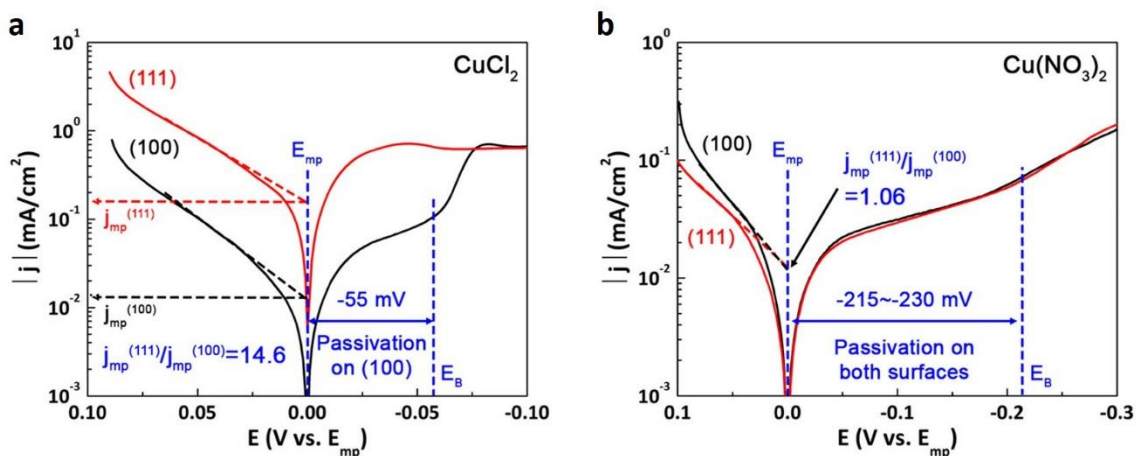


Figure 12: Tafel plots for Cu(111) and Cu(100) electrodes in solutions containing (a) CuCl_2 and (b) $\text{Cu}(\text{NO}_3)_2$ with HDA and ascorbic acid.⁴⁷

Finally, density functional theory (DFT) calculations confirmed that without Cl^- , HDA forms self-assembled monolayer (SAM) on {111} and {100} surfaces. At a Cl^- surface coverage of 1/3 monolayer (ML) on the {111} facets, Cl^- disrupted the HDA SAM. DFT calculations showed that HDA was physisorbed on the {111} facets, thus the repulsion from Cl^- was sufficient to overcome the binding energy of HDA on the Cu surface, disruption the SAM. However, at the same Cl^- surface coverage on the {100} facets, the HDA SAM remained chemisorbed, keeping the SAM intact. As a result, at Cl^- concentrations that were shown to result in Cu nanowires, Cl^- disrupted the HDA SAM

on the {111} facets at the ends of growing nanowires and facilitated Cu atomic addition, while the HDA SAM continued to passivate the {100} side facets (Figure 13).

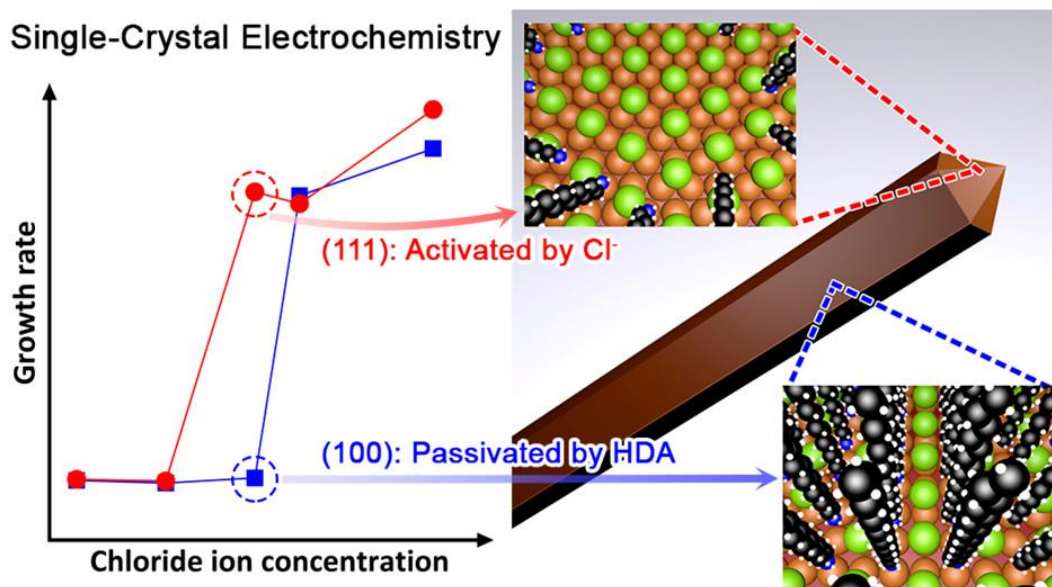


Figure 13: Schematic showing the alternative growth mechanism of Cu nanowires obtained from single-crystal electrochemistry results and DFT calculations.⁴⁷

Single-crystal electrochemistry is a powerful method that enables the investigation of shape-directing agents in growth solutions by measuring the rate of metal reduction on specific crystal facets simulated by single-crystal electrodes. Chapter 3 of this dissertation discusses how this method was used to elucidate the role of I^- on the growth of Cu nanoplates. The study provided experimental data that suggests the growth of Cu nanoplates is due to the competitive adsorption of Cl^- and I^- on both the {111} and {100} facets.

2. Improvements in the Colloidal Synthesis of Cu Nanowires

This section discusses progress towards improving the industrial viability of Cu nanowires. A solution phase, multigram-scale synthesis for long Cu nanowires ($45 \pm 15 \mu\text{m}$ in length) was developed, which yielded over 4 g of Cu nanowires in 1 h under relatively mild reaction conditions. Oxidation of the nanowires was prevented by developing a method that produced 22 g of Ag-coated Cu nanowires (Cu-Ag nanowires), enabling the nanowires to remain electrically stable after being exposed to heat and humidity. For the first time, large quantities of oxidation-resistant Cu nanowires were readily available, leading to their utilization in applications such as a conductive 3D printing filament,⁴⁸ a flow-through electrode,⁶⁸ and a stretchable conductor.⁶⁹ Moreover, a tunable synthesis for short nanowires (1–5 μm in length) was also developed, which presented a simple technique for modifying the aspect ratio of the nanowire product. A synthetic approach was used to understand the synergistic effect of NaOH and glucose on the reaction kinetics, enabling us to produce nanowires of different lengths by modifying the concentration of the reducing agent.

2.1 Multigram-Scale Synthesis of High Aspect Ratio Cu-Ag Nanowires

2.1.1 Glucose-Based Cu Nanowire Synthesis and Electroless Deposition of Ag⁴⁸

While gram-scale syntheses of long Cu nanowires have been previously reported by Rathmell et al. and others,^{39-40, 51, 70-72} bringing us one step closer to meeting potential market demands, some key limitations exist that make them unideal methods for producing large quantities of Cu nanowires. First, they utilize hydrazine, a highly toxic chemical, as the reducing agent. Second, they require large amounts of highly concentrated NaOH (>12 M). Efforts have been made to replace hydrazine with glucose as the reducing agent because it is non-toxic, however, these syntheses require elevated temperatures (>100°C) and pressures over several hours, and the resulting nanowires are coated with HDA or ODA, making them very difficult to disperse in the aqueous solutions.^{41, 46, 73} This work demonstrates that it is possible to replace the hydrazine in the NaOH-EDA reaction with glucose. The use of glucose eliminates issues with disposal of waste containing a highly toxic chemical, and enables the reduction of the amount of NaOH necessary for the reaction from 12 to 6.5 M. The reaction could be carried out at lower temperatures (60°C) relative to previous syntheses using alkylamine and glucose without NaOH (>100°C) because the conversion of glucose to reductones (the reducing agent) is accelerated in the presence of NaOH.⁷⁴⁻⁷⁶

Figure 14a shows the reaction was scaled up to 10 L and was completed in only 1 h. The concentration of the reactants are as follows: 6.5 M NaOH, 9 mM Cu(NO₃)₂, 188 mM EDA, and 82 mg/mL glucose. These conditions resulted in Cu nanowires that had an average length of 45 ± 15 μm (Figure 14b) and 240 ± 95 nm in diameter (Figure 14c). The 10 L reaction had an 85% yield and produced 4.4 g of Cu nanowires.

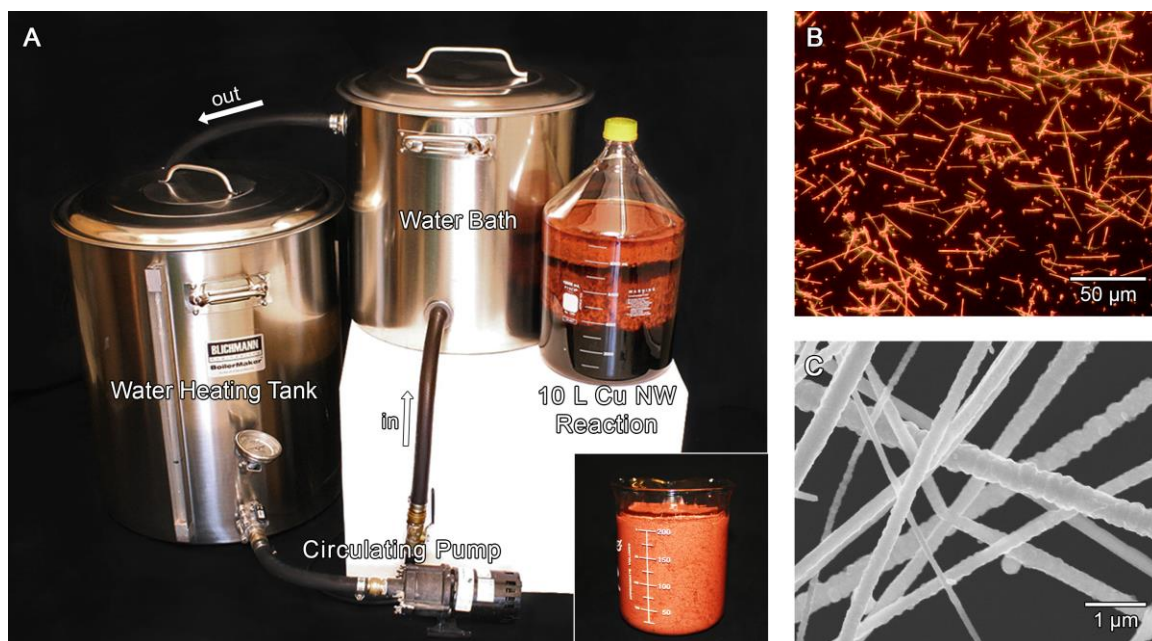


Figure 14: Multigram-scale synthesis of Cu nanowires. (a) Circulating water bath set up for the 10 L synthesis of Cu nanowires. Inset shows ≈22 g of Cu nanowires purified from the reaction. (b) Dark-field optical microscopy (DFOM) image shows the Cu nanowires have an average length of 45 ± 15 μm. (c) An SEM image shows the Cu nanowires have a diameter of 240 ± 95 nm.

In this synthesis, ethylenediamine (EDA) was used as the facet-selective promoter for anisotropic nanowire growth in place of alkylamines. EDA acts as a facet-selective

promoter by prohibiting oxidation on the (111) end facets of nanowires, which encourages Cu atomic addition and causes anisotropic growth.⁵⁰ Unlike alkylamines that form a hydrophobic self-assembled monolayer (SAM) on the surface of nanowires, the use of EDA allows the Cu nanowires to be dispersed in an aqueous solution. Thus, the Cu nanowires could subsequently be coated with Ag using an aqueous, room-temperature electroless deposition method developed by Stewart et al.⁵³ In this electroless deposition process, ascorbic acid removes Cu oxide and reduces Ag ions onto the surface of the Cu nanowires with minimal galvanic displacement, as well as without nucleating Ag nanoparticles in the solution. The reaction was optimized by increasing the concentration of Cu nanowires by a factor of 3 while keeping the concentration of the other reactants the same, resulting in a threefold increase in production efficiency. We also varied the thickness of the Ag coating by modifying the Ag:Cu mol ratio.

As shown in Figure 15a, the reaction was scaled up to 45 L, which yielded 22.5 g of Cu-Ag nanowires in 1 h. To ensure even coating of Ag at such a large volume, AgNO₃ was added at a rate of 0.5 mL/s with a peristaltic pump. After completion of the Ag-coating process, a subtle change in color of the nanowires could be observed, giving a visual indication that the nanowire surface has been modified (Figure 15b). At a Ag:Cu mol ratio of 0.04, a 5-nm diameter increase was observed (Figure 15c), suggesting a 2.5 nm-thick Ag shell was deposited on the Cu nanowires.

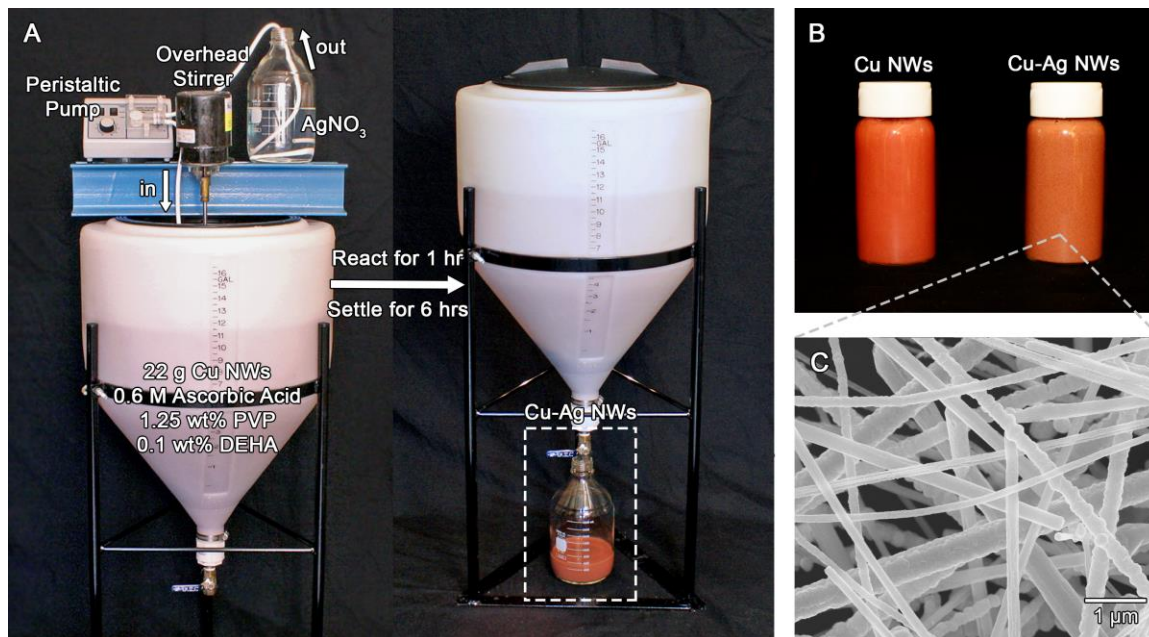


Figure 15: Multigram-scale Ag coating procedure. (a) Tank and pump setup for the 45 L Ag-coating synthesis. Cu-Ag nanowires were collected from the bottom of the tank after settling. (b) A slight color change from orange to brown can be observed after coating the Cu nanowires with Ag. (c) An SEM image shows the Cu-Ag nanowires have a diameter of 245 ± 100 nm.

The successful coating of Ag onto the Cu nanowires was further verified by comparing the X-ray diffractograms of bare Cu nanowires and Cu-Ag nanowires (Figure 16a), which showed the appearance of Ag(111) for the Cu-Ag nanowires that was not present for the Cu nanowires. Scanning transmission electron microscopy-energy dispersive X-ray spectroscopy (STEM-EDS) was performed to confirm the core-shell structure of the Cu-Ag nanowires (Figure 16b–c). The element map in Figure 16b shows a Cu core with a thin Ag shell. A line scan across the diameter of a Cu-Ag nanowire in

Figure 16c shows sharp Ag peaks on both ends of the broader Cu peak, which is indicative of a core-shell structure.

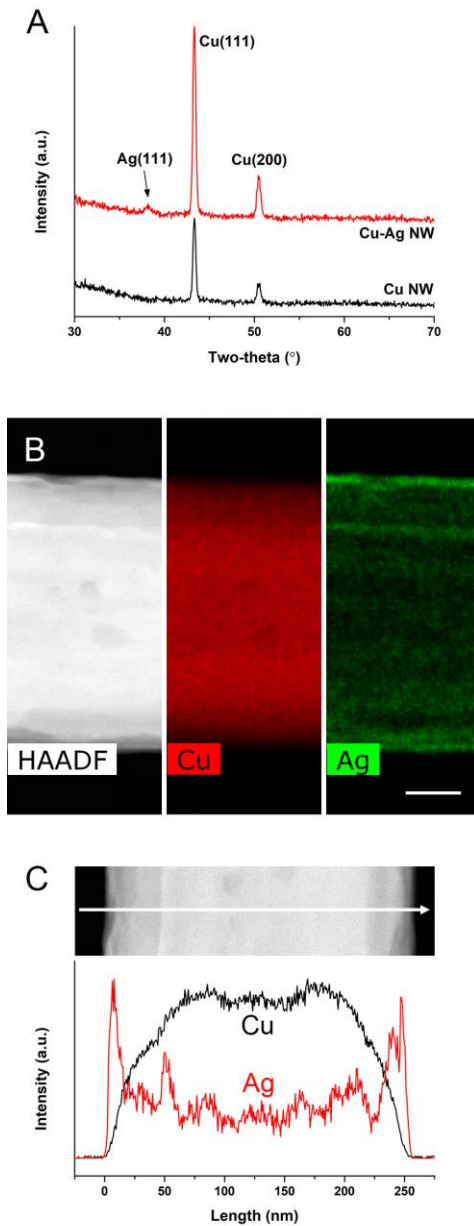


Figure 16: Characterization of the core-shell structure of Cu-Ag nanowires. (a) X-ray diffractograms of Cu nanowires (black) and Cu-Ag nanowires (red). (b) STEM-HAADF

image of a Cu-Ag nanowire with accompanying Cu and Ag EDS maps. The scale bar is equivalent to 50 nm. (c) EDS line scan across the diameter of a Cu-Ag nanowire showing its core-shell structure.

A cost analysis was conducted to determine the economic advantage of increasing the scale of production of Cu-Ag nanowires. Table 2 and 3 show a breakdown of labor and materials costs for Cu nanowire synthesis and Ag coating, respectively. The tables also include a list of prices for starting materials purchased at low volumes (based on prices and quantities ordered by our lab) and high volumes (more representative of a kilogram-scale manufacturing operation). Going from low volume (e.g., Sigma-Aldrich) material prices to high volume material prices without changing the cost of labor decreased the price of the Cu-Ag nanowires from \$16.53 to \$7.16 per gram, including labor and material costs. We note that this price does not include overhead and the cost of waste treatment and/or disposal. Further cost reduction could be obtained by reducing labor costs, which can be accomplished by increasing the reaction volume and increasing production efficiency (grams of nanowires per liter of reaction).

Table 2: Labor and Materials Cost of Cu Nanowire Production at Low and High Volume

LABOR COSTS			
	Batch size	10 L	
	Yield	88% (4.4 g)	
	Reaction and preparation time	5 h	
	Pay rate	\$15.00/h	
	Number of parallel reactions	5	
	Total labor cost per gram	\$3.41	
MATERIALS COST			
	Quantity per gram Cu nanowires	Cost per gram Cu nanowires	
		<i>Low Volume</i>	<i>High Volume</i>
NaOH	1.1 kg	\$1.05	\$0.33
Cu(NO ₃) ₂	4.23 g	\$0.55	\$0.13
EDA	26.14 mL	\$1.27	\$0.52
Glucose	170.45 g	\$0.84	\$0.11
PVP	14.66 g	\$1.27	\$0.15
DEHA	4.89 mL	\$0.76	\$0.09
Total materials cost per gram		\$5.73	\$1.32
Total Labor + Materials Cost Per Gram		\$9.14	\$4.73
MATERIALS COST BREAKDOWN			
Low Volume	Unit Price	Order Quantity	Source
50% NaOH	\$0.95/kg	1396 kg	Brainerd Chemical Company, Dunn, NC
Cu(NO ₃) ₂	\$130.00/kg	2.5 kg	Sigma-Aldrich
EDA	\$48.40/L	2.5 L	Sigma-Aldrich
Glucose	\$4.95/kg	250 kg	Sigma-Aldrich
PVP (10,000 MW)	\$86.67/kg	12 kg	Sigma-Aldrich
DEHA	\$155.00/L	2 L	Sigma-Aldrich
High Volume			
NaOH (s)	\$0.60/kg	1000 kg	Wuhai Xinye Chemical Industry Wuhai, Inner Mongolia, China
Cu(NO ₃) ₂	\$30.00/kg	10 kg	Jinan Boss Chemical Industry Co., Ltd. Ji'nan, Shandong, China
EDA	\$20.00/L	200 L	Shanghai Ruizheng Chemical Technology Co., Ltd., Shanghai, China
Glucose	\$0.66/kg	1000 kg	Hangzhou Yeaster Biotech Co. Ltd. Hangzhou, Zhejiang, China
PVP (15,000 MW)	\$10.00/kg	100 kg	Vega Pharma Limited, Anhui, China
DEHA	\$18.00/L	40 L	Shanghai Ruizheng Chemical Technology Co., Ltd., Shanghai, China

Table 3: Labor and Materials Cost of Ag Coating at Low and High Volume

LABOR COSTS			
	Batch size	44 L	
	Yield	98% (22 g)	
	Reaction and preparation time	3 h	
	Pay rate	\$15.00/h	
	Number of parallel reactions	2	
	Total labor cost per gram	\$1.02	
MATERIALS COST			
	Quantity per gram Cu nanowires	Cost per gram Cu nanowires	
		<i>Low Volume</i>	<i>High Volume</i>
Ascorbic Acid	220.15 g	\$3.88	\$1.10
PVP	18.18 g	\$1.58	\$0.18
AgNO ₃	0.27 g	\$0.91	\$0.12
Total materials cost per gram		\$6.37	\$1.40
Total Labor + Materials Cost Per Gram		\$7.39	\$2.43
MATERIALS COST BREAKDOWN			
Low Volume	Unit Price	Order Quantity	Source
Ascorbic Acid	\$17.64/kg	3.628 kg	Duda Energy, Amazon.com
PVP	\$86.67/kg	12 kg	Sigma-Aldrich
AgNO ₃	\$3.38/g	100 kg	Sigma-Aldrich
High Volume			
Ascorbic Acid	\$5.00/kg	100 kg	Shanghai Ruizheng Chemical Technology Co., Ltd., Shanghai, China
PVP	\$10.00/kg	100 kg	Vega Pharma Limited Anhui, China
AgNO ₃	\$450.00/kg	1 kg	Qingdao Ocean Import and Export Co., Ltd. Shangdong, China

2.1.2 Stability of Cu-Ag Nanowires⁴⁸

In order to produce oxidation-resistant Cu nanowires and widen the scope of its application, it must be coated with enough Ag to stabilizing its surface without significantly increasing the cost of production. To determine the minimal amount of Ag coating to produce stable and conductive nanowires, Cu nanowires were coated with Ag at Ag:Cu mol ratios between 0.03 and 0.07. The Cu-Ag nanowires were then suspended in a nitrocellulose ink and drop-casted into thin films in wells created by double-sided tape. After heating at 150°C for 24 h, Figure 17a shows the resistivity of bare Cu nanowires quickly increased after 1 h until they were no longer conductive. Cu-Ag nanowires with a 0.03 Ag:Cu mol ratio displayed an insignificant increase in resistivity and increasing the Ag coating did not result in further improvement instability. However, when exposed to conditions of 85°C with 85% relative humidity (RH) for over 24 h, the sample coated with 0.03 Ag:Cu became nonconductive after 1 h (Figure 17b). Samples with 0.04–0.07 Ag:Cu were stable after 25 h and increasing the Ag coating did not result in an improvement in stability in these humid conditions. Thus, a minimal amount of Ag coating (>0.04 Ag:Cu) is necessary to protect the nanowires from oxidation. Beyond this amount, there is a negligible decrease in the resistivity of the films.

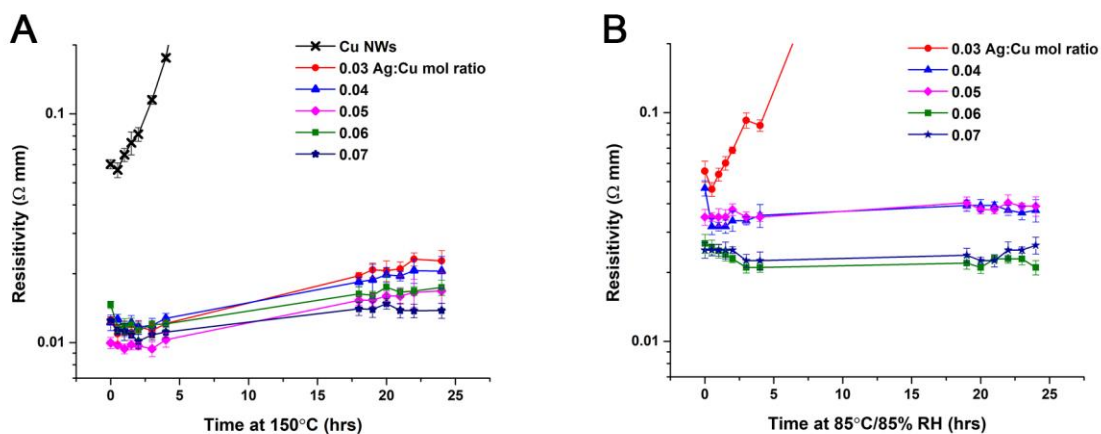


Figure 17: Stability tests ($n = 3$) of Cu-Ag nanowires with varying mol ratios of Ag to Cu. (a) Dry-oven tests at 150°C and (b) humidity chamber tests at 85°C and 85% RH.

The mol ratio of 0.04 Ag:Cu corresponds to a shell thickness of ≈ 3 nm, which was calculated from the mol ratio and the average diameter of the Cu nanowires before coating. Measurement of the Ag shell from the EDS element map shown in Figure 16b suggested a shell thickness of 5–6 nm, which is comparable to the calculated value of 3 nm. The EDS shell thickness is likely larger because the image represents a 2D projection of the pentagonal nanowire, making precise measurement of the shell thickness very difficult. Stewart et al. conducted a similar study for Cu-Ag nanowires ($28 \pm 10 \mu\text{m}$ in length, 79 ± 22 nm in diameter) and showed a minimum shell thickness of 5 nm was sufficient for preventing oxidation of Cu nanowires at 160°C for 24 h.⁵³ Thus, the thickness of Ag necessary to protect the nanowires is roughly the same for the two nanowire diameters (240 vs. 79 nm). However, when exposed to 85% RH/85°C, the sheet resistance of the Cu-Ag nanowires increased twofold after 24 h, unlike our results which showed no

change. Additionally, since the diameter of our Cu nanowires is 2.5x greater, similar shell thickness and oxidation resistance were achieved using 73% less Ag relative to Cu. This shows that if thin nanowires are not required, using a nanowire with larger diameter can reduce the amount of Ag necessary to produce oxidation-resistant Cu nanowires, thereby making them more cost-effective.

2.2 Tunable Synthesis of Low Aspect Ratio Cu Nanowires

While the previous section demonstrated that long Cu nanowires can be produced in the multigram scale, there are currently no tunable, scalable syntheses for low aspect ratio Cu nanowires. One of the biggest challenges in simplifying and increasing the scale of Cu nanowire synthesis is the heat required to form Cu nanowires. In order to reduce the complexity of Cu nanowire synthesis, we need a solution that can raise the temperature of the reaction solution uniformly and consistently, regardless of volume. Mardiansyah et al. have reported an aqueous synthesis of Cu nanowires without the need for external heating by using the heat of NaOH dilution as the source of heat.⁷⁰ However, it was not clear what length or yield of nanowires was produced, and the synthesis used hydrazine as the reducing agent, which is highly toxic and a known carcinogen.

In this work, we developed a self-heating reaction that can be easily modified to produce Cu nanowires with varying aspect ratios. Self-heating was achieved in two parts: dilution of NaOH and degradation of glucose in an alkaline solution. The dilution of

NaOH is a well-known exothermic reaction, while the degradation of glucose in alkaline solutions is more complex. Glucose is converted to enediol in the presence of a strong base and exhibits a yellow-brown color⁷⁷, and further analysis showed that fructose is also produced.⁷⁸ Moreover, Yang et al. reported that over 50 compounds are produced in the alkaline degradation of glucose.⁷⁶

By developing a self-heating synthesis, we have made it much simpler and faster to produce Cu nanowires in large quantities without utilizing an external heat source. Replacing hydrazine with glucose also enabled us to control the amount of heat produced by the reaction, as well as make the reaction safer and greener.

2.2.1 Using Glucose Degradation and NaOH Dilution to Control Reaction Kinetics

Short, thin Cu nanowires were produced at a scale of 1 L, producing up to 350 mg per batch, as shown in Figure 18a. The separate NaOH/Cu(NO₃)₂ and glucose solutions were both preheated to 50°C. Mixing the two solutions resulted in a sharp temperature increase over 4 s (Figure 18b). Figure 19 shows that 12°C of this temperature rise is attributable to the dilution of NaOH, with the remainder due to the reaction of NaOH with glucose. Yang et al. have shown the alkaline degradation of D-glucose produces over 50 compounds, some of which may also act as reducing agents in addition to glucose.⁷⁶ Following this initial fast temperature rise, the temperature continues to rise more slowly depending on the amount of glucose in the reaction solution. Essentially no additional

temperature increase occurred at a concentration of 0.2 g/mL, while the temperature increased from 72 to 110°C at a glucose concentration of 1.0 g/mL. As shown in Figure 18c, increasing the amount of glucose and the temperature of the reaction increases the yield of reduced Cu.

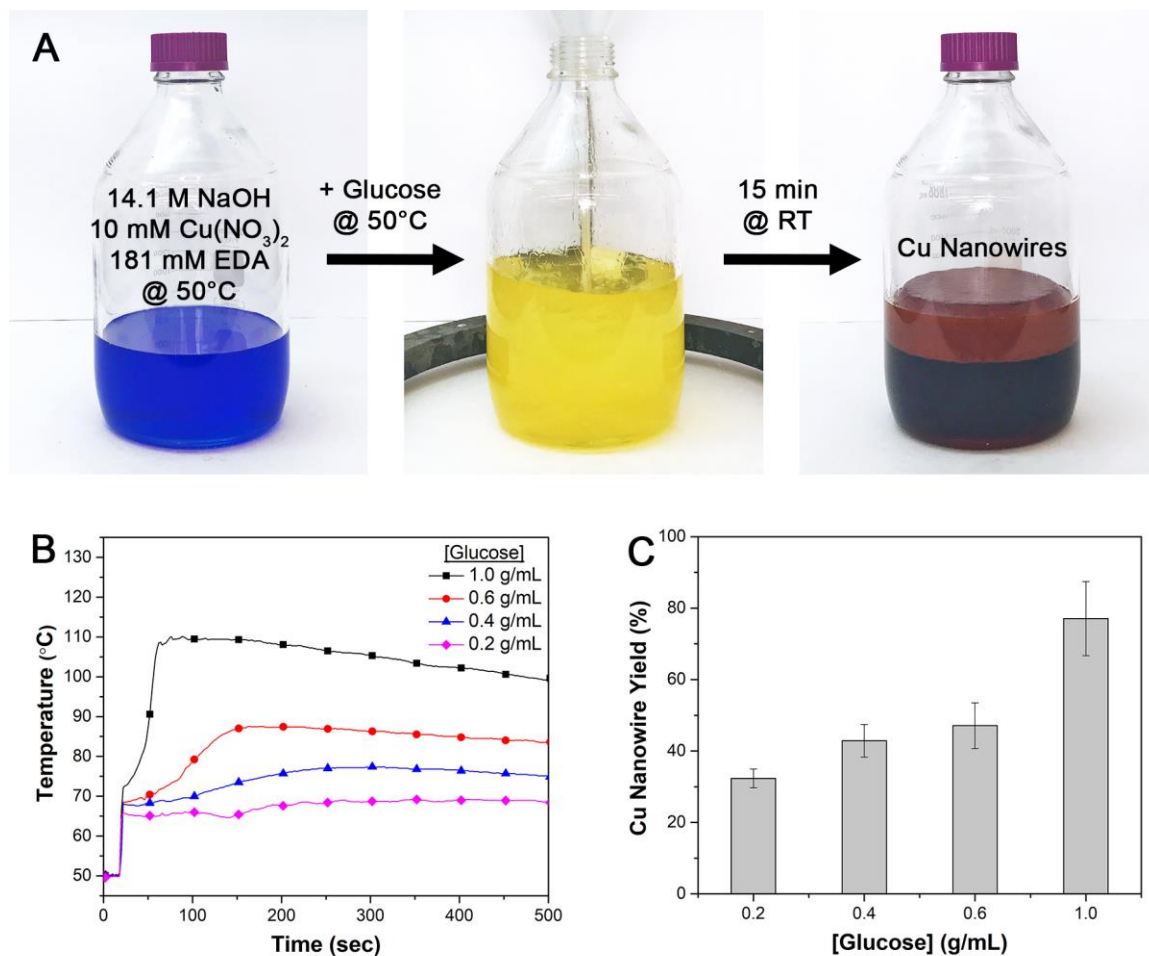


Figure 18: Tunable, self-heated synthesis of short Cu nanowires. (a) Summary of the reaction process. (b) Temperature profiles of Cu nanowire syntheses with varying initial concentrations of glucose solution. (c) The yield of Cu nanowires produces for each condition.

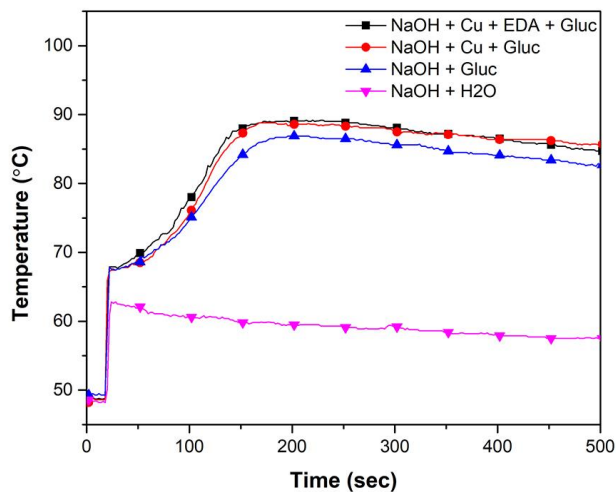


Figure 19: Temperature profile of NaOH with varying reactants.

Figure 20 shows that with the increase of the glucose concentration came the decrease of the lengths of the nanowires produced by the reaction. The fact that the length of the nanowires decreased with increasing yield of reduced Cu indicates that increasing the amount of glucose resulted in the formation of a greater number of Cu nuclei and shorter nanowires. Figure 20 also shows that the dimensions of the nanowire product are easily adjustable by changing the amount of glucose added to the reaction.

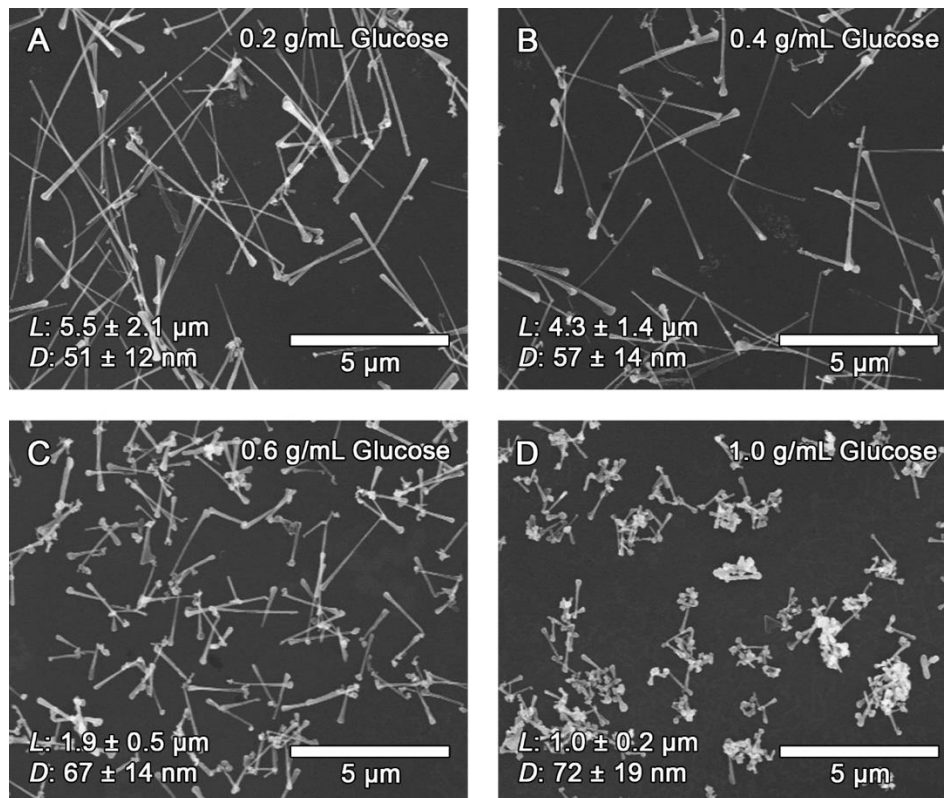


Figure 20: SEM images of the Cu nanowires with average length (L , $n = 200$) and diameter (D , $n = 100$).

This work demonstrated a Cu nanowire synthesis that can produce Cu nanowires with predictable aspect ratios by varying the amount of reducing agent. The use of glucose as the reducing agent in a NaOH-based synthesis resulted in a self-heated reaction due to the degradation of glucose in the presence of an alkaline solution, providing the heat necessary for Cu nanowire formation. Changing the concentration of glucose in the reaction resulted in an observable trend in aspect ratio, enabling us to predict the amount of glucose necessary to obtain nanowires with specific dimensions.

3. Applications for Cu Nanowires

3.1 Highly Conductive Nanowire-Based 3D Printing Filament⁴⁸

3.1.1 Introduction to 3D Printed Electronics

Printed electronics offer the potential to lower the cost of prototyping and producing electronics, as well as enabling the production of devices with unconventional geometries or mechanical properties (i.e., flexible and stretchable).⁷⁹⁻⁹⁰ To date, various printing methods using highly conductive inks have enabled high throughput production of RFID tags, smartcards, displays, packaging, antennas, and printed circuit boards.^{87, 91-99} Moreover, development of electronics with unique functionalities such as wearable, flexible, and degradable sensors is now possible due to advancements in printing technology.¹⁰⁰⁻¹⁰⁴ Within the last several years, 3D printing has been increasingly applied to the creation of printing electronics.^{80, 87, 105-107} The most common form of 3D printing used in consumer-grade printers involves creating a 3D object from a digital model through a layer-by-layer fused deposition modeling (FDM) process. 3D printed electronics offers the potential to prototype complex 3D objects with integrated electronics in a matter of hours versus weeks with printed circuit board-based prototyping and hand-assembly. Electronics with complex geometries that are either too costly or complicated for traditional fabrication techniques can be manufactured via 3D printing in order to improve functionality.^{80, 85, 108}

Several techniques currently exist for 3D printing electronics, including hybrid insertion methods, surface direct-write, and freeform multi-material 3D printing.⁷⁹⁻⁹⁰ Earlier methods typically use a combination of these techniques. For example, the complete fabrication of an electronic device could first start with 3D printing a nonconductive substrate, followed by filling in pre-fabricated channels with conductive ink, and finally inserting electrical components.^{80, 109} While this method has been successful in producing devices with unique configurations, it is often associated with high costs due to expensive inks that must be used with specialized printers. Moreover, there is still a need for a fabrication technique that can produce a complete device in one process from start to finish. Such a technique may be achieved by freeform multi-material 3D printing, in which conductive and nonconductive materials can be printed side by side and a complete, functional device can be produced without disrupting the printing process. One way to achieve this is by using multi-material FDM 3D printers, which can extrude conductive and nonconductive thermoplastics to produce 3D electronics in a layer-by-layer process.¹⁰⁷

Due to the surge in interest in 3D printing, consumer-grade and DIY table-top 3D printers have become increasingly sophisticated while decreasing in price.¹¹⁰ Specialized conductive filaments have also been developed in a push toward printed electronics. Table 4 provides a list of various commercially available and laboratory-scale conductive 3D printing filaments, their fillers, and their resistivity. Most of these conductive filaments

are thermoplastics containing carbon-based materials, such as carbon black and graphene.¹¹¹⁻¹¹³ The resistivity of these filaments ranges from 0.21 to 120 Ω cm, which means a 10-cm-long piece of filament has a resistance ranging from 1000 to 500,000 Ω . In comparison, the resistance of the same piece of Cu would be 7×10^{-5} Ω . A lower resistivity (0.0026 Ω cm) has been achieved by annealing graphene nanoplatelets at 1200°C,¹¹⁴ but such high-temperature annealing is impractical. Electrifi, a commercially available Cu-based filament, has a resistivity of 0.006 Ω cm and is compatible with even the most basic desktop printers.¹¹⁵ While Electrifi is by far the most conductive filament that requires no post-processing techniques, there is still room for improvement. For comparison, the resistivity of bulk Cu is 1.68×10^{-6} Ω cm.

Table 4: The Resistivity of Various Conductive 3D Printing Filaments and their Fillers.

		Conductive Filler	Resistivity (Ω cm)	Citation
Laboratory Scale	Carbomorph	Carbon black	9–120	112
	Conductive ABS Filament	Carbon black	3.6	111
	Conductive PLA Filament	Reduced graphene oxide	0.21	113
	Conductive GNP Ink	Graphene nanoplatelets	0.0026 <i>after annealing @ 1200°C</i>	114
	This work	Cu-Ag nanowires	0.002	48
Commercialized	Proto-Pasta	Carbon black	30	116
	BlackMagic	Graphene	0.6	117
	Electrifi	Cu	0.006	118

We hypothesize metal nanowires with high aspect ratios could enable the production of highly conductive 3D printable polymer composites. Monte Carlo studies have previously shown that for cylinders with radius R and length L , the critical volume fraction ϕ_c necessary for percolation is equal to R/L as $R/L \rightarrow 0$.¹¹⁹⁻¹²³ This estimate becomes fairly accurate (error $\cong 2.5\%$) at $L/R = 100$, and the error decreases linearly with increasing L/R . The effect of aspect ratio on conductivity has been demonstrated in numerous experimental systems.¹²³⁻¹²⁶ For example, Park et al. recently reported a thixotropic ink using Ag nanowires with $L/R = 133\text{--}200$, and reported an experimental $\phi_c = 0.007$, fairly close to what would be predicted based on their aspect ratio.¹²⁵ Thus, metal nanowires can enable the creation of highly conductive inks at low volume fractions. The low volume fraction of solid filler can, in turn, make it easier to ensure such conductive inks are 3D printable.

However, even though nanowires can be used at low volume fractions, the creation of even a small batch of 3D printing filament for FDM printers requires tens of grams of nanowires, making the use Ag nanowires prohibitively expensive. Cu nanowires are a logical alternative, but there was previously no relatively green, multigram-scale synthesis for Cu nanowires.^{39-40, 46} With our development of a multigram-scale synthesis for Cu-Ag nanowires, the production of a nanowire-based 3D printing filament has become much more practical. The Cu-Ag nanowires discussed in Section 2.1 were incorporated into polycaprolactone (PCL) which, due to its low melting point (59–64°C),

allows the filament to be extruded at low temperatures and thereby minimizes oxidation during printing.¹²⁷ Loading of 12 vol% Cu-Ag nanowires produced the most conductive filament that could also be extruded without brittle fracture. The resulting conductive filament had a resistivity of 0.002 Ω cm, which is the lowest resistivity reported for a 3D printing filament to date. Moreover, current capacities of up to 4.74×10^5 A/m² could be achieved depending on the surface-to-volume ratio of the printed trace.

3.1.2 Effect of Filler Morphology and Concentration on the Resistivity of the Filament

Based on previous studies of the effect of aspect ratio on the conductivity of nanowire networks,^{123-124, 126, 128} we expect that metal nanowires with higher aspect ratios would result in a more conductive filament at a lower volume percent of filler. As the percolation threshold of a conductive network decreases, the number of junctions in the network also decreases, reducing the effect of contact resistance from the junction of two nanowires. To test this hypothesis, we created nanowire-PCL composites with 3–25 vol% loading of 30 and 50- μ m-long Cu-Ag nanowires, 3–22 vol% 10 μ m Ag flakes, and 3–22 vol% of 20- μ m-long Ag nanowires. Table 5 lists the dimensions of these fillers.

Table 5: Dimensions of Ag and Cu Fillers.

	Length (μm)	Width/ Thickness (nm)	Aspect Ratio
Ag Flakes	10	310	32
Ag nanowires	20	90	220
Cu-Ag nanowires	30	250	120
	50	220	230

Figure 21 shows the resistivity of the samples initially declined with increasing filler fraction, but the resistivity of the nanowire composites remained nearly constant once a certain volume percent was reached. No further improvements in conductivity were observed beyond 11 vol% for Ag nanowires, 9 vol% for 30 μm Cu-Ag nanowires, and 6 vol% 50 μm Cu-Ag nanowires.

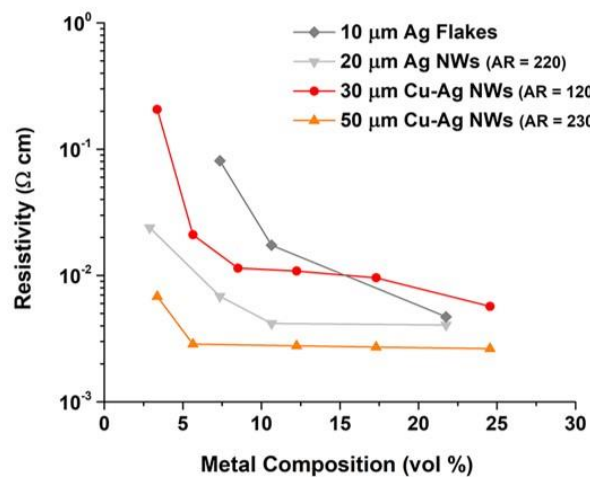


Figure 21: Resistivity of filament composites containing various Ag and Cu fillers at different volume percent (vol%).

It was expected that the resistivity of the nanowire composites would continue to decrease with increasing volume fraction, but this did not occur. We hypothesized that this may be due to an uneven dispersion of nanowires in the composite at a larger (\approx mm) length scale than could be easily probed with scanning electron microscopy (SEM). Indeed, pictures of the composite films Figure 22a) exhibit a surface roughness that increases with nanowire concentration, suggesting some degree of aggregation may be occurring.

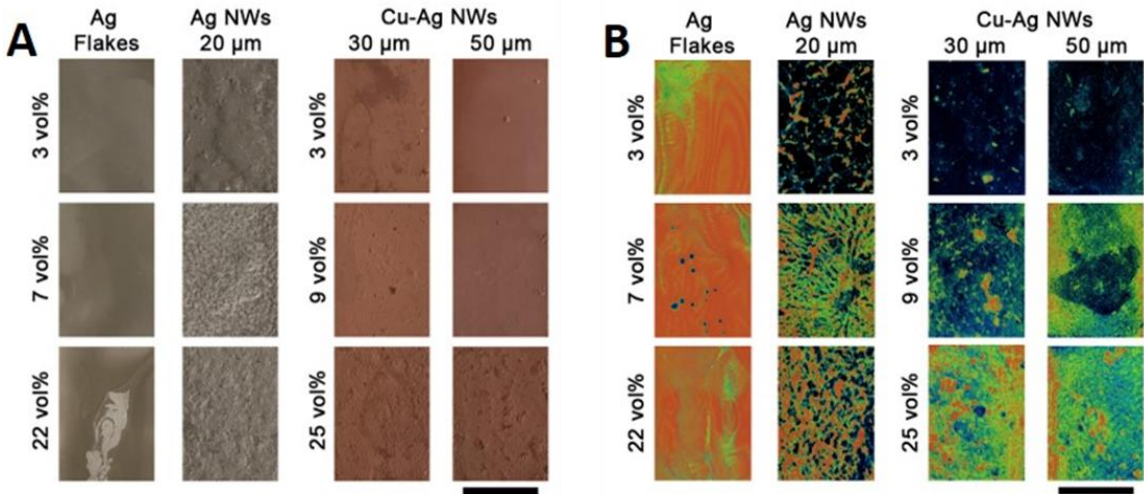


Figure 22: Determination of composite quality and filler dispersion. (a) Camera images of the composite films show the greater surface roughness of nanowire composites with high loadings of nanowires. (b) Micro-CT images of filament composite films showing areas of high (red) and low (blue/black) density of metal filler. The scale bars for both (a) and (b) are 1 cm.

To explore this phenomenon further, we performed high-resolution X-ray computed tomography (micro-CT, Nikon XTH 225 ST) on the composites. The resulting images (Figure 22b) show areas of high (red) and low (blue/black) densities of nanowires in the composite films. Aggregation is most notable in the Ag nanowire composite, which shows a few aggregates at 3 vol%, but more of a network of aggregates at 7 and 22 vol%. Cu-Ag nanowire composites similarly displayed an increased fraction of high densities of nanowires segregates into regions of the film instead of dispersed throughout the film. The aggregation in the nanowire composites makes it difficult to come to any conclusions with respect to the quantitative effects of length and aspect ratio on the conductivity in this experimental system. In contrast, the flake morphology exhibited fairly even contrast across the film, indicating a minimal amount of aggregation. At the same time, the resistivity of the Ag flake composites continually decreased.

This combination of resistivity and micro-CT data suggests that the nanowires become more easily aggregated than the flakes in the PCL composite, resulting in different resistivities as a function of volume fraction. This is likely due to the higher percolation threshold of the flakes relative to the nanowires. At volume fractions greater than ϕ_c , the excluded volumes of the nanowires will interpenetrate, leading to the formation of a large number of contacts between nanowires and thus the formation of aggregates. In addition, one can intuitively expect flakes to flow across one another while nanowires may get more easily tangled.¹²⁹⁻¹³⁰ However, the resistivity of the 50- μm -long Cu-Ag nanowire

composite at 5 vol% was lower than all other samples, including the composite with 22 vol% of Ag flake. Thus, if Cu-Ag nanowires can be as much as five times cheaper and achieve a lower resistivity. Table 2Table 3 (Appendix 1) suggest that such a cost target may be within reach with further scale-up and optimization of the synthesis.

Table 2: Labor and Materials Cost of Cu Nanowire Production at Low and High Volume

3.1.3 Production of 3D Printing Filament

A conductive filament was produced by adding 12 vol% 45- μm -long Cu-Ag nanowires to PCL dissolved in dichloromethane (DCM) (Figure 23a). The DCM was evaporated off completely to form a solid composite. This composite was cut into pellets (Figure 23b) and extruded into filament using a Filabot filament extruder (Figure 23c,d). An SEM image shown in Figure 23e suggests that the Cu-Ag nanowires were evenly distributed throughout the filament at this volume fraction and length scale.

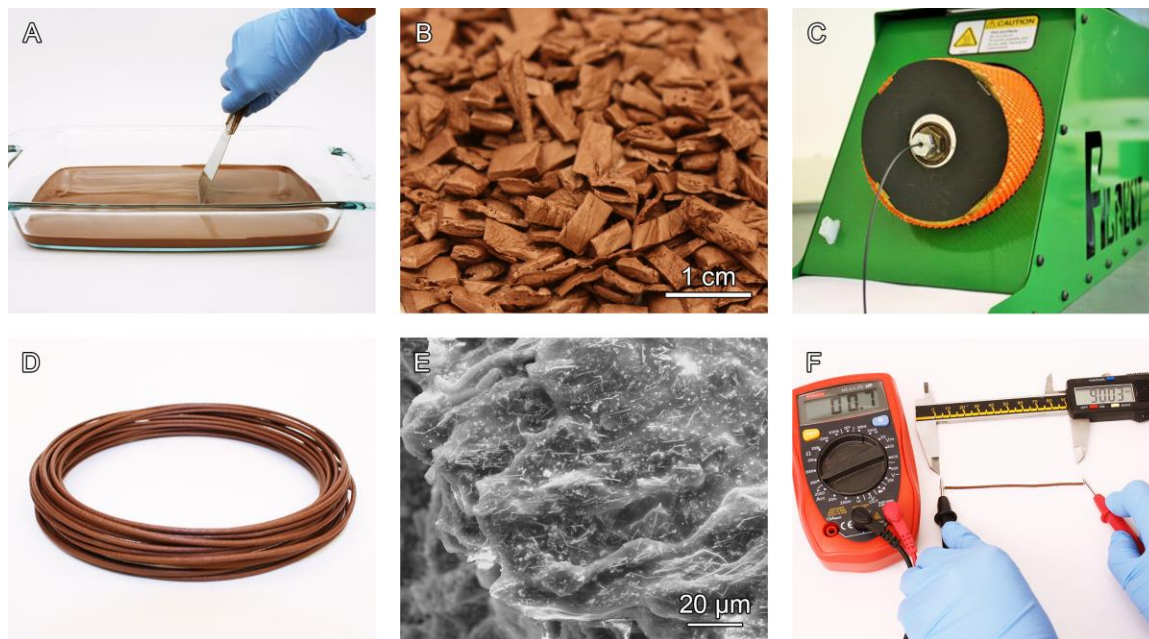


Figure 23: Production of nanowire-based 3D printing filament. (a) Filament production started with a mixture of Cu-Ag nanowires and PCL dissolved in DCM. (b) Drying of this solution created a solidified composite which was cut into uniform pellets, and (c) extruded through a Filabot to form the filament. (d) The Filabot produced a coil of conductive filament similar in dimensions to other commercially available filaments used for 3D printing (diameter = 1.75 mm). (e) SEM image shows the dispersion of Cu-Ag nanowires in the PCL filament. (f) a 90 mm length of filament with a diameter of 1.8 mm had a measured resistance of 0.7 Ω .

Although the previously discussed conductivity results suggest that the ideal composite would be composed of ≈ 5 vol% 50 μm Cu-Ag nanowires, increasing the scale of the Cu nanowire synthesis resulted in a slight decrease in length from 50 to 45 μm . Moreover, extruded filaments with 5 vol% Cu-Ag nanowires resulted in a printable, but nonconductive, filament. The loss of conductivity after extrusion was likely caused by the breakage of wires during the extrusion step. Measurements from dark-field optical

microscopy (DFOM) images of the Cu-Ag nanowires in the composite before and after extrusion show the average length decreased from $45 \pm 15 \mu\text{m}$ to $10 \pm 8 \mu\text{m}$ (Figure 24).

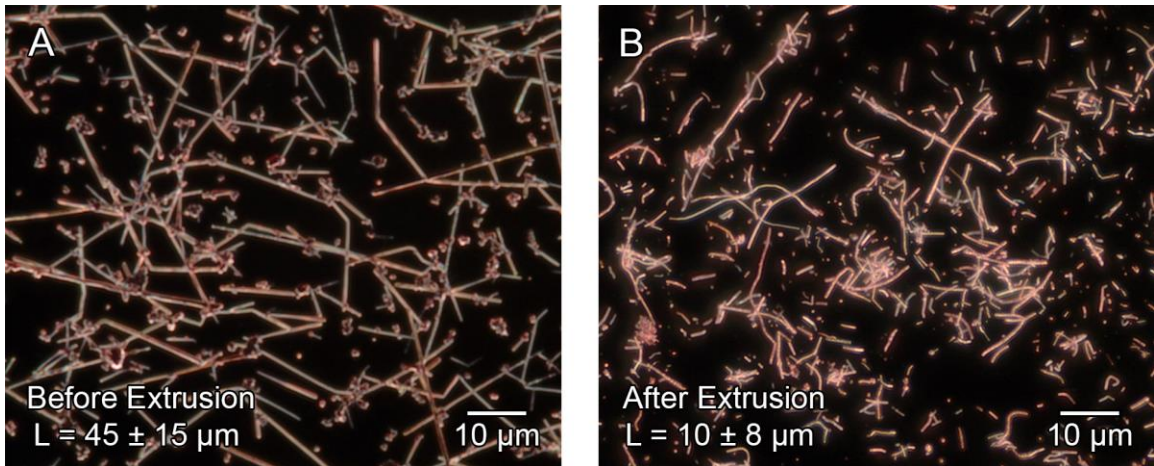


Figure 24: DFOM images comparing the lengths of Cu-Ag nanowires in composite (a) before and (b) after extruding into filament.

To overcome this issue, the loading of Cu-Ag nanowires was increased to 12 vol%, which was the maximum loading found to be conductive without making the filament so brittle that it could not be continuously extruded. The Ag coating was also increased to 0.10 Ag:Cu mol ratio to minimize oxidation during the elevated temperatures used during filament extrusion and printing.

The 12 vol% filament was found to be printable with a 1.0 mm nozzle at a 0.2 mm layer thickness. Printing attempts with 0.2- and 0.5-mm nozzles resulted in clogging, which is a common problem for other commercially available conductive filaments at

these small nozzle diameters. Therefore, the minimum diameter and thickness of printed features with this filament are 1.0 mm and 0.2 mm, respectively.

3.1.4 Resistivity of Cu-Ag Nanowire Filament

The resistivity of the conductive PCL filament was $0.002 \text{ } \Omega \text{ cm}$ prior to printing (Figure 23f). This is a >100 times improvement from previously reported conductive filaments containing various carbon-based fillers such as carbon black ($9\text{--}120^{112}$ and $3.61^{111} \text{ } \Omega \text{ cm}$) and reduced graphene oxide ($0.21 \text{ } \Omega \text{ cm}^{113}$) (see Table 4). The Cu-Ag nanowire filament is also comparable to the most conductive filament reported in literature, which contains graphene and has a resistivity of $0.003 \text{ } \Omega \text{ cm}^{114}$. However, the process required to reach such a low resistivity involved heating the printed object at 475°C for 1 h to burn off the specialized polyethylene glycol ink, followed by an annealing step at 1200°C for 5 min. Because our Cu-Ag nanowire filament does not require any post-processing steps to achieve similar conductivity, this new filament represents a significant improvement in practicality and accessibility.

3.1.5 3D-Printed Inductive Charging Coil as a Proof of Concept

To determine the printability of the nanowire-based filament using a standard tabletop 3D printer, as well as demonstrate its conductivity, Figure 25a shows a 3D-printed inductive charging coil powering an LED using a wireless charging dock. The 3D

printed coil was designed with a winding width of 2 mm and a diameter of 24 mm in order to fit within the footprint of the charging coil, giving a coil with seven turns. The inductance of this coil can be approximated with the Wheeler formula:

$$L = \frac{r^2 n^2}{8r + 11w}$$

where L is the inductance (μH), r is the average radius of the spiral (inches), n is the number of turns, and w is the width of the winding (inches).¹³¹ From this formula, we calculated that the inductance of the printed coil was $4.8 \mu\text{H}$, which is about half the inductance of the charging coil ($8.7 \mu\text{H}$). The waveforms (Figure 25b) from the charging (transmitting) and printed (receiving) coils show 40% of the input voltage was transferred to the printed coil, which is in line with what one would expect from their difference in inductance.

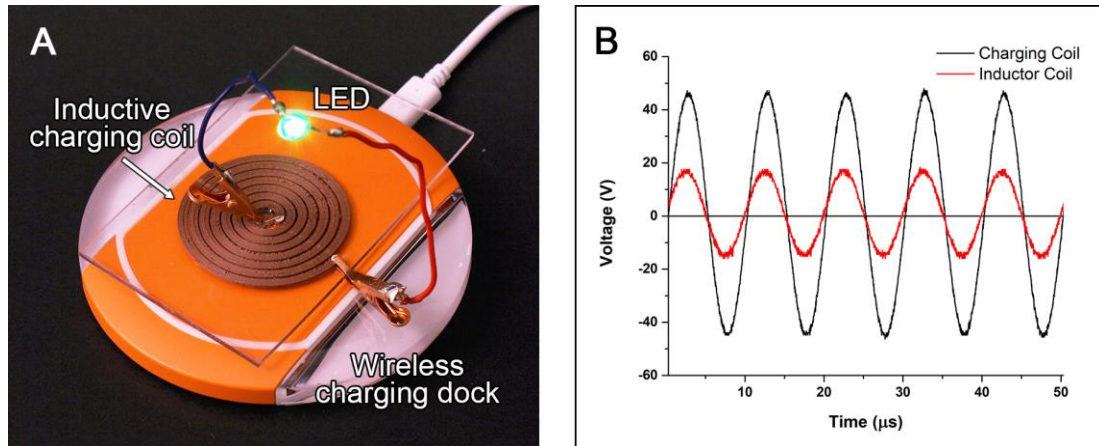


Figure 25: Proof of concept 3D printed inductive charging coil. (a) Demonstration showing how the Cu-Ag nanowire filament can be used to 3D print an inductive charging

coil to wirelessly power an LED. (b) Oscilloscope measurement of the transmitted (charging coil) and received (inductor coil) waveforms.

3.1.6 Temperature Resistance and Current Capacity

Since the nanowire-based filament was developed to conduct electricity, we investigated the thermal resistance of the filament, as well as determined the maximum current capacity that a printed trace can withstand. Figure 26 shows the stability of 12 vol% Cu-Ag nanowire filament exposed to increasing temperatures in a dry oven. The resistivity of the filament was stable up to 110°C, after which the resistivity sharply increased. At 145°C the filament was not conductive due to the low melting point of PCL (60°C),¹²⁷ the resistivity of the filament was stable well beyond that point. Moreover, the areas of the conductive filament that were not in contact with the multimeter leads retained their shape throughout the duration of the experiment. These observations suggest that the Cu-Ag nanowire filament has higher thermal stability than pure PCL. It is possible that the addition of Cu-Ag nanowires provided structural support to the PCL by increasing the viscosity of the melt. Therefore, the PCL was able to retain its shape, and the connections between the Cu-Ag nanowires were maintained beyond the exact melting point.

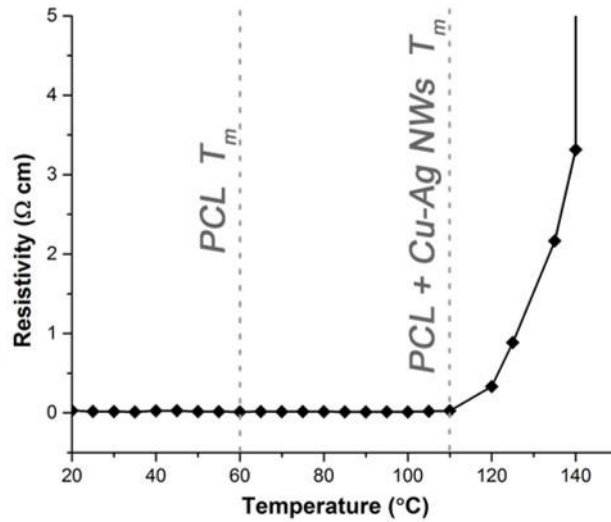


Figure 26: Resistivity of the conductive filament vs. temperature. The melting points of pure PCL and PCL with Cu-Ag nanowires are indicated by dashed lines.

The maximum current capacity of the 3D printed traces was determined by plotting the current density at failure for printed traces with varying surface-area-to-volume ratios, as shown in Figure 27a. The current was increased stepwise in 1 mA increments every 5 s. Failure was defined as the current at which the resistance of the trace doubled due to Joule heating, which caused the PCL to melt and the Cu-Ag nanowires to oxidize.

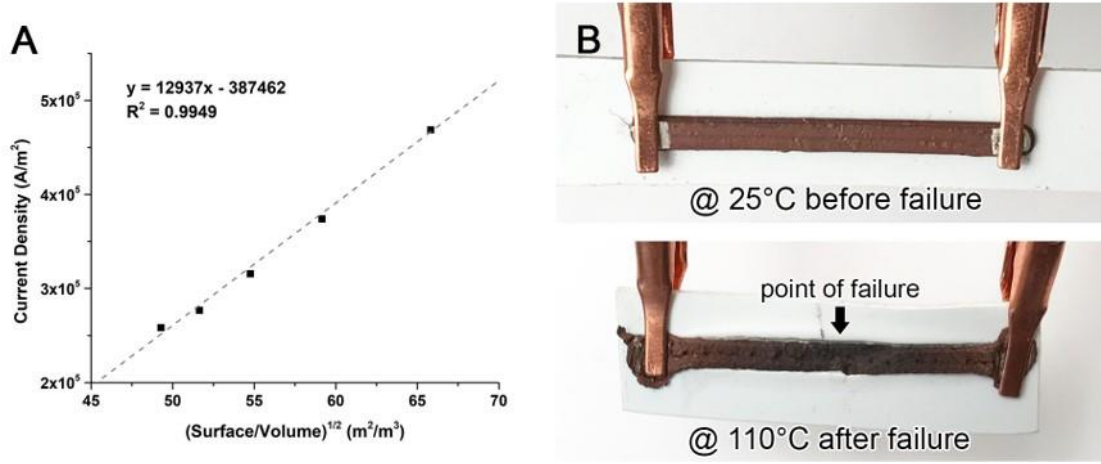


Figure 27: Thermal limitations of nanowire-based filament. (a) Current density at failure with the square root of the surface-to-volume ratio of the 3D printed traces. (b) 3D printed traces before (top) and after (bottom) failure due to Joule heating.

To estimate the current density at failure for the printed traces, we assume homogenous Joule heating, heat conduction along the printed traces, and heat conduction from the printed traces to the surrounding air via convection. The temperature distribution $T(x)$ in the printed trace is given by Equation 1.

$$T(x) - T_{\infty} = \frac{j^2 \rho V}{A_{SA} h} \left[1 - \frac{\cosh\left(x \sqrt{\frac{A_{SA} h}{V K}}\right)}{\cosh\left(\frac{L}{2} \sqrt{\frac{A_{SA} h}{V K}}\right)} \right] \quad (\text{Eq. 1})$$

where $T(x)$ is the temperature of the printed trace at x , T_{∞} is the temperature of the air in the room, j is the current density, ρ is the resistivity of the printed trace, K is the thermal conductivity of the printed trace, L is the length of the printed trace, x is the position along the length of the trace ($-L/2 \leq x \leq L/2$ and $x = 0$ at the middle of the printed trace), h is the

heat transfer coefficient, A_{SA} is the surface area of the trace, and V is the volume of the printed trace.¹³² Based on this equation, the highest temperature occurs in the middle of the printed trace. This is indeed what occurred when we applied a current to the printed traces which was increased stepwise in 1mA increments every 5 s (see Figure 27b). Thus, in order to predict the current density at failure, it is only necessary to determine the change in temperature that occurs in the middle of the trace where $x = 0$. Equation 1 can then be simplified to:

$$T(0) - T_{\infty} = \frac{j^2 \rho V}{A_{SA} h} \left[1 - \frac{1}{\cosh\left(\frac{L}{2} \sqrt{\frac{A_{SA}}{V} \times \frac{h}{K}}\right)} \right] \quad (\text{Eq. 2})$$

Equation 2 can be simplified further since the term $\frac{L}{2} \sqrt{\frac{A_{SA}}{V} \times \frac{h}{K}} \gg 1$. For our experimental conditions, the values of A_{SA}/V are in the range of 2400–4300 m^{-1} and the length of the traces are 0.025 m. A typical heat transfer coefficient (h) for air with natural convection is 200 $\text{W}/\text{m}^2\text{K}$, and the thermal conductivity (K) of metal nanowire-polymer composite is below 2 $\text{W}/\text{m}^2\text{K}$.¹³²⁻¹³⁴ Thus, the bracketed term is ≈ 1 (i.e., 0.996–0.999) and Equation 3 can be simplified to:

$$T(0) - T_{\infty} = \frac{j^2 \rho V}{A_{SA} h} \quad (\text{Eq. 3})$$

By simply rearranging Equation 3, the current density of the printed trace at failure (j_{failure}) due to Joule heating can be expressed as:

$$j_{failure} = \sqrt{\frac{h\Delta T_{at failure}}{\rho}} \cdot \sqrt{\frac{ASA}{V}} \quad (\text{Eq. 4})$$

Equation 4 shows a linear relationship between the current density at failure and the square root of the surface-area-to-volume ratio, where the slope is dependent on the heat transfer coefficient, the difference in the temperature of the printed trace, the air in the room ($\Delta T_{at failure}$), and the electrical resistivity of the trace.

Figure 27a shows that a plot of $j_{failure}$ versus $\sqrt{\frac{ASA}{V}}$ is linear, as expected from Equation 4. The validity of the experimental data was further verified by setting $\Delta T_{at failure} = 85$ K based on the difference between the temperature of the filament and room temperature, and $\rho = 0.00004 \Omega \text{ m}$ based on the average resistivity of the printed traces. With these variables known, the convective heat transfer coefficient could be determined from the slope of the experimental linear fit. The calculations resulting from the experimental data indicate the heat transfer coefficient was $79 \text{ W/m}^2\text{K}$. Previous work on heat transfer in an additively manufactured polymer heat exchanger reported a heat transfer coefficient range of $35\text{--}120 \text{ W/m}^2\text{K}$,¹³⁵ in line with that of the experimental data. Such a predictable trend is helpful in engineering the geometry of 3D printed objects based on the current that will be applied. Not surprisingly, a printed trace with a higher surface-area-to-volume ratio, a lower resistivity, and a higher melting point polymer will withstand a higher current density.

3.1.7 Conclusion

Cu-Ag nanowires were used to create a 3D-printing filament >100 times more conductive than commercially available graphene-based filaments. Printed traces were stable up to 110°C, limited by the low melting point of the PCL filament (60°C), and could support current densities between 2.5 and 4.5 × 10⁵ A/m² depending on the surface-to-volume ratio of the printed trace. A 3D-printed inductive charging coil provided a simple demonstration of the potential applications of the highly conductive Cu-Ag nanowire filament. It appears the aggregation of the nanowires in the filament limited the maximum conductivity that could be achieved. Thus, future work on nanowire composites might further explore the effect of nanostructure morphology and surface treatment on aggregation and the rheology of the polymer melt during processing to achieve higher loadings of nanostructures.

3.2 Stretchable Conductor

This section discusses how the development of a multigram-scale synthesis for long aspect ratio Cu-Ag nanowires (Section 2.1) enabled the development of a stretchable conductor that could maintain its conductivity at up to 300% strain in a project led by Matthew Catenacci.⁶⁹ The goal of this work was to develop a material that is both conductive and stretchable for applications such as wearable electronics, robotics,

bioelectronics, and energy storage,¹³⁶⁻¹⁴¹ where the material must have a conductivity similar to Cu wiring while also undergoing many cycles of stretching.

Among the previous works in stretchable conductors, elastomers doped with Ag microflakes stand out as most promising due to their high conductivity both initially and after 50 cycles of 50% strain.¹⁴²⁻¹⁴⁴ However, the best results were achieved only after the Ag microflakes were sintered via photonic curing, whereas those that were not sintered exhibited more significant increases in resistance after strain, leading one to conclude that the structure of the microflakes do not lend to secure electrical interconnections when the elastomer is stretched. Additionally problematic is the monetary and environmental cost of Ag, which is an expensive metal with a large carbon footprint. For these reasons, a more effective and practical alternative is necessary for the advancement of stretchable circuitry.

One possible alternative is a Cu nanowire-based stretchable composite, which have been shown to be very conductive at low volume fractions due to their high aspect ratio.^{48, 145} The nanowires can achieve high conductivity within a composite due to their tendency to tangle and form a greater number of electrical interconnections. Moreover, Cu is 1000 times more abundant, 100 times less expensive, and has a carbon footprint 25 times lower than Ag.³⁴ Thus, using the developed Cu-Ag nanowires discussed in Section 2.1 (which are coated with a minimally thin Ag shell to prevent oxidation) presents a solution that is more cost-effective, potentially has the ability to maintain its conductivity

under strain, and is also practical since our lab has the capability of producing large quantities of those nanowires.

A stretchable Cu-Ag nanowire composite was made by first producing a nanowire felt via vacuum filtration. As shown in Figure 28a, nanowires suspended in an aqueous solution were filtered through a silicone gasket laser-cut with the shape of the desired final structure. The nanowire felt was then annealed at 150°C to improve conductivity (1.6 times higher than the air-dried felt) before finally infiltrating it with PDMS (Figure 28b-c). The resulting flexible nanowire composite had a porosity of 90% and a conductivity of 1220 ± 630 S/cm.

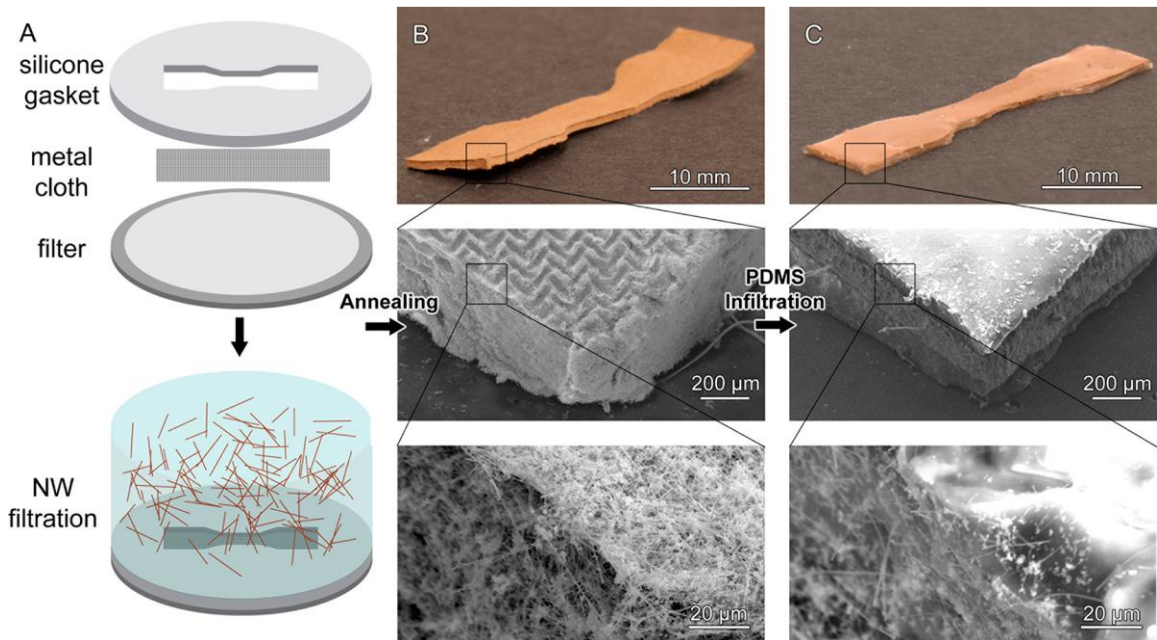


Figure 28: Production of a stretchable conductor using Cu-Ag nanowires. (a) Cu-Ag nanowires were filtered through a silicone gasket onto a metal cloth to create a nanowire

felt in the shape of the hole in the gasket. (b) Photograph and SEM image of felt after annealing and (c) after PDMS infiltration.⁶⁹

Additional optimizations were conducted to determine how the type and composition of PDMS (which affected factors such as stiffness and void formation) influenced the conductivity of the composite under cycles of strain. For example, Figure 29 shows that Cu-Ag nanowires infiltrated with Ecoflex consistently displayed lower changes in resistance under cycles of strain compared to Dragon Skin. However, more detailed reports of these efforts are outside the scope of this dissertation.

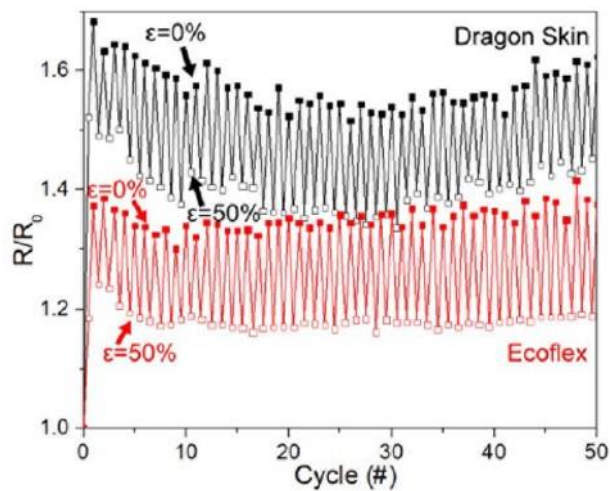


Figure 29: R/R_0 behavior over 50 cycles at 50% strain.⁶⁹

Ultimately, a stretchable elastomer was developed which had a conductivity comparable to previous composites made with Ag microflakes (1270 S/cm), but had the

best retention in conductivity after 50 cycles of stretching to 50% strain (only 37% increase in resistance) compared to any material with a conductivity higher than >1000 S/cm. Moreover, the fabrication method used in this study also enabled the formation of a serpentine pattern that was able to retain its conductivity up to strains of 300%, as shown in Figure 30.

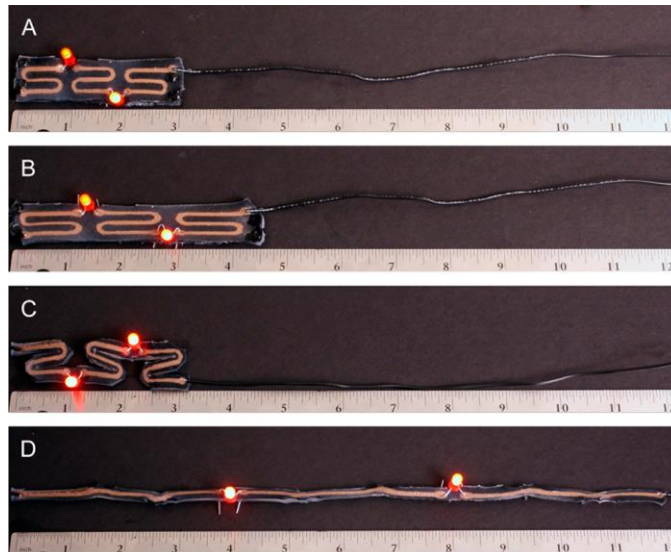


Figure 30: Demonstration of conductor stretchability. (a) A stretchable LED circuit at 0% and (b) 50% strain. Serpentine variant of stretchable LED circuit at (c) 0% and (d) 300% strain.⁶⁹

3.3 Flow-Through Electrode

Similar to the stretchable conductor, the development of a flow-through electrode in a project led by Myung Jun Kim was also enabled by the multigram-scale synthesis of Cu nanowires (Section 2.1). In both the 3D printing filament and stretchable conductor,

the key to the success of the applications was the long length of the Cu nanowires. However, the relatively thin diameter of the nanowires can also be beneficial, especially in applications that require maximum surface area, such as in flow-through electrodes. In this work, Kim et al. demonstrated how reducing the size of the fibers in a flow-through electrode to the nanoscale can increase the productivity of electrochemical processes.⁶⁸

Organic electrochemistry has been proposed as a viable option to utilize surplus energy generated by renewable resources. One of the challenges of renewable energy is using and distributing it efficiently, and current infrastructures do not yet allow us to fully utilize all the energy that is available. This results in curtailment, where power generators are deliberately cut in order to meet the demand, or lack thereof, for renewable energy. Thus, directing some of the curtailed energy toward electrochemical synthesis allows us to use resources that would otherwise have been wasted, and also presents a potentially cheaper and more environmentally friendly alternative to traditional synthetic methods.

One of the more pressing challenges to utilizing electricity for chemical production is that the production rate of product per unit volume increases with the surface area of the electrode rather than the volume of the reactor. As a result, industrial electrochemical reactors tend to be much larger and more expensive than heterogenous gas-phase or homogenous chemical reactors for a given rate of chemical production.¹⁴⁶ Moreover, at the relatively high voltages and currents used to drive an electrochemical process at its maximum rate, the reaction is usually under mass-transport-limited conditions (the

reaction rate is limited by how quickly the reactants reach the electrode and how quickly the product can move away). Thus, to maximize productivity, one must increase the surface area of the electrode while also increasing the rate at which reactants and products move to and from the electrode surface.

To this end, a flow-through electrode using Cu nanowire felt was developed, which had a 15x greater surface area compared to conventional carbon-based electrodes with the same dimensions. Figure 31 illustrates how significantly thinner and more compact the Cu nanowires (diameter: 220 nm) were compared to carbon paper (10 μm , industry standard). The more finely divided nature of the Cu nanowire felt relative to carbon paper resulted in an increase in the mass transport coefficient (i.e., diffusion rate coefficient that relates the mass transfer rate, mass transfer area, and driving force concentration difference) by up to 3.6 times at the highest flow rate.

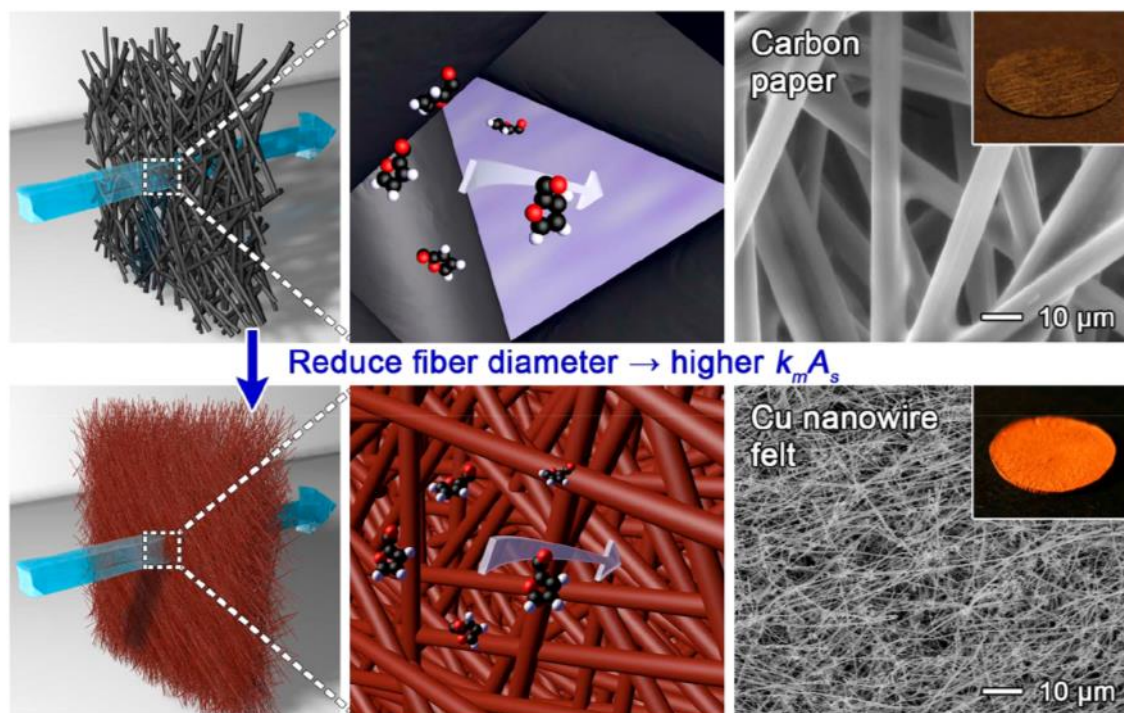


Figure 31: Schematic illustration of this study's effort to explore how reducing the size of the fibers in a flow-through electrode to the nanoscale can improve productivity. SEM images show the different diameters of the fibers in the Cu nanowire felt and carbon paper. Insets are photographs of the Cu nanowire felt and carbon paper.⁶⁸

The Cu nanowire felt was also utilized for an intramolecular cyclization of 2,2'-bis(bromomethyl)-1,1'-biphenyl to produce 9,10-dihydrophenanthrene (see Figure 32a) in order to test the suitability of the Cu nanowire felt for electroorganic syntheses. Figure 32b shows that the Cu nanowire felt electrode displayed significantly higher single-pass conversions (defined as the concentration of reactant depleted as it passed through the reaction cell divided by the initial reactant concentration) than carbon paper at all tested flow rates and initial concentrations of the reactant. Moreover, Figure 32c shows the

maximum productivity achieved with the Cu nanowire felt electrode (0.54 g/h) was 4.2x higher than that of carbon paper (0.126 g/h).

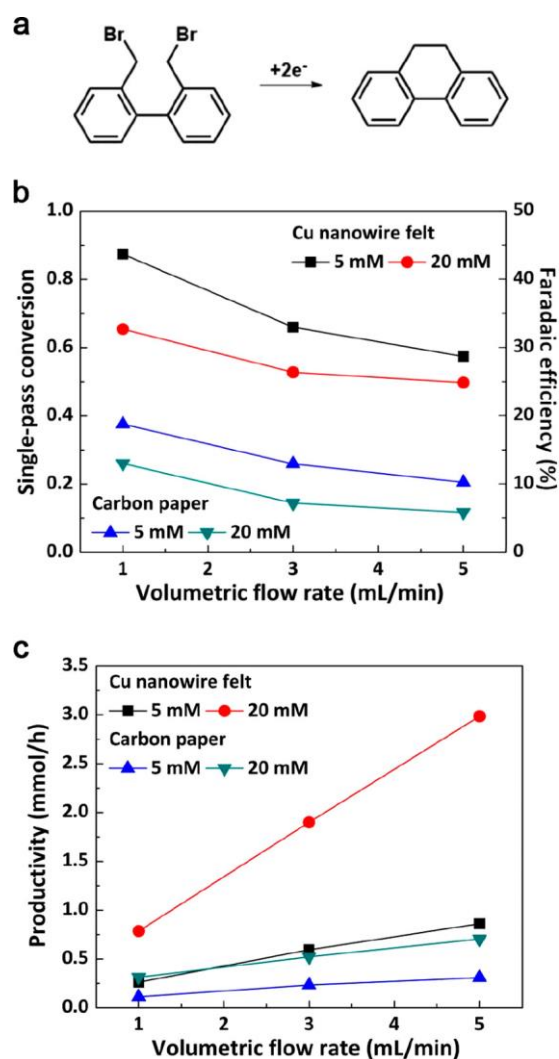


Figure 32: Performance of nanowire-based flow-through electrode. (a) Schematic for the conversion of 2,2'-bis(bromomethyl)-1,1'-biphenyl to 9,10-dihydrophenanthrene. (b) Single-pass conversion, Faradaic efficiency, and (c) corresponding productivity of 9,10-dihydrophenanthrene as a function of volumetric flow rate and concentration of 2,2'-bis(bromomethyl)-1,1'-biphenyl for Cu nanowire felt and carbon paper.⁶⁸

Table 6 summarizes the physical properties of the Cu nanowire felt in comparison to commercially available flow-through electrodes. Although the Cu nanowire felt had the lowest permeability, the thin diameter of the nanowires compared to the fibers in carbon- and Ni-based electrodes resulted in a significantly higher specific surface area at comparable porosity. The unique structure-property relationship of highly conductive the Cu nanowire felt makes it a promising material for improving the efficiency and productivity of flow electrochemical systems.

Table 6: Physical Properties of Carbon Paper, Graphite Felt, Reticulated Vitreous Carbon, Ni Foam, and Cu Nanowire Felt.⁶⁸

	Carbon Paper	Graphite Felt	Reticulated Vitreous Carbon	Ni Foam	Cu Nanowire Felt (this study)
Resistivity ($\mu\Omega$ cm)	$4.7\text{--}5.8 \times 10^3$	3×10^5	$2.3\text{--}6.9 \times 10^5$	1×10^3	143 (± 8)
Specific Surface Area (cm^2/cm^3)	1.6×10^3	2.3×10^2	$1.34\text{--}6.75 \times 10^1$	$1.9\text{--}4.1 \times 10^2$	2.4×10^4 ($\pm 1.2 \times 10^3$)
Porosity (%)	78–80	98	90–97	97–98	94 (± 0.7)
Permeability (m^2)	10^{-12}	$10^{-10}\text{--}10^{-11}$	$10^{-9}\text{--}10^{-10}$	$1.8 \times 10^{-8}\text{--}$ 2.6×10^{-9}	9.92×10^{-14} ($\pm 4.5 \times 10^{-15}$)

4. Single-Crystal Electrochemistry to Understand the Role of I⁻ in Cu Nanoplate Growth

Although Cu nanocrystals have been used in applications such as nanowires in transparent electronics¹⁴⁷ and nanoparticles for catalysis and organic reactions,¹⁴⁸ the effects of halide ions on Cu nanocrystal growth have not been clearly demonstrated. The most commonly used shape-directing agents used in Cu nanocrystal syntheses are alkylamines, which induce the formation of pentagonally-twinned nanowires and nanocubes.^{41, 44} For both structures, preferential adsorption of alkylamine on {100} facets over {111} has been the pervasive explanation for growth. However, using Cu single-crystal electrodes, we recently discovered that Cu nanowire growth is the result of competitive adsorption between Cl⁻ and alkylamines.⁴⁷ The adsorption of alkylamines alone is not facet preferential; rather, Cl⁻ selectively disrupts the self-assembled monolayer (SAM) of alkylamines on {111} facets. This disruption facilitates Cu atomic addition to {111} facets and ultimately yields anisotropic nanowires. This work suggests that the role of the Cl⁻ halide is far more significant than previously suspected and warrants further investigation. It also implies that other halides such as Br⁻ and I⁻ can potentially alter the growth mode of Cu nanocrystals since while Cl⁻ facilitates Cu deposition,¹⁴⁹ Br⁻ and I⁻ interrupt it.¹⁵⁰⁻¹⁵¹

In this study, we explored how I⁻ altered the growth mode of Cu in the presence of hexadecylamine (HDA). Unlike syntheses with Cl⁻ that result in nanowires, the addition

of I⁻ resulted in 2D nanoplates. Single-crystal electrochemistry revealed that the rate of atomic addition of Cu was greater on {100} facets than on {111} in the presence of I⁻. Compared to synthetic findings, the selective promotion of Cu addition on {100} facets drove lateral growth of nanoplates while effectively hampering Cu deposition on {111} basal surfaces.

4.1 Synthetic Observations of Cu Nanoplate Growth

The synthetic results shown in Figure 33a–c demonstrate the dramatic effect of halide ions on Cu nanocrystal growth modes. The addition of Cl⁻ to a growth solution containing a Cu(II) precursor, HDA, and ascorbic acid (AA) (herein referred to as HDA·Cl⁻ solution) resulted in pentagonally-twinned Cu nanowires (Figure 33a). Prior research has demonstrated that nanowire growth can be attributed to facet-selective adsorption of Cl⁻ on {111} facets, allowing HDA to form a passivating SAM on {100} and leave {111} end facets open to addition.^{41, 47} Whereas Cl⁻ took on the role of a selective activator, the addition of I⁻ in place of Cl⁻ (forming the HDA·I⁻ solution) did not cause anisotropic growth, yielding spherical Cu particles instead (Figure 33b). Interestingly, the combination of both Cl⁻ and I⁻ (i.e., HDA·Cl⁻·I⁻ solution) induced Cu nanoplate formation with an average thickness of 130 ± 30 nm, an average width of 4.0 ± 1.5 μm , and an aspect ratio of 31 (Figure 33c,d).

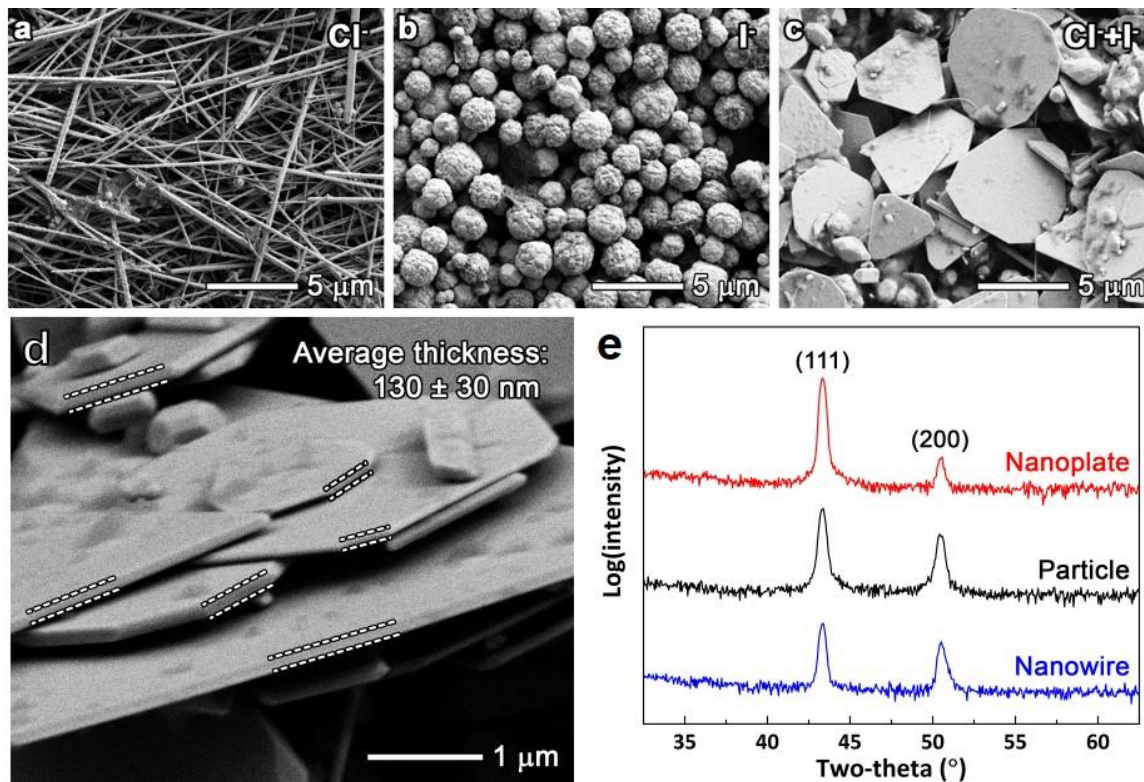


Figure 33: Cu nanostructures synthesized with HDA, AA, and different combinations of Cu precursors and halide ions: (a) nanowires from CuCl_2 , (b) spherical particles from $\text{Cu}(\text{NO}_3)_2$ with NaI , and (c) nanoplates from CuCl_2 with NaI . (d) A representative SEM image used to measure the average thickness of Cu nanoplates. (e) XRD patterns for Cu nanowires, spherical particles, and nanoplates shown in (a-c). The concentrations of Cu precursors, HDA, AA, and NaI were 16.4 mM, 49.4 mM, 50 mM, and 75 μM, respectively.

Although there is still some debate on the crystallinity of the lattice planes that comprise nanoplate edges (Table 7), most researchers agree that FCC metals form hexagonal nanoplates consisting of two {111} basal surfaces and 12 alternating {100} and {111} side planes.¹⁵²⁻¹⁵⁴ To help visualize the atomic structure, we created models of the Cu nanoplates in Figure 34. Our models indicate that the number of twin layers along the horizontal plane of the nanoplate determines the presentation of {111} and {100} facets on

the sides. When there is no twin layer or the number of twin layers is even, the side facets alternate vertically and laterally between {111} and {100} in a checkerboard pattern (Figure 34a). When the number of twin layers is odd, the {111} and {100} facets alternate only laterally in columns (Figure 34b). Previous findings have also suggested that metal atomic addition is facilitated on {100} edge facets rather than {111} edge and basal facets, so in addition to lateral anisotropic growth, hexagonal nanoplates are gradually truncated into nanotriangles.¹⁵³ In sum, the change in growth mode from nanowires to nanoplates with the addition of I implies that an inversion in facet activity occurs such that greater Cu addition takes place on {100} than {111}.

Table 7: The Crystal Structure of Metal Nanoplates Reported in Previous Research

Metal	Plate shape	Basal Facet	Side Facets	Citation
Ag	Triangle & Hexagon	{111}	{100} & {111}	152-153, 155-157
Pd	Triangle & Hexagon	{111}	{100} & {111}	158-159
Au	Triangle & Hexagon	{111}	{100} & {110}	160
Cu	Triangle & Hexagon	{111}	{100} & {110}	60
	Triangle	{111}	{110}	56
Ni-Cu	Hexagon	{111}	{100} & {111}	161
	Triangle	{111}	{100}	

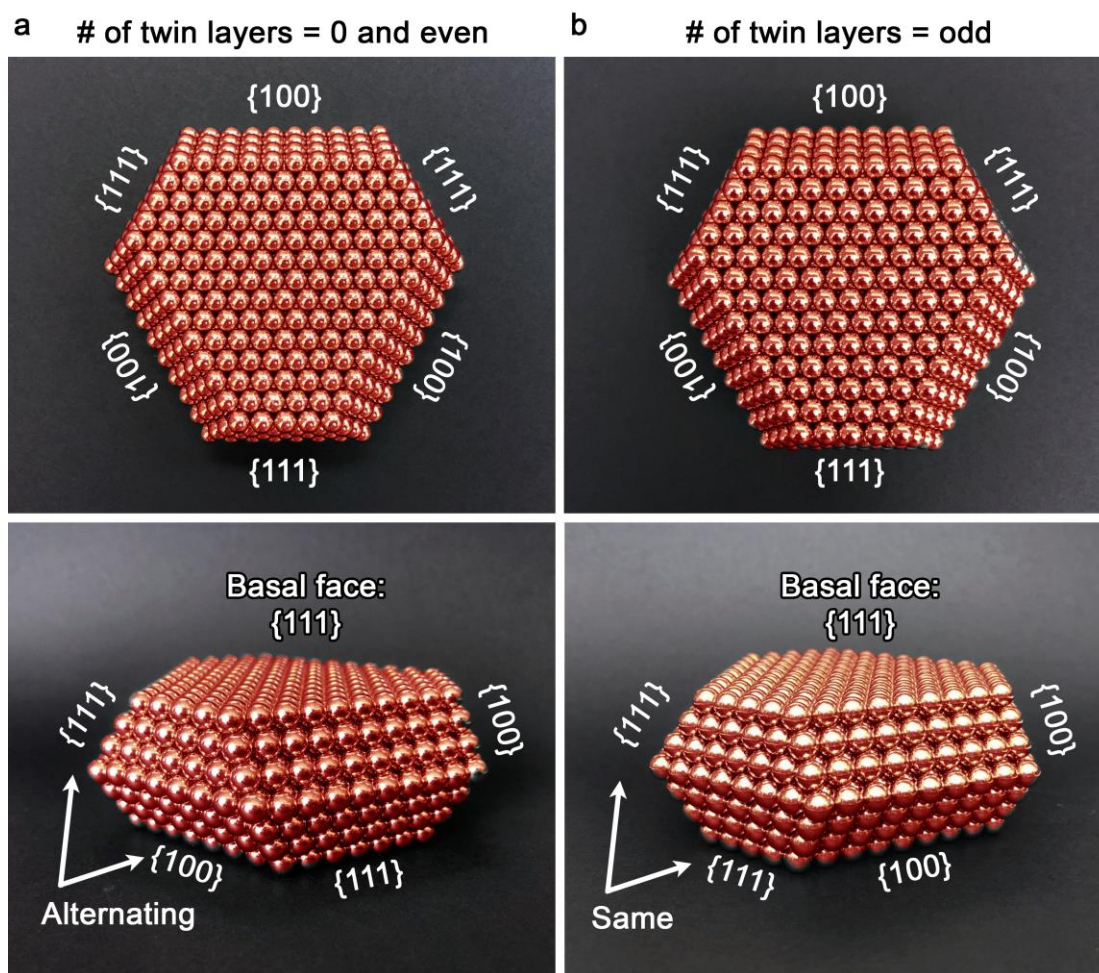


Figure 34: Two models demonstrating the atomic arrangement of Cu in hexagonal nanoplates using an FCC packing of spherical magnets (a) without a twin layer and (b) with one twin layer. The sides of the hexagonal nanoplates consist of $\{111\}$ and $\{100\}$ facets while the basal surfaces are enclosed by $\{111\}$ facets.

Preferential Cu facet growth under the influence of halides was further observed by introducing nanoplate seeds (initially grown with the HDA-Cl-I solution) to the HDA-Cl solution (Figure 35). Although it was impossible to prevent the formation of nanowires, the nanoplates became 2.3 times thicker while their widths remained within

error of each other (before seeded growth: $4.0 \pm 1.5 \mu\text{m}$, after: $4.4 \pm 1.0 \mu\text{m}$). This result clearly indicates that Cl⁻ selectively promoted Cu atomic addition on the {111} basal planes of the nanoplate seeds, resuming its anticipated behavior as a facet-selective activator.

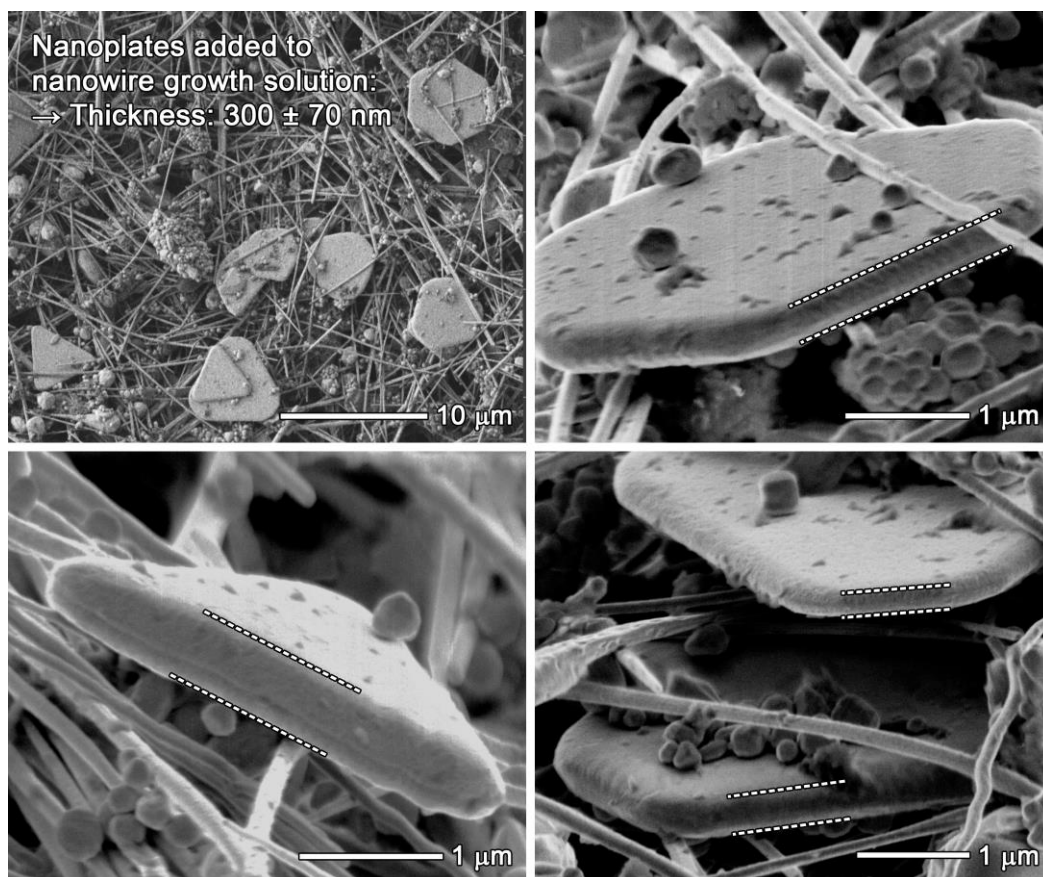


Figure 35: SEM images of Cu nanoplates after seeded growth in which Cu nanoplates from Figure 33c were added to a Cu nanowire growth solution (HDA-Cl⁻).

4.2 Electrochemical Measurements of Cu Reduction Rates on Cu Single-Crystal Electrodes

To corroborate the effect of halide ions on the growth of Cu nanocrystals, electrochemical measurements with Cu(111) and Cu(100) single-crystal electrodes were

performed in the growth solutions, a method previously used to investigate rates of atomic addition.^{47, 50} As described in mixed potential theory,⁶⁴⁻⁶⁵ all electrons from the oxidation of reducing agents are funneled into the reduction of Cu-alkylamine complexes (i.e., oxidation rate = reduction rate). At the mixed potential (E_{mp} , the potential where spontaneous redox reactions occur), the resulting current is zero and can be observed via linear sweep voltammetry (LSV). The net current is a result of having equal and opposite partial currents for oxidation and reduction, which each corresponds to the reaction rate of Cu nanocrystal growth at E_{mp} . As shown in Figure 36a, Tafel plots of LSVs were used to extract the partial current density at E_{mp} (referred to as j_{mp}), and the ratio of j_{mp} for the two single-crystal electrodes ($j_{mp}^{(100)}/j_{mp}^{(111)}$) was used to compare the Cu atomic addition activities.

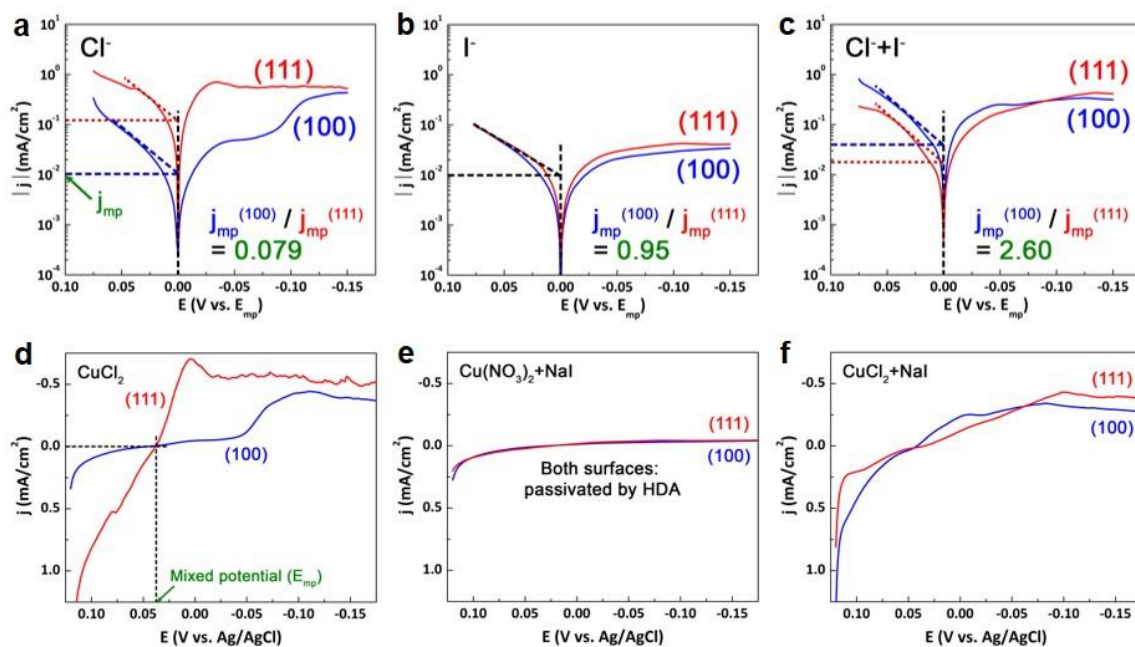


Figure 36: (a–c) Tafel plots for two Cu single-crystal electrodes obtained with the same reaction solutions as Figure 33a–c, respectively. (d–f) The corresponding LSVs.

Figure 36a depicts the Tafel plots obtained in the HDA- Cl^- solution. The partial currents for both reduction and oxidation were greater for the (111) electrode than the (100), and $j_{mp}^{(111)}$ was 12.7 times greater than $j_{mp}^{(100)}$. Various j_{mp} values according to the electrolyte composition and single-crystal electrode are summarized in Figure 37. Since the growing ends of pentagonally-twinned Cu nanowires are enclosed by {111} facets, and the sides are covered by {100} facets, the greater value of $j_{mp}^{(111)}$ in comparison to $j_{mp}^{(100)}$ agreed with the anisotropic growth of Cu nanowires.⁴⁷

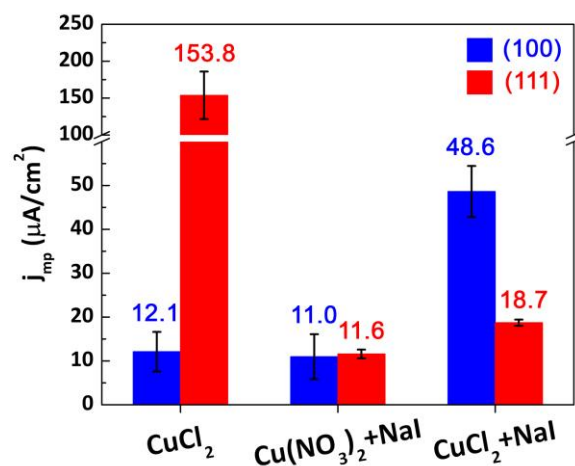


Figure 37: The current densities at mixed potential (j_{mp}) measured from the Tafel plots shown in Figure 36a–c. The values in the graph correspond to average j_{mp} .

On the other hand, both j_{mp} values in the HDA- I^- solution significantly decreased compared to the HDA- Cl^- solution (Figure 36b and Figure 37) and were similar to previously reported values obtained in a solution containing Cu(II), HDA, and AA without any halide ions.⁴⁷ The agreement between the two measurements indicate that in this instance, both (111) and (100) electrodes were passivated by HDA without any facet-selective behavior ($j_{mp}^{(100)}/j_{mp}^{(111)} = 0.95$). However, the addition of I^- to the HDA- Cl^- solution (i.e., HDA- Cl^- - I^- solution) elicited a dramatic change in the facet-selective chemistry. Figure 36c shows a 2.6 times greater j_{mp} for the (100) electrode compared to the (111), the opposite of what was observed in the HDA- Cl^- solution (Figure 36a). This inversion supports the hypothesis that I^- facilitates greater Cu atomic addition to the {100} edge facets than to the {111} basal planes, ultimately resulting in nanoplate formation.

The $j_{mp}^{(111)}$ and $j_{mp}^{(100)}$ values of the HDA-Cl-I⁻ solution were further investigated by varying the concentration of I⁻ (Figure 38a). Interestingly, increasing the I⁻ concentration had opposing effects on each facet: reducing $j_{mp}^{(111)}$ and increasing $j_{mp}^{(100)}$. Moreover, there was also a correlation between the $j_{mp}^{(100)}/j_{mp}^{(111)}$ ratio and nanoplate yield ($N_{\text{nanoplates}} / (N_{\text{nanoplates}} + N_{\text{nanowires}}) \times 100$, where N equals the number of nanocrystals) as the I⁻ concentration was increased (Figure 38b). Of note, when the value of $j_{mp}^{(100)}/j_{mp}^{(111)}$ was over 2.5, the percent of nanoplates exceeded 85%, whereas the yield decreased to 36% when the $j_{mp}^{(100)}/j_{mp}^{(111)}$ was 0.31. These results signify that the $j_{mp}^{(100)}/j_{mp}^{(111)}$ can be used as a predictor for the formation of nanoplates.

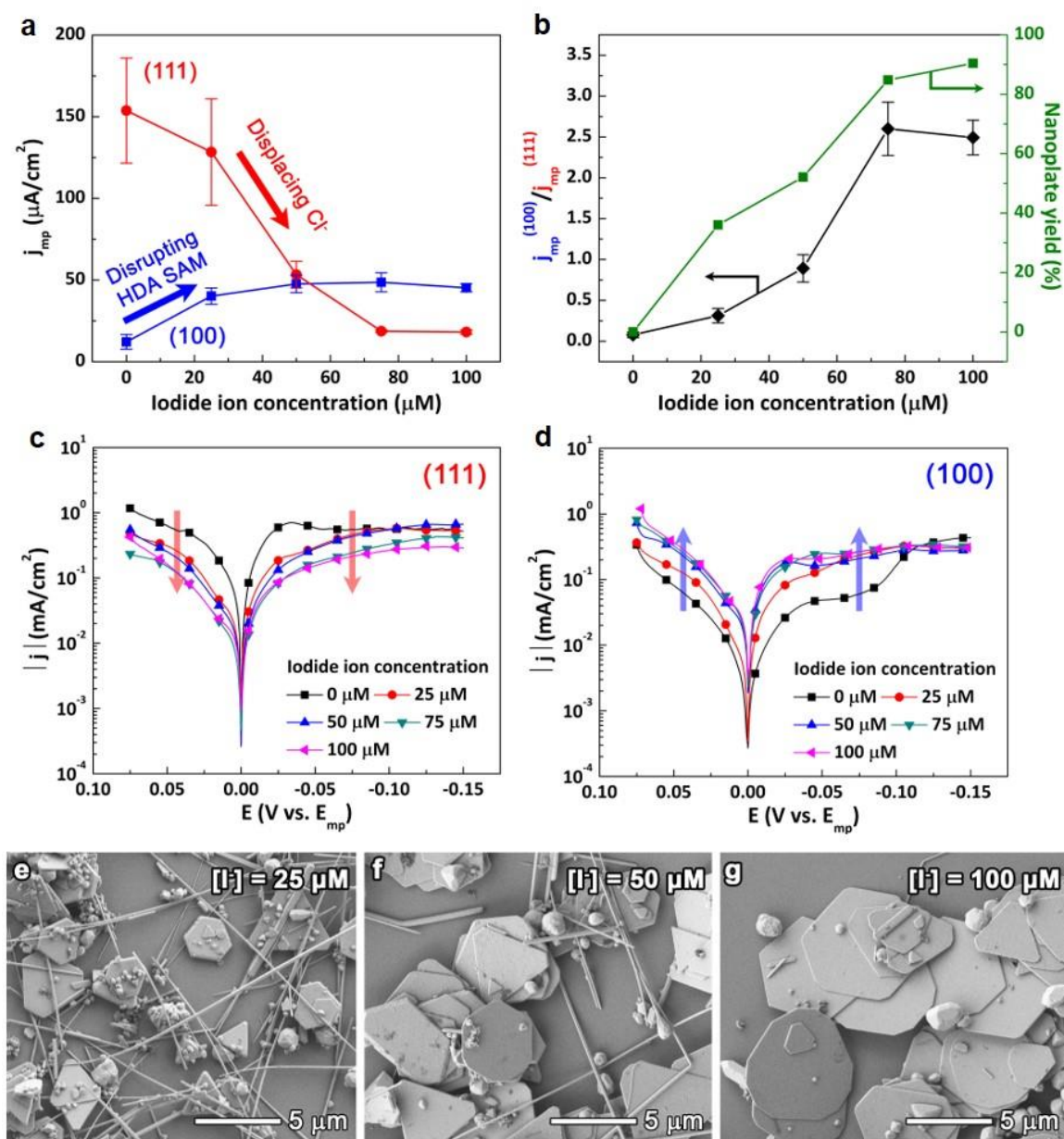


Figure 38: Electrochemical and synthetic results demonstrating the passivation and activation effects of I^- on $\{111\}$ and $\{100\}$ facets. (a) Values of $j_{mp}^{(100)}$ and $j_{mp}^{(111)}$ and (b) $j_{mp}^{(100)}/j_{mp}^{(111)}$ (diamonds) and the percent of nanoplates (squares) as a function of I^- concentration. (c–d) Corresponding Tafel plots for (a–b) for $\{111\}$ and $\{100\}$ single-crystal electrodes obtained with electrolytes containing 16.4 mM $CuCl_2$, 49.4 mM HDA, and 50 mM ascorbic acid. The I^- concentration varied from 0 to 100 μM . The arrows on the graphs indicate the changes in current density with the addition of I^- . (e–g) Representative SEM images used for measuring plate yields at I^- concentrations of 25, 50, and 100 μM .

Figure 38a demonstrated that the effect of I⁻ on j_{mp} depends on the crystal facet. Atomic addition on {111} facets becomes more difficult with increasing concentrations of I⁻ while atomic addition on {100} facets is facilitated. We hypothesized that the opposite behaviors displayed by I⁻ are due to the fact that the surface chemistries of the {111} and {100} facets differ in the presence of HDA and Cl⁻. To illustrate this hypothesis, the schematic in Figure 39a shows how the composition of {111} and {100} surfaces in an HDA-Cl⁻ solution changes as increasing concentrations of I⁻ is introduced. When there is no I⁻ present (0 μ M I⁻, left side of the schematic), the {111} surface is covered exclusively by Cl⁻ (which activates the surface for atomic addition) and the {100} surface is passivated by an HDA SAM and co-adsorbed Cl⁻.⁴⁷ As increasing concentrations of I⁻ is introduced, Cl⁻ on the {111} facet is displaced by I⁻. We observed that the change in {111} surface conditions resulted in a lesser $j_{mp}^{(111)}$ value for the HDA-Cl⁻-I⁻ solution compared to the HDA-Cl⁻ solution, suggesting atomic addition on the (111) electrode decreased. On the other hand, Figure 39a shows I⁻ disrupted the HDA SAM on the {100} facet, resulting in a surface covered by I⁻ and Cl⁻. Since the primary role of the HDA SAM was to passivate or prevent atomic addition and we observed a spike in the $j_{mp}^{(100)}$ in the HDA-Cl⁻-I⁻ solution compared to the HDA-Cl⁻ solution, it appears that atomic addition on the (100) electrode increased.

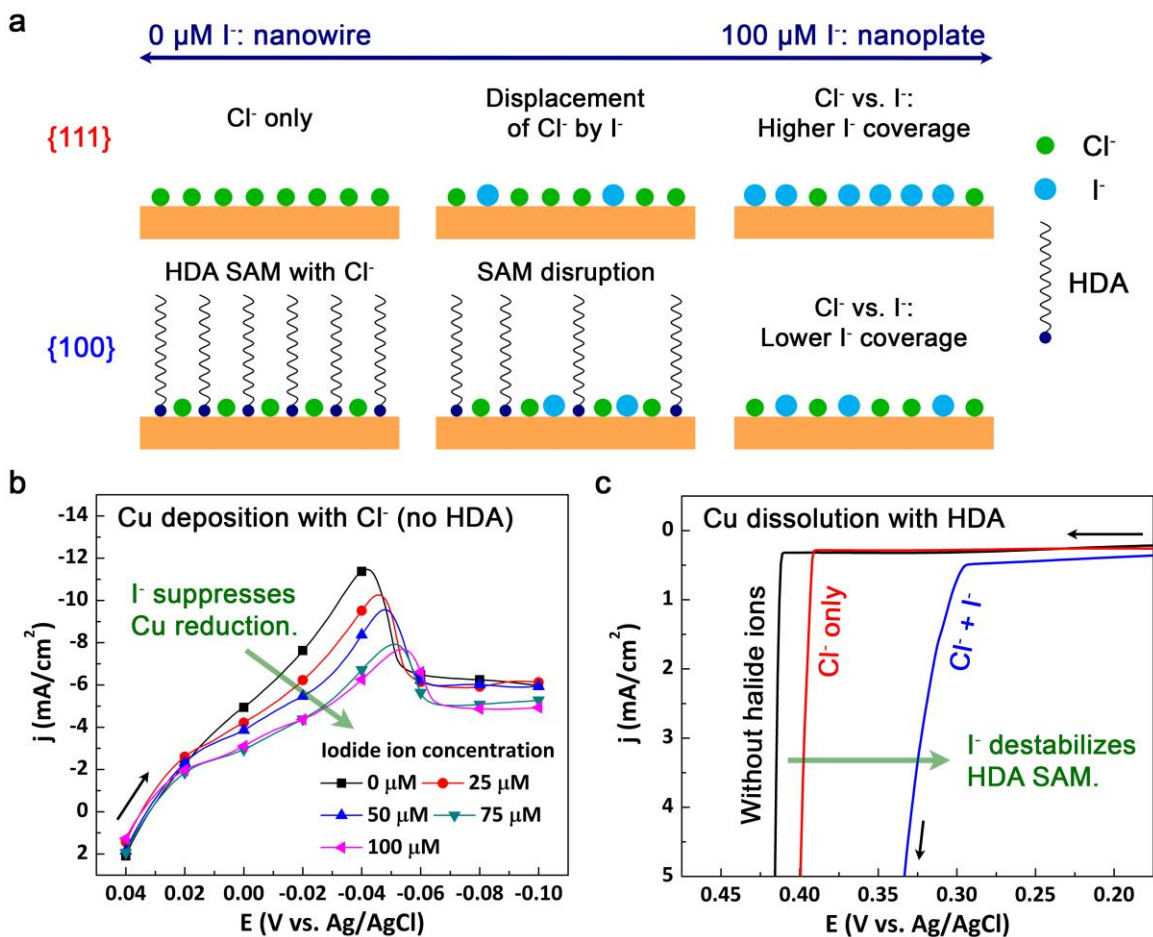


Figure 39: The role of competitive adsorption of Cl⁻ and I⁻ in the growth of Cu nanoplates. (a) Schematic diagram of Cu {111} and {100} facets in an HDA-Cl⁻ solution with varying concentrations of I⁻. (b) LSVs for Cu ion reduction on a polycrystalline Cu electrode in electrolytes containing 16.4 mM CuCl₂ and various concentrations of I⁻ to confirm the effect of I⁻ on Cl⁻-covered Cu surfaces. (c) LSVs for Cu dissolution of a polycrystalline Cu electrode in electrolytes containing 49.4 mM HDA with and without halide ions to verify the effect of I⁻ on HDA-covered Cu surfaces. The concentrations of Cl⁻ and I⁻ used in (b) were 32.8 mM and 75 μM , respectively. The black arrows indicate the direction of the potential sweep.

To validate our hypothesis, we investigated the effect of I⁻ concentration on the different surface chemistries present in the {111} and {100} surfaces independent of one

another. To elucidate the effect of I⁻ on the Cl⁻-activated Cu {111} facets, LSVs of Cu ion reduction in a solution containing only Cu(II), Cl⁻, and varying concentrations of I⁻ (no HDA) were measured (Figure 39b). LSVs of anodic Cu dissolution on a polycrystalline Cu electrode were obtained in solutions containing HDA with and without halide ions (Figure 39c), which mimic the effect of I⁻ on the HDA-passivated Cu {100} facets.

The LSVs for Cu deposition (Figure 39b) indicated that adding more I⁻ to the CuCl₂ solution continuously passivated the (111) electrode to Cu addition. The bond between I⁻ and Cu is likely stronger due to its covalency compared with the Cl⁻ and Cu bond, which is most likely ionic.¹⁶² As a result, adsorbed Cl⁻ is more mobile than I⁻ on the Cu surface, the latter increasing charge transfer resistance for Cu deposition.¹⁵¹ The decrease in current associated with Cu deposition confirms that the decrease in $j_{mp}^{(111)}$ as the I⁻ concentration increases (Figure 38a) is due to the adsorption of I⁻ displacing Cl⁻ on the (111) electrode, which is described in the top schematics in Figure 39a.

It is worthwhile to note that although an HDA SAM monolayer more strongly prohibits Cu atomic addition than I⁻, leading one to believe that HDA may passivate {111} facets in the HDA-Cl-I⁻ solution, Figure 40 confirms the decrease in $j_{mp}^{(111)}$ was due to the coverage of I⁻ on the (111) electrode rather than HDA. Figure 40 shows that the LSV of a Cu(100) electrode in an HDA-Cl⁻ solution features a current plateau between -0.04–0.05 V indicative of a passivating HDA SAM.⁴⁷ However, no current plateau was observed for the Cu(111) electrode in the HDA-Cl-I⁻, suggesting no HDA SAM was present on the (111)

surface. These results validate that the inhibition of Cu atomic addition on the {111} basal planes was caused by adsorbed I⁻. This also explains why the effect of I⁻ concentration on {111} facets can be investigated in the absence of HDA.

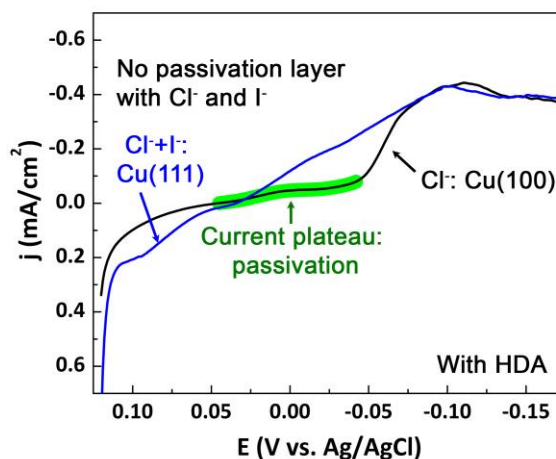


Figure 40: LSVs for the (100) electrode in an HDA-Cl⁻ solution, and the (111) electrode in an HDA-Cl⁻-I⁻ solution. The concentrations of CuCl₂, HDA, NaI, and AA were 16.4 mM, 49.4 mM, 75 μM, and 50 mM respectively.

Next, the effect of I⁻ on HDA-covered {100} facets was investigated by comparing the stability of HDA SAM with and without halide ions. Figure 39c shows LSVs for Cu dissolution performed in electrolytes containing only HDA and halide ions. In the absence of halide ions, a potential of 0.41 V was necessary to disrupt the HDA SAM and initiate Cu dissolution. However, the presence of Cl⁻ reduced the potential required for Cu dissolution to 0.39 V, while a combination of Cl⁻ and I⁻ had a more dramatic effect on destabilizing the HDA SAM, lowering the Cu dissolution potential to 0.29 V. These results

indicate that the combination of I⁻ and Cl⁻ effectively disrupts the HDA SAM, facilitating electrochemical reactions on the Cu surface. As discussed above, I⁻ is weaker when it comes to suppressing Cu deposition compared to an HDA SAM. Therefore, the disruption of the HDA SAM by I⁻, a weaker passivator, could cause the $j_{mp}^{(100)}$ to increase (Figure 38a). I⁻ appears to behave as an activator for {100} facets only when the $j_{mp}^{(100)}$ of the HDA-Cl⁻-I⁻ solution is compared to that of the HDA-Cl⁻ solution because without I⁻, the Cu(100) electrode is covered by a stronger passivation layer of HDA.

4.3 Conclusion

Through single-crystal electrochemistry, this work clarifies the modulating effect of I⁻ on Cu nanocrystal formation. In the presence of I⁻, Cl⁻, and HDA, Cu reduction is favored on {100} facets, resulting in the lateral growth of Cu nanowires. Moreover, the ratio of $j_{mp}^{100}/j_{mp}^{111}$ increased with I⁻ concentration, alluding to its passivation effect on the {111} basal surfaces. This effect was in line with synthetic observations that showed larger, thinner Cu nanoplates were produced when we increased I⁻ concentration. We also demonstrated that, when paired with I⁻, Cl⁻ plays a crucial role in the growth of Cu nanoplates by producing a synergistic effect in destabilizing the HDA SAM on {100} surfaces. While this work has shed light on the mechanism of Cu nanoplate formation, further insight is necessary to clarify the opposing effects of I⁻ on {111} and {100}.

Computer simulations using DFT can further illuminate the surface composition of the {111} and {100} facets that results in the lateral growth of Cu nanoplates.

5. Conclusions

In conclusion, this work discussed efforts in advancing the wide-spread application of Cu nanocrystals in electronic and catalytic applications. This was done by first demonstrating a rapid and easy multigram-scale synthesis of stable Cu-Ag nanowires, which enabled us to take advantage of the unique properties of nanocrystals and utilize them in applications that required relatively large quantities. The nanowires exhibited excellent conductive properties when integrated into a thermoplastic, enabling the production of the most electrically conductive 3D printing filament to date. The flexibility of a nanowire network was also beneficial in producing a highly stretchable conductor for potential use in wearable electronics. Finally, the high surface area of a Cu nanowire felt resulted in the improvement of the productivity of a flow-through electrode.

We also introduced a simple method for tailoring the reaction kinetics of a colloidal synthesis to tune the aspect ratio of short Cu nanowires. The self-heated approach offers an energy-efficient approach to nanocrystal synthesis and streamlines the process of Cu nanowire production. The work discussed in Chapter 2 represents just a small step towards the implementation of metal nanocrystals in new and innovative technologies. Future efforts are necessary to further increase the scale at which Cu-Ag nanowires can be synthesized and decrease the cost of production before they can be viable materials for transparent conductive electrodes, electronic devices, and wearable electronics.

Finally, single-crystal electrochemistry was used to understand the role of I⁻ on the growth of Cu nanoplates, offering more detail on the importance of halides in the anisotropic growth of nanocrystals. However, some questions remain regarding the surface activation effect of I⁻ on different Cu crystal facets. Compared to Cu nanowires, the growth of Cu nanoplates is not as well-understood. Thus, by clarifying its growth mechanism, we hope to increase the impact of Cu nanoplates in electronic and catalytic applications.

6. Experimental Procedures

6.1 Multigram-Scale Synthesis of Cu Nanowires

6.1.1 High Aspect Ratio Cu Nanowires

The multi-gram scale synthesis of Cu nanowires with an average length of 45 ± 15 μm and an average diameter of 240 ± 95 nm was first developed in this work. In this 10-L scale reaction, 800 mL 0.1 M $\text{Cu}(\text{NO}_3)_2 \cdot 2.5\text{H}_2\text{O}$ ($\geq 98\%$, Sigma-Aldrich), 7.5 L 8 M NaOH (99.0%, NOAH Technologies), and 115 mL ethylenediamine (EDA, $\geq 99\%$, Sigma-Aldrich) were sequentially added in a 10-L polypropylene bottle, shaking by hand after each addition. Next, 750 mL 1 g/mL α -D-glucose (96%, Sigma-Aldrich) aqueous solution was added to the reaction solution, mixed thoroughly by shaking the bottle, and immediately placed in a 60°C water bath for 1 h. Appropriate personal protective equipment (e.g., face mask, rubber apron, and elbow-length rubber gloves) were worn to ensure safety while handling the highly basic reaction solution, especially at such large volumes. The synthesis was repeated five times, yielding approximately 22 g of Cu nanowires.

The synthesized Cu nanowires were purified by first separating the Cu nanowires from the reaction solution using a stainless-steel mesh strainer. The Cu nanowires were resuspended in a 400 mL aqueous solution containing 3 wt% polyvinylpyrrolidone (PVP, avg MW 10,000, Sigma-Aldrich) and 1 wt% *N,N*-diethylhydroxylamine (DEHA, $>95.0\%$, TCI America) (PVP/DEHA). The nanowires were further purified through gravity filtration using a custom-made funnel fitted with a stainless-steel mesh (30 μm pore size)

and rinsed with three aliquots of 250 mL PVP/DEHA. The purified Cu nanowires were stored in PVP/DEHA at a concentration of 4.5 mg/mL.

A smaller-scale synthesis was used to produce Cu nanowires with an average length of 50 μm and an average diameter of 230 nm. In a 2-L Pyrex bottle, 160 mL 0.1 M $\text{Cu}(\text{NO}_3)_2 \cdot 2.5\text{H}_2\text{O}$, 1.5 L 8 M NaOH, and 23 mL EDA were combined, shaking thoroughly after each addition. Next, 150 mL of 1 g/mL glucose solution was added to the reaction solution, mixed thoroughly, then placed in a 60°C oven for 4 h. Cu nanowires with an average length of 30 μm and an average diameter of 120 nm were synthesized in a similar manner, except the amount of glucose solution added was increased to 250 mL. The Cu nanowires were purified by carefully decanting out about 80% of the reaction solution, then precipitating the Cu nanowires via centrifugation (2000 rpm for 10 min). The supernatant was discarded, and the nanowires were rinsed in triplicate with 200 mL PVP/DEHA, vortexing for 30 s before centrifuging. The nanowires were stored in PVP/DEHA at a concentration of 1.6 mg/mL.

6.1.2 Synthesis of Ag and Cu-Ag Nanowires

Ag nanowires with an average length of 20 μm were synthesized based on a polyol method previously reported by Wiley et al.¹⁶³⁻¹⁶⁴ In a 500-mL round-bottom flask, 158.4 mL ethylene glycol (EG, J. T. Baker) was heated in a 125°C oil bath for 30 min. Meanwhile, the following solutions were prepared: (1) 257 mg NaCl (Fisher Scientific) in 20 mL EG,

(2) 81 mg $\text{Fe}(\text{NO}_3)_2$ (Sigma-Aldrich) in 10 mL EG, (3) 1.05 g PVP (avg MW = 55,000, Sigma-Aldrich) in 25 mL EG, and (4) 1.05 g AgNO_3 in 25 mL EG. While stirring the heated EG in the round-bottom flask at 150 rpm, 0.2 mL of Solution 1, 0.1 mL of Solution 2, 20.76 mL of Solution 3, and 20.76 mL of Solution 4 were sequentially added at 30 s intervals. After 5 min, the temperature of the oil bath was increased to 130°C for 6 h. The Ag nanowires were purified via centrifugation (1000 rpm, 20 min) and rinsing with acetone (VWR) three times.

Cu nanowires synthesized in the multigram-scale from Section 5.1.1 were coated with Ag by mixing together the Cu nanowires in PVP (5 L, 4.5 mg/mL), 10 L of 4 wt% PVP solution, and 27.5 L of 1 M L-ascorbic acid (>99.0%, Duda Energy) in a 15-gallon polypropylene inductor tank with an overhead mixer for 15 min under ambient conditions. AgNO_3 (1416 mL, 25 mM, $\geq 99.7\%$, Fisher Scientific) was added at 0.5 mL/s using a peristaltic pump, and the reaction solution was stirred for an additional 5 min after completely adding AgNO_3 . To retrieve the Cu-Ag nanowires, the reaction solution was passed through a custom-made funnel fitted with a stainless-steel mesh (30 μm pore size). The Cu-Ag nanowires were then rinsed three times with de-ionized water via centrifugation (2000 rpm, 10 min).

Cu-Ag nanowires with different Ag:Cu mol ratios were also synthesized but at a smaller scale. A solution containing 2 mL 1.6 mg/mL Cu nanowires in PVP/DEHA, 2 mL 4 wt% PVP solution, and 5.5 mL 1 M L-ascorbic acid was stirred for 5 min. Varying

amounts of 25 mM AgNO₃ (0.03 mol ratio: 60 μL, 0.04 mol ratio: 80 μL, 0.05 mol ratio: 100 μL, 0.06 mol ratio: 120 μL, and 0.07 mol ratio: 140 μL) were added to the solution and stirred for 3 min. The Cu-Ag nanowires were purified via centrifugation (2000 rpm, 10 min) and rinsed three times with PVP/DEHA.

To confirm the Cu-Ag core-shell structure of the nanowires, X-ray diffraction (XRD) analysis and scanning transmission electron microscopy paired with energy dispersive X-ray spectroscopy (STEM-EDS) were conducted. XRD samples were prepared by resuspending the Cu and Cu-Ag nanowires in isopropanol and drop-casting them onto glass slides and were analyzed on a Panalytical X'Pert PRO MRD HR. STEM-EDS samples were prepared by resuspending Cu-Ag nanowires in de-ionized water and drop-casting them on a holey carbon TEM grid (Ted Pella), and images were obtained with an FEI Titan 80-300.

6.1.3 Preparation of Samples Containing High Aspect Ratio Nanowires

For the samples discussed in Figure 17, Cu and Cu-Ag nanowires (0.3–0.7 mol ratio Ag:Cu) were each dispersed in 1 mL nitrocellulose ink. Various amounts of nanowire-ink solution containing 0.64 mg of Cu and Cu-Ag nanowires were drop-casted into circular wells formed by double-sided tape. One set of samples was placed in a 150°C drying oven for 24 h, then measured for resistivity with a four-point probe. Another set was trimmed into rectangles and had Ag paste applied on the short ends, then placed in a humidity

chamber set to 85% relative humidity (RH) and 85°C. The resistance of each sample was measured with a multimeter periodically over 24 h, then converted to resistivity using the exact dimensions of each sample.

To test the effect of nanowire composition on resistivity (Figure 21), varying quantities of Cu-Ag nanowires, Ag nanowires, and Ag flakes ($\geq 99.9\%$, 10 μm , Sigma-Aldrich) were added to dichloromethane (DCM, VWR) containing 1 g of polycaprolactone (PCL) pellets (IC3D Printers, LLC). The composites were vortexed until the PCL pellets were completely dissolved, then cast into rectangular silicone wells and allowed to dry until all the DCM had evaporated. Nonuniform edges were trimmed and Ag paste was applied to the short ends. The resistance of each sample was measured with a multimeter, then converted to resistivity.

6.1.4 Cu-Ag Nanowire Filament Production and 3D Printing

A highly conductive thermoplastic filament for 3D printing was produced containing 12:88 volume ratio of Cu-Ag nanowires to PCL. The Cu-Ag nanowires from Section 5.1.2 were washed three times with methanol (VWR), then dispersed in 1.5 L DCM. To this, 22 g of PCL pellets were added and stirred for 1 h until completely dissolved. The liquid composite was transferred to a glass tray and stirred every few minutes to maintain a homogenous dispersion until most of the DCM had evaporated. Once a thick paste-like consistency was reached, the composite was spread out in a thin

layer and allowed to completely harden overnight. The hardened nanowire/PCL composite was cut into 5 x 5 mm pellets and further dried in a 50°C oven for 2 h. The dried pellets were then fed into a Filabot filament extruder heated to 120°C and fitted with a 1.6 mm nozzle.

The nanowire filament was then used to 3D print the inductive charging coil shown in Figure 25 using a HICTOP Prusa I3 printer fitted with a 1 mm nozzle at a print speed of 15 mm/s and extrusion temperature of 160°C. Before printing, a 3D model of the charging coil was rendered on Fusion 360, then converted to a printable gcode using Cura (slicing software for 3D printing). An LED was attached to the coil using alligator clips coated with Ag paste to reduce contact resistance.

6.1.5 Low Aspect Ratio Nanowires

Various sizes of short nanowires were synthesized by combining 31.25 mL 0.2 M $\text{Cu}(\text{NO}_3)_2 \cdot 2\frac{1}{2} \text{H}_2\text{O}$, 625 mL 15 M NaOH, and 8 mL EDA in a 2-L Pyrex bottle, shaking well after each addition, then pre-heating to 50°C in a large water bath. Glucose solutions of varying concentrations (1.0, 0.6, 0.4, and 0.2 g/mL) were prepared by dissolving α -D-glucose in de-ionized water that was heated to 85°C, then stirring at 900 rpm until the glucose dissolved completely. At room temperature, 250 mL of the appropriate glucose solution (pre-heated to 50°C) was rapidly added to the Cu/NaOH/EDA solution while stirring with an overhead stirrer at 500 rpm for 15 s. The reaction solution was left at room

temperature under ambient conditions for 15 min, within which time the nanowires formed.

To begin purification, the nanowires were precipitated out of the reaction solution by adding 250 mL of PVP/DEHA and shaking vigorously, which causes the Cu nanowires to float to the top and form a dense cake. After most of the reaction solution was carefully decanted out to separate it from the Cu nanowires, the nanowire cake was transferred to 250 mL centrifuge tubes and centrifuged for 10 min at 2500 rpm. The supernatant was discarded, and the nanowires were rinsed four times with 200 mL aliquots of PVP/DEHA, vortexing for 30 s and centrifuging between each rinse. The Cu nanowires were stored in PVP/DEHA at a concentration of 1 g/mL.

Atomic absorption spectroscopy (AAS) was used to determine the yield of reduced Cu in Figure 18c. Measured aliquots of each Cu nanowire sample were rinsed with and suspended in de-ionized water. The nanowires were then dissolved with a minimal amount of concentrated nitric acid (85%, VWR). The samples were further diluted with de-ionized water to a known volume, then analyzed with the AAS. A calibration curve was used to find the concentration of nanowires in the initial aliquot and the total experimental yield. Finally, the experimental yield was compared to the initial amount of Cu added to the synthesis.

Images obtained through SEM (FEI XL30 SEM-FEG) were used to measure the dimensions of the Cu nanowires. The samples were prepared by suspending the Cu nanowires in de-ionized water and drop-casting them onto a silicon wafer.

6.2 Synthesis and Analysis of Cu Nanocrystals

6.2.1 Synthesis of Cu nanocrystals

Cu nanowires were synthesized by preparing a 15-mL aqueous solution containing 16.4 mM $\text{CuCl}_2 \cdot 2\text{H}_2\text{O}$ ($\geq 99.0\%$, Sigma-Aldrich) and 49.4 mM hexadecylamine (HDA, 90%, Aldrich Chemistry) in a 20-mL glass vial. The solution was stirred rapidly overnight, after which ascorbic acid (50 mM, $\geq 99\%$, Sigma-Aldrich) was added and vortexed for 30 s. The reaction solution was placed in a 90°C oven for 17 h, then purified through centrifugation (1500 rpm for 10 min). The supernatant was discarded from the Cu nanowire precipitate, which was then rinsed sequentially via vortex and centrifugation with isopropyl alcohol (IPA, VWR), hexane (VWR), and a solution containing 40 vol% IPA and 60 vol% de-ionized water by volume.

Cu nanoplates were synthesized and purified following the above procedure for Cu nanowires, with the exception of adding the appropriate concentration of NaI ($\geq 99.5\%$, Sigma-Aldrich) to the Cu-HDA solution before stirring overnight. Likewise, Cu nanoparticles were prepared by simply replacing the $\text{CuCl}_2 \cdot 2\text{H}_2\text{O}$ in the nanoplate synthesis with 16.4 mM $\text{Cu}(\text{NO}_3)_2 \cdot 2.5\text{H}_2\text{O}$ ($\geq 98\%$, Sigma-Aldrich) and following the purification method for Cu nanowires.

The shape and dimensions of the Cu nanocrystals were confirmed using a scanning electron microscope (SEM, Apreo S, Thermo Fisher Scientific). The samples were prepared by dispersing the purified products in IPA and drop-casting them onto silicon wafers.

6.2.2 Seeded Growth of Cu Nanoplates

Cu nanoplates were used as seeds in a Cu nanowire growth solution to demonstrate the facet selective growth of the nanocrystals in the presence of HDA and Cl⁻. First, a 14-mL solution containing 17.6 mM CuCl₂·2H₂O and 52.9 mM HDA was prepared in a 20-mL glass vial and stirred rapidly overnight. Next, 9 mg Cu nanoplates were dispersed in 1 mL 0.75 M ascorbic acid, stirring for 5 min. The two solutions were mixed together, vortexed for 30 s, then placed in a 90°C oven for 17 h. The final concentrations of CuCl₂·2H₂O, HDA, and ascorbic acid after mixing the two solutions were 16.4 mM, 49.4 mM, and 50 mM, respectively, matching the reaction conditions of the Cu nanowire synthesis detailed in Section 5.2.1.

6.2.3 Electrochemical Methods

The electrochemical measurement procedures used to analyze the growth mechanism of Cu nanocrystals were similar to those previously published by Kim et al.⁴⁷ Electrochemical measurements were conducted using a CHI600D potentiostat (CH

Instruments, Inc.) and a three-electrode system (Cu single-crystal or polycrystalline electrode as the working electrode, Pt wire as the counter electrode, and a Ag/AgCl reference electrode). Synthetic conditions were replicated by conducting all electrochemical measurements in a 90°C water bath and using the same solutions in Section 5.2.1, with the addition of 0.2 M KNO₃ (99%, Sigma-Aldrich) as the supporting electrolyte to eliminate the effects of solution resistance from the electrochemical measurements. The working electrodes were mechanically polished before each measurement with alumina particles (1.0 and 0.3 μm, Buehler) on Nylon pads, rinsing with de-ionized water between each step. The Cu(111) and Cu(100) single crystals were additionally electrochemically polished by applying 1.6 V (vs. Pt wire) in phosphoric acid (85%, Acros Organics) for 30 s, rinsed well with de-ionized water, then dried with N₂.

LSV with single-crystal electrodes was conducted by first placing the reaction solution of interest in a 90°C water bath. After 2 min, the working electrode was placed in the reaction solution, followed by the reference and counter electrodes after an additional 3 min. After waiting another 2 min, a potential sweep was applied from 0.12 V to -0.25 V (vs. Ag/AgCl) at a scan rate of 1 mV/s. The current-potential curves were replotted in log scale to create a Tafel plot and extract the current density at mixed potential (j_{mp}), as previously explained by Kim et al.⁴⁷

LSV was also conducted to determine the effect of I⁻ concentration on Cu deposition by using a polycrystalline Cu electrode and following the procedure detailed

above. The electrolyte solution contained 16.4 mM $\text{CuCl}_2 \cdot 2\text{H}_2\text{O}$ and various concentrations of NaI (0–100 μM), the potential sweep applied was from 0.04 V to -0.1 V (vs. Ag/AgCl), and the scan rate was 10 mV/s. To investigate the effect of different halide ions on HDA adsorption, the potential was swept from -0.1 V to 0.425 V at 10 mV/s in electrolyte solutions containing 49.4 mM HDA with i) no added halide ions, ii) 32.8 mM NaCl, and iii) 32.8 mM NaCl and 75 μM NaI.

References

1. Ruditskiy, A.; Peng, H.-C.; Xia, Y., Shape-Controlled Metal Nanocrystals for Heterogeneous Catalysis. *Annual Review of Chemical and Biomolecular Engineering* **2016**, *7* (1), 327-348.
2. Liu, L.; Corma, A., Metal Catalysts for Heterogeneous Catalysis: From Single Atoms to Nanoclusters and Nanoparticles. *Chem. Rev.* **2018**, *118* (10), 4981-5079.
3. Panthani, M. G.; Korgel, B. A., Nanocrystals for Electronics. *Annual Review of Chemical and Biomolecular Engineering* **2012**, *3* (1), 287-311.
4. Talapin, D. V.; Lee, J.-S.; Kovalenko, M. V.; Shevchenko, E. V., Prospects of Colloidal Nanocrystals for Electronic and Optoelectronic Applications. *Chem. Rev.* **2010**, *110* (1), 389-458.
5. Kagan, C. R., Flexible colloidal nanocrystal electronics. *Chem. Soc. Rev.* **2019**, *48* (6), 1626-1641.
6. and, S. L.; El-Sayed, M. A., Optical Properties and Ultrafast Dynamics of Metallic Nanocrystals. *Annu. Rev. Phys. Chem.* **2003**, *54* (1), 331-366.
7. Li, M.; Gou, H.; Al-Ogaidi, I.; Wu, N., Nanostructured Sensors for Detection of Heavy Metals: A Review. *ACS Sustainable Chemistry & Engineering* **2013**, *1* (7), 713-723.
8. Dykman, L.; Khlebtsov, N., Gold nanoparticles in biomedical applications: recent advances and perspectives. *Chem. Soc. Rev.* **2012**, *41* (6), 2256-2282.
9. Jeong, H.-H.; Choi, E.; Ellis, E.; Lee, T.-C., Recent advances in gold nanoparticles for biomedical applications: from hybrid structures to multi-functionality. *Journal of Materials Chemistry B* **2019**, *7* (22), 3480-3496.
10. Zhang, X., Gold Nanoparticles: Recent Advances in the Biomedical Applications. *Cell Biochemistry and Biophysics* **2015**, *72* (3), 771-775.
11. Rosi, N. L.; Mirkin, C. A., Nanostructures in biodiagnostics. *Chem. Rev.* **2005**, *105* (4), 1547-1562.
12. Yavuz, M. S.; Cheng, Y.; Chen, J.; Cobley, C. M.; Zhang, Q.; Rycenga, M.; Xie, J.; Kim, C.; Song, K. H.; Schwartz, A. G.; Wang, L. V.; Xia, Y., Gold nanocages covered by

- smart polymers for controlled release with near-infrared light. *Nature Materials* **2009**, *8* (12), 935-939.
13. Kottmann, J. P.; Martin, O. J. F.; Smith, D. R.; Schultz, S., Plasmon resonances of silver nanowires with a nonregular cross section. *Phys. Rev. B* **2001**, *64* (23), 235402.
 14. Wiley, B. J.; Im, S. H.; Li, Z.-Y.; McLellan, J.; Siekkinen, A.; Xia, Y., Maneuvering the Surface Plasmon Resonance of Silver Nanostructures through Shape-Controlled Synthesis. *The Journal of Physical Chemistry B* **2006**, *110* (32), 15666-15675.
 15. Sosa, I. O.; Noguez, C.; Barrera, R. G., Optical Properties of Metal Nanoparticles with Arbitrary Shapes. *The Journal of Physical Chemistry B* **2003**, *107* (26), 6269-6275.
 16. Yang, T.-H.; Peng, H.-C.; Zhou, S.; Lee, C.-T.; Bao, S.; Lee, Y.-H.; Wu, J.-M.; Xia, Y., Toward a Quantitative Understanding of the Reduction Pathways of a Salt Precursor in the Synthesis of Metal Nanocrystals. *Nano Lett.* **2017**, *17* (1), 334-340.
 17. Yang, T.-H.; Zhou, S.; Gilroy, K. D.; Figueroa-Cosme, L.; Lee, Y.-H.; Wu, J.-M.; Xia, Y., Autocatalytic surface reduction and its role in controlling seed-mediated growth of colloidal metal nanocrystals. *Proceedings of the National Academy of Sciences* **2017**, *114* (52), 13619-13624.
 18. Zhou, S.; Yang, T.-H.; Zhao, M.; Xia, Y., Quantitative analysis of the reduction kinetics of a Pt(II) precursor in the context of Pt nanocrystal synthesis. *Chinese Journal of Chemical Physics* **2018**, *31* (4), 370-374.
 19. Huo, D.; Kim, M. J.; Lyu, Z.; Shi, Y.; Wiley, B. J.; Xia, Y., One-Dimensional Metal Nanostructures: From Colloidal Syntheses to Applications. *Chem. Rev.* **2019**, *119* (15), 8972-9073.
 20. Xia, Y.; Xia, X.; Peng, H.-C., Shape-Controlled Synthesis of Colloidal Metal Nanocrystals: Thermodynamic versus Kinetic Products. *J. Am. Chem. Soc.* **2015**, *137* (25), 7947-7966.
 21. Xia, Y.; Xiong, Y.; Lim, B.; Skrabalak, S. E., Shape-Controlled Synthesis of Metal Nanocrystals: Simple Chemistry Meets Complex Physics? *Angew. Chem. Int. Ed.* **2009**, *48* (1), 60-103.
 22. Zeng, J.; Zheng, Y.; Rycenga, M.; Tao, J.; Li, Z.-Y.; Zhang, Q.; Zhu, Y.; Xia, Y., Controlling the Shapes of Silver Nanocrystals with Different Capping Agents. *J. Am. Chem. Soc.* **2010**, *132* (25), 8552-8553.

23. Yang, T.-H.; Shi, Y.; Janssen, A.; Xia, Y., Surface Capping Agents and Their Roles in Shape-Controlled Synthesis of Colloidal Metal Nanocrystals. *Angew. Chem. Int. Ed.* **2019**.
24. Zhao, S.; Han, F.; Li, J.; Meng, X.; Huang, W.; Cao, D.; Zhang, G.; Sun, R.; Wong, C. P., Advancements in Copper Nanowires: Synthesis, Purification, Assemblies, Surface Modification, and Applications. *Small* **2018**, *14* (26).
25. Li, N.; Yin, H.; Zhuo, X.; Yang, B.; Zhu, X.-M.; Wang, J., Infrared-Responsive Colloidal Silver Nanorods for Surface-Enhanced Infrared Absorption. *Advanced Optical Materials* **2018**, *6* (17), 1800436.
26. Dionne, J. A., Plasmons rock in metal bands. *Nature Materials* **2013**, *12*, 380.
27. Saha, K.; Agasti, S. S.; Kim, C.; Li, X.; Rotello, V. M., Gold Nanoparticles in Chemical and Biological Sensing. *Chem. Rev.* **2012**, *112* (5), 2739-2779.
28. Doering, W. E.; Piotti, M. E.; Natan, M. J.; Freeman, R. G., SERS as a Foundation for Nanoscale, Optically Detected Biological Labels. *Adv. Mater.* **2007**, *19* (20), 3100-3108.
29. Zhang, Q.; Zhou, Y.; Villarreal, E.; Lin, Y.; Zou, S.; Wang, H., Faceted Gold Nanorods: Nanocuboids, Convex Nanocuboids, and Concave Nanocuboids. *Nano Lett.* **2015**, *15* (6), 4161-4169.
30. Jia, H.; Fang, C.; Zhu, X.-M.; Ruan, Q.; Wang, Y.-X. J.; Wang, J., Synthesis of Absorption-Dominant Small Gold Nanorods and Their Plasmonic Properties. *Langmuir* **2015**, *31* (26), 7418-7426.
31. He, X.; Liu, A. I.; Hu, X.; Song, M.; Duan, F.; Lan, Q.; Xiao, J.; Liu, J.; Zhang, M.; Chen, Y.; Zeng, Q., Temperature-controlled transparent-film heater based on silver nanowire-PMMA composite film. *Nanotechnology* **2016**, *27* (47), 475709.
32. Celle, C.; Mayousse, C.; Moreau, E.; Basti, H.; Carella, A.; Simonato, J.-P., Highly flexible transparent film heaters based on random networks of silver nanowires. *Nano Research* **2012**, *5* (6), 427-433.
33. *U.S. Geological Survey*. U.S. Department of the Interior: Washington, D.C.: 2014; p 48-49.
34. Gutowski, T. G.; Sahni, S.; Allwood, J. M.; Ashby, M. F.; Worrell, E., The energy required to produce materials: constraints on energy-intensity improvements,

- parameters of demand. *Philosophical Transactions of the Royal Society A: Mathematical, Physical and Engineering Sciences* **2013**, 371 (1986), 20120003.
35. Choi, H.; Park, S.-H., Seedless Growth of Free-Standing Copper Nanowires by Chemical Vapor Deposition. *J. Am. Chem. Soc.* **2004**, 126 (20), 6248-6249.
 36. Gerein, N. J.; Haber, J. A., Effect of ac Electrodeposition Conditions on the Growth of High Aspect Ratio Copper Nanowires in Porous Aluminum Oxide Templates. *The Journal of Physical Chemistry B* **2005**, 109 (37), 17372-17385.
 37. Wu, H.; Hu, L.; Rowell, M. W.; Kong, D.; Cha, J. J.; McDonough, J. R.; Zhu, J.; Yang, Y.; McGehee, M. D.; Cui, Y., Electrospun Metal Nanofiber Webs as High-Performance Transparent Electrode. *Nano Lett.* **2010**, 10 (10), 4242-4248.
 38. Liu, Z.; Yang, Y.; Liang, J.; Hu, Z.; Li, S.; Peng, S.; Qian, Y., Synthesis of Copper Nanowires via a Complex-Surfactant-Assisted Hydrothermal Reduction Process. *The Journal of Physical Chemistry B* **2003**, 107 (46), 12658-12661.
 39. Chang, Y.; Lye, M. L.; Zeng, H. C., Large-Scale Synthesis of High-Quality Ultralong Copper Nanowires. *Langmuir* **2005**, 21 (9), 3746-3748.
 40. Rathmell, A. R.; Bergin, S. M.; Hua, Y.-L.; Li, Z.-Y.; Wiley, B. J., The Growth Mechanism of Copper Nanowires and Their Properties in Flexible, Transparent Conducting Films. *Adv. Mater.* **2010**, 22 (32), 3558-3563.
 41. Jin, M.; He, G.; Zhang, H.; Zeng, J.; Xie, Z.; Xia, Y., Shape-Controlled Synthesis of Copper Nanocrystals in an Aqueous Solution with Glucose as a Reducing Agent and Hexadecylamine as a Capping Agent. *Angew. Chem. Int. Ed.* **2011**, 50 (45), 10560-10564.
 42. Liu, Z.; Chen, Y.; Zheng, Y., Stirring-induced growth of hierarchical Cu structures in the presence of diamine. *CrystEngComm* **2014**, 16 (38), 9054-9062.
 43. Chen, J.; Chen, J.; Li, Y.; Zhou, W.; Feng, X.; Huang, Q.; Zheng, J.-G.; Liu, R.; Ma, Y.; Huang, W., Enhanced oxidation-resistant Cu–Ni core–shell nanowires: controllable one-pot synthesis and solution processing to transparent flexible heaters. *Nanoscale* **2015**, 7 (40), 16874-16879.
 44. Kim, M. J.; Alvarez, S.; Yan, T.; Tadepalli, V.; Fichthorn, K. A.; Wiley, B. J., Modulating the Growth Rate, Aspect Ratio, and Yield of Copper Nanowires with Alkylamines. *Chem. Mater.* **2018**, 30 (8), 2809-2818.

45. Ravi Kumar, D. V.; Kim, I.; Zhong, Z.; Kim, K.; Lee, D.; Moon, J., Cu(ii)-alkyl amine complex mediated hydrothermal synthesis of Cu nanowires: exploring the dual role of alkyl amines. *PCCP* **2014**, *16* (40), 22107-22115.
46. Mohl, M.; Pusztai, P.; Kukovecz, A.; Konya, Z.; Kukkola, J.; Kordas, K.; Vajtai, R.; Ajayan, P. M., Low-Temperature Large-Scale Synthesis and Electrical Testing of Ultralong Copper Nanowires. *Langmuir* **2010**, *26* (21), 16496-16502.
47. Kim, M. J.; Alvarez, S.; Chen, Z.; Fichthorn, K. A.; Wiley, B. J., Single-Crystal Electrochemistry Reveals Why Metal Nanowires Grow. *J. Am. Chem. Soc.* **2018**, *140* (44), 14740-14746.
48. Cruz, M. A.; Ye, S.; Kim, M. J.; Reyes, C.; Yang, F.; Flowers, P. F.; Wiley, B. J., Multigram Synthesis of Cu-Ag Core-Shell Nanowires Enables the Production of a Highly Conductive Polymer Filament for 3D Printing Electronics. *Particle & Particle Systems Characterization* **2018**, *35* (5), 1700385.
49. Koo, J.; Kwon, S.; Kim, N. R.; Shin, K.; Lee, H. M., Ethylenediamine-Enhanced Oxidation Resistivity of a Copper Surface during Water-Based Copper Nanowire Synthesis. *The Journal of Physical Chemistry C* **2016**, *120* (6), 3334-3340.
50. Kim, M. J.; Flowers, P. F.; Stewart, I. E.; Ye, S.; Baek, S.; Kim, J. J.; Wiley, B. J., Ethylenediamine Promotes Cu Nanowire Growth by Inhibiting Oxidation of Cu(111). *J. Am. Chem. Soc.* **2017**, *139* (1), 277-284.
51. Rathmell, A. R.; Wiley, B. J., The Synthesis and Coating of Long, Thin Copper Nanowires to Make Flexible, Transparent Conducting Films on Plastic Substrates. *Adv. Mater.* **2011**, *23* (41), 4798-4803.
52. Stewart, I. E.; Rathmell, A. R.; Yan, L.; Ye, S.; Flowers, P. F.; You, W.; Wiley, B. J., Solution-processed copper-nickel nanowire anodes for organic solar cells. *Nanoscale* **2014**, *6* (11), 5980-8.
53. Stewart, I. E.; Ye, S.; Chen, Z.; Flowers, P. F.; Wiley, B. J., Synthesis of Cu-Ag, Cu-Au, and Cu-Pt Core-Shell Nanowires and Their Use in Transparent Conducting Films. *Chem. Mater.* **2015**, *27* (22), 7788-7794.
54. Kholmanov, I.; Domingues, S. H.; Chou, H.; Wang, X.; Tan, C.; Kim, J.; Li, H.; Piner, R.; Zabin, A.; Ruoff, R., Reduced Graphene Oxide/Copper Nanowire Hybrid Films as High-Performance Transparent Electrodes. *ACS Nano* **2013**, *7* (2), 1811-1816.

55. Im, H.; Jung, S.; Jin, J.; Lee, D.; Lee, J.; Lee, D.; Lee, J.; Kim, I.; Bae, B., Flexible Transparent Conducting Hybrid Film Using a Surface- Embedded Copper Nanowire Network: A Highly Oxidation-Resistant Copper Nanowire Electrode for Flexible Optoelectronics. *ACS Nano* **2014**, *8* (10), 10973-10979.
56. Lee, J.-W.; Han, J.; Lee, D. S.; Bae, S.; Lee, S. H.; Lee, S.-K.; Moon, B. J.; Choi, C.-J.; Wang, G.; Kim, T.-W., 2D Single-Crystalline Copper Nanoplates as a Conductive Filler for Electronic Ink Applications. *Small* **2018**, *14* (8), 1703312.
57. Sun, Y.; Xu, L.; Yin, Z.; Song, X., Synthesis of copper submicro/nanoplates with high stability and their recyclable superior catalytic activity towards 4-nitrophenol reduction. *Journal of Materials Chemistry A* **2013**, *1* (39), 12361-12370.
58. Luc, W.; Fu, X.; Shi, J.; Lv, J.-J.; Jouny, M.; Ko, B. H.; Xu, Y.; Tu, Q.; Hu, X.; Wu, J.; Yue, Q.; Liu, Y.; Jiao, F.; Kang, Y., Two-dimensional copper nanosheets for electrochemical reduction of carbon monoxide to acetate. *Nature Catalysis* **2019**, *2* (5), 423-430.
59. Dai, L.; Qin, Q.; Wang, P.; Zhao, X.; Hu, C.; Liu, P.; Qin, R.; Chen, M.; Ou, D.; Xu, C.; Mo, S.; Wu, B.; Fu, G.; Zhang, P.; Zheng, N., Ultrastable atomic copper nanosheets for selective electrochemical reduction of carbon dioxide. *Science Advances* **2017**, *3* (9), e1701069.
60. Venkatasubramanian, R.; He, J.; Johnson, M. W.; Stern, I.; Kim, D. H.; Pesika, N. S., Additive-Mediated Electrochemical Synthesis of Platelike Copper Crystals for Methanol Electrooxidation. *Langmuir* **2013**, *29* (43), 13135-13139.
61. Bhanushali, S.; Ghosh, P.; Ganesh, A.; Cheng, W., 1D copper nanostructures: progress, challenges and opportunities. *Small* **2015**, *11* (11), 1232-52.
62. Ha, T. H.; Koo, H.-J.; Chung, B. H., Shape-Controlled Syntheses of Gold Nanoprisms and Nanorods Influenced by Specific Adsorption of Halide Ions. *The Journal of Physical Chemistry C* **2007**, *111* (3), 1123-1130.
63. Bindra, P.; Light, D.; Rath, D., Mechanisms of electroless metal plating: I. Mixed potential theory and the interdependence of partial reactions. *IBM Journal of Research and Development* **1984**, *28* (6), 668-678.
64. Bindra, P.; Roldan, J., Mechanisms of electroless metal plating. III. Mixed potential theory and the interdependence of partial reactions. *J. Appl. Electrochem.* **1987**, *17* (6), 1254-1266.

65. Feldman, B. J.; Melroy, O. R., The Mechanism of Electroless Cu Deposition: Extraction of the Oxidative and Reductive Electrochemical Half-Cell Currents from a Complete Bath. *J. Electrochem. Soc.* **1989**, *136* (3), 640-643.
66. Bard, A. J.; Faulkner, L. R., *Electrochemical Methods: Fundamentals and Applications, 2nd Edition*. John Wiley & Sons: New York, 2001.
67. Dubin, V. M.; Shacham-Diamand, Y.; Zhao, B.; Vasudev, P. K.; Ting, C. H., Selective and Blanket Electroless Copper Deposition for Ultralarge Scale Integration. *J. Electrochem. Soc.* **1997**, *144* (3), 898-908.
68. Kim, M. J.; Seo, Y.; Cruz, M. A.; Wiley, B. J., Metal Nanowire Felt as a Flow-Through Electrode for High-Productivity Electrochemistry. *ACS Nano* **2019**, *13* (6), 6998-7009.
69. Catenacci, M. J.; Reyes, C.; Cruz, M. A.; Wiley, B. J., Stretchable Conductive Composites from Cu–Ag Nanowire Felt. *ACS Nano* **2018**, *12* (4), 3689-3698.
70. Mardiansyah, D.; Triyana, K.; Sosiati, H.; Harsojo, Synthesis of copper nanorods by aqueous solution method without heating external. 2016.
71. Ye, S.; Rathmell, A. R.; Ha, Y. C.; Wilson, A. R.; Wiley, B. J., The role of cuprous oxide seeds in the one-pot and seeded syntheses of copper nanowires. *Small* **2014**, *10* (9), 1771-8.
72. Ye, S.; Stewart, I. E.; Chen, Z.; Li, B.; Rathmell, A. R.; Wiley, B. J., How Copper Nanowires Grow and How To Control Their Properties. *Acc. Chem. Res.* **2016**, *49* (3), 442-51.
73. Panigrahi, S.; Kundu, S.; Ghosh, S. K.; Nath, S.; Praharaj, S.; Basu, S.; Pal, T., Selective one-pot synthesis of copper nanorods under surfactantless condition. *Polyhedron* **2006**, *25* (5), 1263-1269.
74. Kevin, M.; Lim, G. Y. R.; Ho, G. W., Facile control of copper nanowire dimensions via the Maillard reaction: using food chemistry for fabricating large-scale transparent flexible conductors. *Green Chem.* **2015**, *17*, 1120-1126.
75. Hendricks, B. C.; Steinbach, W. H., The Thermal Chemistry of d-Glucose and Other Glucose Sugards in Sodium Hydroxide Solutions. *J. Phys. Chem.* **1937**, *42* (3), 335-342.
76. Yang, B. Y.; Montgomery, R., Alkaline degradation of glucose: effect of initial concentration of reactants. *Carbohydr. Res.* **1996**, *280* (1), 27-45.

77. Wilde, C. P.; Zhang, M., Oxidation of glucose at electrodeposited platinum electrodes in alkaline solution. *J. Chem. Soc., Faraday Trans.* **1993**, 89 (2), 385-389.
78. Yei, L. H. E.; Beden, B.; Lamy, C., Electrocatalytic oxidation of glucose at platinum in alkaline medium: on the role of temperature. *Journal of Electroanalytical Chemistry and Interfacial Electrochemistry* **1988**, 246 (2), 349-362.
79. Christenson, K. K.; Paulsen, J. A.; Renn, M. J.; McDonald, K.; Bourassa, J., Direct Printing of Circuit Boards Using Aerosol Jet®. *NIP & Digital Fabrication Conference* **2011**, (2), 433-436.
80. Espalin, D.; Muse, D. W.; MacDonald, E.; Wicker, R. B., 3D Printing multifunctionality: structures with electronics. *The International Journal of Advanced Manufacturing Technology* **2014**, 72 (5-8), 963-978.
81. Liang, J.; Li, L.; Chen, D.; Hajagos, T.; Ren, Z.; Chou, S.-Y.; Hu, W.; Pei, Q., Intrinsically stretchable and transparent thin-film transistors based on printable silver nanowires, carbon nanotubes and an elastomeric dielectric. **2015**, 6, 7647.
82. Liang, J.; Tong, K.; Pei, Q., A Water-Based Silver-Nanowire Screen-Print Ink for the Fabrication of Stretchable Conductors and Wearable Thin-Film Transistors. *Adv. Mater.* **2016**, 28 (28), 5986-5996.
83. Lipomi, D. J.; Bao, Z., Stretchable, elastic materials and devices for solar energy conversion. *Energy Environ. Sci.* **2011**, 4 (9), 3314-3328.
84. Lipomi, D. J.; Vosgueritchian, M.; Tee, B. C. K.; Hellstrom, S. L.; Lee, J. A.; Fox, C. H.; Bao, Z., Skin-like pressure and strain sensors based on transparent elastic films of carbon nanotubes. *Nat Nano* **2011**, 6 (12), 788-792.
85. MacDonald, E.; Wicker, R., Multiprocess 3D printing for increasing component functionality. *Science* **2016**, 353 (6307).
86. Mannsfeld, S. C. B.; Tee, B. C. K.; Stoltenberg, R. M.; Chen, C. V. H. H.; Barman, S.; Muir, B. V. O.; Sokolov, A. N.; Reese, C.; Bao, Z., Highly sensitive flexible pressure sensors with microstructured rubber dielectric layers. *Nat Mater* **2010**, 9 (10), 859-864.
87. Parekh, D. P.; Cormier, D.; Dickey, M. D., Multifunctional Printing: Incorporating Electronics into 3D Parts Made by Additive Manufacturing. In *Addit. Manuf.*, Bandyopadhyay, A.; Bose, S., Eds. CRC Press: 2015; pp 215-258.

88. Rogers, J. A.; Bao, Z., Printed plastic electronics and paperlike displays. *J. Polym. Sci., Part A: Polym. Chem.* **2002**, *40* (20), 3327-3334.
89. Rogers, J. A.; Someya, T.; Huang, Y., Materials and Mechanics for Stretchable Electronics. *Science* **2010**, *327* (5973), 1603-1607.
90. Shemelya, C.; Banuelos-Chacon, L.; Melendez, A.; Kief, C.; Espalin, D.; Wicker, R.; Krijnen, G.; Macdonald, E., Multi-functional 3D printed and embedded sensors for satellite qualification structures. In *Sensors*, Busan, 2015; pp 1-4.
91. Ankireddy, K.; Iskander, M.; Vunnam, S.; Anagnostou, D. E.; Kellar, J.; Cross, W., Thermal analysis of silver nanoparticles for flexible printed antenna fabrication. *J. Appl. Phys.* **2013**, *114* (12), 124303.
92. Bao, Z.; Feng, Y.; Dodabalapur, A.; Raju, V. R.; Lovinger, A. J., High-Performance Plastic Transistors Fabricated by Printing Techniques. *Chem. Mater.* **1997**, *9* (6), 1299-1301.
93. Berggren, M.; Nilsson, D.; Robinson, N. D., Organic materials for printed electronics. *Nat Mater* **2007**, *6* (1), 3-5.
94. Finkensteller, K., The Manufacture of Transponders and Contactless Smart Cards. In *RFID Handbook*, John Wiley & Sons, Ltd: 2010; pp 347-359.
95. Kamyshny, A.; Magdassi, S., Conductive Nanomaterials for Printed Electronics. *Small* **2014**, *10* (17), 3515-3535.
96. Shin, K.-Y.; Hong, J.-Y.; Jang, J., Micropatterning of Graphene Sheets by Inkjet Printing and Its Wideband Dipole-Antenna Application. *Adv. Mater.* **2011**, *23* (18), 2113-2118.
97. Siegel, A. C.; Phillips, S. T.; Dickey, M. D.; Lu, N.; Suo, Z.; Whitesides, G. M., Foldable Printed Circuit Boards on Paper Substrates. *Adv. Funct. Mater.* **2010**, *20* (1), 28-35.
98. Subramanian, V.; Chang, P. C.; Huang, D.; Lee, J. B.; Molesa, S. E.; Redinger, D. R.; Volkman, S. K., All-printed RFID tags: materials, devices, and circuit implications. In *19th International Conference on VLSI Design*, IEEE: Hyderabad, India, 2006.
99. Subramanian, V.; Lee, J. B.; Liu, V. H.; Molesa, S., Printed Electronic Nose Vapor Sensors for Consumer Product Monitoring. In *International Solid State Circuits Conference*, IEEE: San Francisco, CA, USA, 2006.

100. Carlson, A.; Bowen, A. M.; Huang, Y.; Nuzzo, R. G.; Rogers, J. A., Transfer Printing Techniques for Materials Assembly and Micro/Nanodevice Fabrication. *Adv. Mater.* **2012**, *24* (39), 5284-5318.
101. Kim, D.-H.; Ghaffari, R.; Lu, N.; Rogers, J. A., Flexible and Stretchable Electronics for Biointegrated Devices. *Annu. Rev. Biomed. Eng.* **2012**, *14* (1), 113-128.
102. Nuzzo, R. G.; Rogers, J. A.; Menard, E.; Lee, K. J.; Khang, D. Y.; Sun, Y.; Meitl, M.; Zhu, Z., Methods and devices for fabricating and assembling printable semiconductor elements. Google Patents: 2016.
103. Rim, Y. S.; Bae, S. H.; Chen, H.; De Marco, N.; Yang, Y., Recent Progress in Materials and Devices toward Printable and Flexible Sensors. *Adv. Mater.* **2016**, *28* (22), 4415-40.
104. Xu, S.; Zhang, Y.; Jia, L.; Mathewson, K. E.; Jang, K. I.; Kim, J.; Fu, H.; Huang, X.; Chava, P.; Wang, R.; Bhole, S.; Wang, L.; Na, Y. J.; Guan, Y.; Flavin, M.; Han, Z.; Huang, Y.; Rogers, J. A., Soft microfluidic assemblies of sensors, circuits, and radios for the skin. *Science* **2014**, *344* (6179), 70-4.
105. Catenacci, M. J.; Flowers, P. F.; Cao, C.; Andrews, J. B.; Franklin, A. D.; Wiley, B. J., Fully Printed Memristors from Cu-SiO₂ Core-Shell Nanowire Composites. *J. Electron. Mater.* **2017**, *46* (7), 4596-4603.
106. Chizari, K.; Daoud, M. A.; Ravindran, A. R.; Therriault, D., 3D Printing of Highly Conductive Nanocomposites for the Functional Optimization of Liquid Sensors. *Small* **2016**, *12* (44), 6076-6082.
107. Flowers, P. F.; Reyes, C.; Ye, S.; Kim, M. J.; Wiley, B. J., 3D printing electronic components and circuits with conductive thermoplastic filament. *Addit. Manuf.* **2017**, *18* (Supplement C), 156-163.
108. Xie, Y.; Ye, S.; Reyes, C.; Sithikong, P.; Popa, B.; Wiley, B. J.; Cummer, S. A., Microwave metamaterials made by fused deposition 3D printing of a highly conductive copper-based filament. *Appl. Phys. Lett.* **2017**, *110* (18), 181903.
109. Li, J.; Wasley, T.; Nguyen, T. T.; Ta, V. D.; Shephard, J. D.; Stringer, J.; Smith, P.; Esenturk, E.; Connaughton, C.; Kay, R., Hybrid additive manufacturing of 3D electronic systems. *J. Micromech. Microeng.* **2016**, *26* (10).
110. Sculpteo *The State of 3D Printing*; 2017.

111. Jo, A.; Chae, H.; Kim, Y.; Kim, H.; Paek, S.; Soum, V.; Jang, W.; Ryu, S.; Kwon, O.; Shin, K., Formulation of Conductive Filament Composed of Thermoplastic with Carbon Black for a Simple 3D Printing Electrical Device. *J. Nanosci. Nanotechnol.* **2016**, *16*, 8415-8418.
112. Leigh, S. J.; Bradley, R. J.; Pursell, C. P.; Billson, D. R.; Hutchins, D. A., A simple, low-cost conductive composite material for 3D printing of electronic sensors. *PLoS One* **2012**, *7* (11), e49365.
113. Zhang, D.; Chi, B.; Li, B.; Gao, Z.; Du, Y.; Guo, J.; Wei, J., Fabrication of highly conductive graphene flexible circuits by 3D printing. *Synth. Met.* **2016**, *217*, 79-86.
114. de la Osa, G.; Pérez-Coll, D.; Miranzo, P.; Osendi, M. I.; Belmonte, M., Printing of Graphene Nanoplatelets into Highly Electrically Conductive Three-Dimensional Porous Macrostructures. *Chem. Mater.* **2016**, *28* (17), 6321-6328.
115. Multi3D 100g Electrifi Conductive 3D Printing Filament. <https://www.multi3dllc.com/product/electrifi-3d-printing-filament/> (accessed Mar 1, 2017).
116. Proto-Pasta Electrically Conductive Composite PLA. <https://www.proto-pasta.com/collections/exotic-composite-pla/products/conductive-pla?variant=27767315720>.
117. BlackMagic3D Conductive Graphene PLA Filament 100g. <http://www.blackmagic3d.com/Conductive-p/grphn-pla.htm>.
118. Multi3D Electrifi Conductive Filament. <https://www.multi3dllc.com/product/electrifi/>.
119. Balberg, I.; Anderson, C. H.; Alexander, S.; Wagner, N., Excluded volume and its relation to the onset of percolation. *Phys. Rev. B* **1984**, *30* (7), 3933-3943.
120. Balberg, I.; Binenbaum, N.; Wagner, N., Percolation Thresholds in the Three-Dimensional Sticks System. *Phys. Rev. Lett.* **1984**, *52* (17), 1465-1468.
121. Bug, A. L. R.; Safran, S. A.; Webman, I., Continuum Percolation of Rods. *Phys. Rev. Lett.* **1985**, *54* (13), 1412-1415.
122. Bug, A. L. R.; Safran, S. A.; Webman, I., Continuum percolation of permeable objects. *Phys. Rev. B* **1986**, *33* (7), 4716-4724.

123. White, S. I.; Mutiso, R. M.; Vora, P. M.; Jahnke, D.; Hsu, S.; Kikkawa, J. M.; Li, J.; Fischer, J. E.; Winey, K. I., Electrical Percolation Behavior in Silver Nanowire-Polystyrene Composites: Simulation and Experiment. *Adv. Funct. Mater.* **2010**, *20* (16), 2709-2716.
124. Ning, H.; Zen, M.; Cheng, Y.; Go, Y.; Hisao, F.; Toshiyuki, H., The electrical properties of polymer nanocomposites with carbon nanotube fillers. *Nanotechnology* **2008**, *19* (21), 215701.
125. Park, J. S.; Kim, T.; Kim, W. S., Conductive Cellulose Composites with Low Percolation Threshold for 3D Printed Electronics. *Sci. Rep.* **2017**, *7* (1), 3246.
126. Russ, M.; Rahatekar, S. S.; Koziol, K.; Farmer, B.; Peng, H. X., Length-dependent electrical and thermal properties of carbon nanotube-loaded epoxy nanocomposites. *Compos. Sci. Technol.* **2013**, *81*, 42-47.
127. Woodruff, M. A.; Hutmacher, D. W., The return of a forgotten polymer—Polycaprolactone in the 21st century. *Prog. Polym. Sci.* **2010**, *35* (10), 1217-1256.
128. Borchert, J. W.; Stewart, I. E.; Ye, S.; Rathmell, A. R.; Wiley, B. J.; Winey, K. I., Effects of length dispersity and film fabrication on the sheet resistance of copper nanowire transparent conductors. *Nanoscale* **2015**, *7* (34), 14496-504.
129. Tozzi, E. J.; Klingenberg, D. J.; Scott, T., Correlation of fiber shape measures with dilute suspension properties. *Nord. Pulp Pap. Res. J.* **2008**, *23* (4), 369-373.
130. Utracki, L. A.; Fisa, B., Rheology of fiber- or flake-filled plastics. *Polym. Compos.* **1982**, *3* (4), 193-211.
131. Wheeler, H. A., Simple Inductance Formulas for Radio Coils. *Proc. IRE* **1928**, *16*, 1398-1400.
132. Chien, A.-T.; Cho, S.; Joshi, Y.; Kumar, S., Electrical conductivity and Joule heating of polyacrylonitrile/carbon nanotube composite fibers. *Polymer* **2014**, *55* (26), 6896-6905.
133. Bhanushali, S.; Ghosh, P. C.; Simon, G. P.; Cheng, W., Copper Nanowire-Filled Soft Elastomer Composites for Applications as Thermal Interface Materials. *Adv. Mater. Interfaces* **2017**, *4* (17), 1700387-n/a.

134. Wang, S.; Cheng, Y.; Wang, R.; Sun, J.; Gao, L., Highly Thermal Conductive Copper Nanowire Composites with Ultralow Loading: Toward Applications as Thermal Interface Materials. *ACS Appl. Mater. Interfaces* **2014**, *6* (9), 6481-6486.
135. Arie, M. A.; Shooshtari, A. H.; Tiwari, R.; Dessiatoun, S. V.; Ohadi, M. M.; Pearce, J. M., Experimental characterization of heat transfer in an additively manufactured polymer heat exchanger. *Appl. Therm. Eng.* **2017**, *113*, 575-584.
136. Sekitani, T.; Nakajima, H.; Maeda, H.; Fukushima, T.; Aida, T.; Hata, K.; Someya, T., Stretchable active-matrix organic light-emitting diode display using printable elastic conductors. *Nature Materials* **2009**, *8*, 494.
137. Yamada, T.; Hayamizu, Y.; Yamamoto, Y.; Yomogida, Y.; Izadi-Najafabadi, A.; Futaba, D. N.; Hata, K., A stretchable carbon nanotube strain sensor for human-motion detection. *Nature nanotechnology* **2011**, *6* (5), 296-301.
138. Yan, C.; Wang, J.; Kang, W.; Cui, M.; Wang, X.; Foo, C. Y.; Chee, K. J.; Lee, P. S., Highly Stretchable Piezoresistive Graphene–Nanocellulose Nanopaper for Strain Sensors. *Adv. Mater.* **2014**, *26* (13), 2022-2027.
139. Hong, S.; Lee, H.; Lee, J.; Kwon, J.; Han, S.; Suh, Y. D.; Cho, H.; Shin, J.; Yeo, J.; Ko, S. H., Highly Stretchable and Transparent Metal Nanowire Heater for Wearable Electronics Applications. *Adv. Mater.* **2015**, *27* (32), 4744-4751.
140. Joshipura, I. D.; Finn, M.; Tan, S. T. M.; Dickey, M. D.; Lipomi, D. J., Stretchable bioelectronics—Current and future. *MRS Bull.* **2017**, *42* (12), 960-967.
141. Xu, S.; Zhang, Y.; Cho, J.; Lee, J.; Huang, X.; Jia, L.; Fan, J. A.; Su, Y.; Su, J.; Zhang, H.; Cheng, H.; Lu, B.; Yu, C.; Chuang, C.; Kim, T.-i.; Song, T.; Shigeta, K.; Kang, S.; Dagdeviren, C.; Petrov, I.; Braun, P. V.; Huang, Y.; Paik, U.; Rogers, J. A., Stretchable batteries with self-similar serpentine interconnects and integrated wireless recharging systems. *Nature Communications* **2013**, *4* (1), 1543.
142. Matsuhisa, N.; Kaltenbrunner, M.; Yokota, T.; Jinno, H.; Kuribara, K.; Sekitani, T.; Someya, T., Printable elastic conductors with a high conductivity for electronic textile applications. *Nature Communications* **2015**, *6* (1), 7461.
143. Matsuhisa, N.; Inoue, D.; Zalar, P.; Jin, H.; Matsuba, Y.; Itoh, A.; Yokota, T.; Hashizume, D.; Someya, T., Printable elastic conductors by in situ formation of silver nanoparticles from silver flakes. *Nature Materials* **2017**, *16*, 834.

144. Oh, Y.; Yoon, I. S.; Lee, C.; Kim, S. H.; Ju, B.-K.; Hong, J.-M., Selective photonic sintering of Ag flakes embedded in silicone elastomers to fabricate stretchable conductors. *Journal of Materials Chemistry C* **2017**, *5* (45), 11733-11740.
145. Huang, W.; Li, J.; Zhao, S.; Han, F.; Zhang, G.; Sun, R.; Wong, C.-P., Highly electrically conductive and stretchable copper nanowires-based composite for flexible and printable electronics. *Compos. Sci. Technol.* **2017**, *146*, 169-176.
146. Roberts, R.; Ouellette, R. P.; Cheremisinoff, P. N., *Industrial applications of electroorganic synthesis*. Ann Arbor Science: 1982.
147. Ye, S.; Rathmell, A. R.; Chen, Z.; Stewart, I. E.; Wiley, B. J., Metal Nanowire Networks: The Next Generation of Transparent Conductors. *Adv. Mater.* **2014**, *26* (39), 6670-6687.
148. Gawande, M. B.; Goswami, A.; Felpin, F.-X.; Asefa, T.; Huang, X.; Silva, R.; Zou, X.; Zboril, R.; Varma, R. S., Cu and Cu-Based Nanoparticles: Synthesis and Applications in Catalysis. *Chem. Rev.* **2016**, *116* (6), 3722-3811.
149. Yanson, Y. I.; Rost, M. J., Structural Accelerating Effect of Chloride on Copper Electrodeposition. *Angew. Chem. Int. Ed.* **2013**, *52* (9), 2454-2458.
150. Sung, M.; Yoon, Y.; Hong, J.; Kim, M. J.; Kim, J. J., Bromide Ion as a Leveler for High-Speed TSV Filling. *J. Electrochem. Soc.* **2019**, *166* (13), D546-D550.
151. Kim, M. J.; Kim, H. C.; Kim, J. J., The Influences of Iodide Ion on Cu Electrodeposition and TSV Filling. *J. Electrochem. Soc.* **2016**, *163* (8), D434-D441.
152. Aherne, D.; Ledwith, D. M.; Gara, M.; Kelly, J. M., Optical Properties and Growth Aspects of Silver Nanoprisms Produced by a Highly Reproducible and Rapid Synthesis at Room Temperature. *Adv. Funct. Mater.* **2008**, *18* (14), 2005-2016.
153. Goebel, J.; Zhang, Q.; He, L.; Yin, Y., Monitoring the Shape Evolution of Silver Nanoplates: A Marker Study. *Angew. Chem. Int. Ed.* **2012**, *51* (2), 552-555.
154. Kim, M. H.; Kwak, S. K.; Im, S. H.; Lee, J.-B.; Choi, K.-Y.; Byun, D.-J., Maneuvering the growth of silver nanoplates: use of halide ions to promote vertical growth. *Journal of Materials Chemistry C* **2014**, *2* (30), 6165-6170.
155. Germain, V.; Li, J.; Inger, D.; Wang, Z. L.; Pileni, M. P., Stacking Faults in Formation of Silver Nanodisks. *The Journal of Physical Chemistry B* **2003**, *107* (34), 8717-8720.

156. Xiong, Y.; Siekkinen, A. R.; Wang, J.; Yin, Y.; Kim, M. J.; Xia, Y., Synthesis of silver nanoplates at high yields by slowing down the polyol reduction of silver nitrate with polyacrylamide. *J. Mater. Chem.* **2007**, *17* (25), 2600-2602.
157. Zeng, J.; Xia, X.; Rycenga, M.; Henneghan, P.; Li, Q.; Xia, Y., Successive Deposition of Silver on Silver Nanoplates: Lateral versus Vertical Growth. *Angew. Chem. Int. Ed.* **2011**, *50* (1), 244-249.
158. Xiong, Y.; McLellan, J. M.; Chen, J.; Yin, Y.; Li, Z.-Y.; Xia, Y., Kinetically Controlled Synthesis of Triangular and Hexagonal Nanoplates of Palladium and Their SPR/SERS Properties. *J. Am. Chem. Soc.* **2005**, *127* (48), 17118-17127.
159. Xiong, Y.; Washio, I.; Chen, J.; Cai, H.; Li, Z.-Y.; Xia, Y., Poly(vinyl pyrrolidone): A Dual Functional Reductant and Stabilizer for the Facile Synthesis of Noble Metal Nanoplates in Aqueous Solutions. *Langmuir* **2006**, *22* (20), 8563-8570.
160. Lim, B.; Camargo, P. H. C.; Xia, Y., Mechanistic Study of the Synthesis of Au Nanotadpoles, Nanokites, and Microplates by Reducing Aqueous HAuCl₄ with Poly(vinyl pyrrolidone). *Langmuir* **2008**, *24* (18), 10437-10442.
161. Guo, H.; Chen, Y.; Ping, H.; Wang, L.; Peng, D.-L., One-pot synthesis of hexagonal and triangular nickel-copper alloy nanoplates and their magnetic and catalytic properties. *J. Mater. Chem.* **2012**, *22* (17), 8336-8344.
162. Huemann, S.; Minh Hai, N. T.; Broekmann, P.; Wandelt, K.; Zajonz, H.; Dosch, H.; Renner, F., X-ray Diffraction and STM Study of Reactive Surfaces under Electrochemical Control: Cl and I on Cu(100). *The Journal of Physical Chemistry B* **2006**, *110* (49), 24955-24963.
163. Bergin, S. M.; Chen, Y.-H.; Rathmell, A. R.; Charbonneau, P.; Li, Z.-Y.; Wiley, B. J., The effect of nanowire length and diameter on the properties of transparent, conducting nanowire films. *Nanoscale* **2012**, *4* (6), 1996-2004.
164. Stewart, I. E.; Kim, M. J.; Wiley, B. J., Effect of Morphology on the Electrical Resistivity of Silver Nanostructure Films. *ACS Appl. Mater. Interfaces* **2017**, *9* (2), 1870-1876.

Biography

Mutya Aguila Cruz graduated from Rollins College in 2015 with a Bachelor of Arts in chemistry. She wrote an undergraduate thesis entitled “Synthesis of Photoactive Gold Nanoparticles for Photodynamic Therapy.” She also published her first research article “Improved Butanol–Methanol (BUME) Method by Replacing Acetic Acid for Lipid Extraction of Biological Samples” as an undergraduate research intern in Dr. Xianlin Han’s lab at the Sanford Burnham Prebys Medical Discovery Institute.

In 2015, she pursued her doctorate degree in chemistry at Duke University under the supervision of Dr. Benjamin Wiley. During her graduate career, she published two first-authored papers entitled “Multigram Synthesis of Cu-Ag Core-Shell Nanowires Enables the Production of Highly Conductive Polymer Filament Fabrication” and “Progress Toward an Ideal IR Obscurant with a Self-Heating Synthesis of Short, Thin Cu Nanowires”. She was also the co-first author in one publication entitled “One-Step Electrodeposition of Cu on Conductive 3D Printed Objects” and one manuscript in preparation: “Halide Ions Determine the Anisotropic Growth of Cu Nanowires and Nanoplates”. Finally, she was a co-author in four additional publications: “Stretchable Conductive Composites from Cu-Ag Nanowire Felt”, “Three-Dimensional Printing of a Complete Lithium Ion Battery with Fused Filament Fabrication”, “Accelerating Electrochemistry with Metal Nanowires”, and “Metal Nanowire Felt as a Flow-Through Electrode for High-Productivity Electrochemistry”. Mutya was also a two-time recipient

of the Nanoscience Certification Program Fellowship and the William Krigbaum Fellowship.